Orthogonal and Symmetric Haar Wavelets on the Sphere

by

Christian Lessig

A thesis submitted in conformity with the requirements
for the degree of Master of Science
Graduate Department of Computer Science
University of Toronto

Abstract

Orthogonal and Symmetric Haar Wavelets on the Sphere

Christian Lessig

Master of Science

Graduate Department of Computer Science

University of Toronto

2007

The efficient representation of signals defined over spherical domains has many applications. We derive a new spherical Haar wavelet basis (SOHO) that is both orthogonal and symmetric, rebutting previous work that presumed the nonexistence of such a basis. The key to obtaining the basis is a novel spherical subdivision scheme that defines a partition acting as the domain of the basis functions. We also derive basis transformation matrices that permit the rotation of a signal represented in our new basis. The elements of these matrices can be computed analytically, in contrast to previous work that required numerical computations. Experimental results for the approximation and rotation of spherical signals verify that the superior theoretical properties of the SOHO wavelet basis also have practical benefits over previous representations.

Acknowledgements

I want to thank ...

Eugene Fiume for asking the right questions and having faith.

Mike Daum for listening.

My parents for always supporting me.

And everyone else who helped to make this work possible.

Contents

Nomenclature

$\#X$	Cardinality of a set X
$\alpha_{j,k}$	Area of a spherical triangle $T_{j,k}$
$\|\cdot\|$	Norm of a Banach space
β_{i_1,i_2}	Coupling coefficient, element of a basis transformation matrix
$\triangle, \triangledown$	Nodes of a forest
$\breve{\psi}_{j,m}$	Dual basis function of a wavelet basis
χ	Characteristic function
$\delta_{k,k'}$	Kronecker delta
ℓ_p	Norm associated with the space L_p
$\eta_{j,k}$	Normalization constant of a scaling basis function defined over $T_{j,k}$
$\gamma_{j,m}$	Basis function coefficient of a wavelet basis function $\psi_{j,m}$
$\hat{\psi}_{j,m}$	Primary basis function of a wavelet basis
$\lambda_{j,k}$	Basis function coefficient of a scaling basis function $\varphi_{j,k}$
$\mathbb{R}$	Real numbers

$\mathbb{Z}$ Integer numbers

$\mathbb{Z}^+$ Positive integer numbers (including zero)

$\mathcal{B}$ Set of leaf nodes of a forest

$\mathcal{F}$ Nodes of a forest

$\mathcal{F}_j$ Nodes of a forest at generation j

$\mathcal{M}$ Multiresolution analysis

$\mathcal{P}$ Partition over which the SOHO wavelet basis is defined

$\mathcal{T}$ Tree

$\mathfrak{F}$ Field over which a Banach space is defined

$\text{supp}(f)$ Support of a function f

$\omega = (\theta, \phi)$ Spherical coordinates of a point on the unit sphere

Ψ Wavelet basis

$\psi_{j,m}$ Primary wavelet basis function

$\tau_{j,k}$ Characteristic function of a spherical triangle $T_{j,k}$

$\tilde{\psi}_{j,m}$ Dual wavelet basis function of $\psi_{j,m}$

$\tilde{\varphi}_{j,k}$ Dual scaling basis function of $\varphi_{j,k}$

$\tilde{X}$ Dual space of a Banach space X

$\varphi_{j,k}$ Primary scaling basis function

$\varrho^i_{j,k}$ Normalization constant for the i^{th} wavelet basis function defined over $T_{j,k}$

$d(\mathcal{F})$ Depth of a forest

E Spherical excess

$g_{j,m,l}$ Wavelet basis function filter coefficients associated with $\psi_{j,m}$

$h_{j,k,l}$ Scaling basis function filter coefficient associated with $\varphi_{j,k}$

I Identity matrix

L_p Space of p-power integrable functions

M^T Transpose of a matrix M

M^{-1} Inverse of a matrix M

$T_{j,k}$ Spherical triangle forming a domain of a partition of the sphere

V_j Subspace of a multiresolution analysis at level j

Chapter 1

Introduction

Many signals are naturally parametrized over the unit sphere $\mathbb{S}^2$. Examples can be found in astronomy, computer graphics, medical imaging, and many other fields. An efficient and distortion free representation of spherical signals is therefore of importance. Of particular interest are the ability to approximate a wide range of signals accurately with minimal storage costs, and the possibility of obtaining computationally efficient algorithms to process a signal.

In the following, we will introduce the ideas which yield such an efficient representation of spherical signals. We will also provide some intuitions of why these techniques work and why some representations are better suited for our purposes than others. The reader is referred to the following chapters for a more mathematical treatment of the subjects. We will also delay any proofs of our claims to later chapters.

1.1 How to represent signals?

A signal, or, to use terminology from mathematics, a function, can be represented in a variety of ways. For our purposes, we represent functions using bases that have shown

to be efficient for the representation of a wide range of signals in many different fields. Formed by a sequence of functions, a basis can represent *any* function from the space spanned by the basis functions. The basis representation will be seen to be optimal in that it employs the minimal number of functions which is necessary to span the space. The basis representation of a signal is formed by a unique sequence of basis function coefficients. These are obtained by projecting the signal into the basis. How the projection is accomplished in detail depends on the particular representation. In most cases it requires the computation of inner products of dual basis functions and the signal:

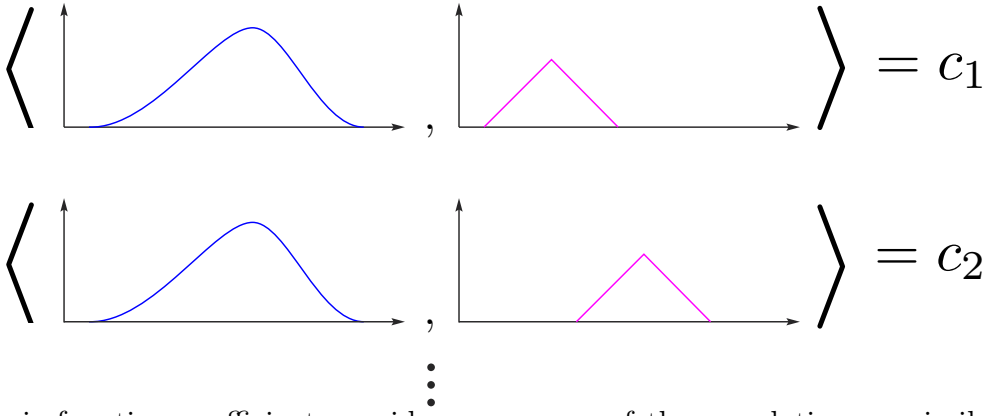

Every basis function coefficient provides a measure of the correlation, or similarity, of the associated basis function with the signal. Recombining the coefficients and the basis functions therefore yields a function which locally resembles the signal:

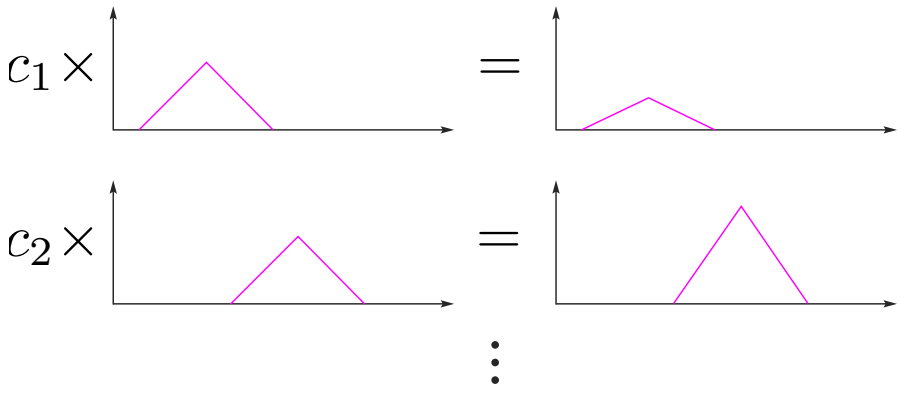

The original signal can be recovered, or reconstructed, by combining all scaled basis functions. Many bases have an infinite number of basis functions and combining all of them is therefore infeasible. In practice, a finite number of basis functions is used yielding an approximation of the original signal:

$$S \approx \sum_i c_i f_i \quad \Rightarrow$$ 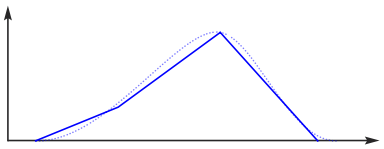

We already hinted that there is not only one basis for a given space. In fact, every space has an infinite number of bases. These differ in their properties and therefore in their practicality for different applications, making some bases better suited for our purposes than others. This however leaves the question: What bases are efficient for the approximation and processing of all-frequency signals on the sphere?

1.2 But what are wavelets?

Wavelets are very versatile and flexible representations for signals. Discrete wavelets, for example, are well suited for compact representation and for approximation. Continuous wavelets, in contrast, are more suitable for analysis. Wavelet representations are not limited to be (minimal) bases. In particular continuous wavelets are often overcomplete, that is the sequence of "basis" functions provides a redundant representation of a signal. For our applications discrete wavelets that are bases are the representations of choice. In the following, we will therefore concentrate on these, and for the sake of simplicity just denote them as wavelets.

Nonetheless, the question what wavelets are has yet to be answered. Interestingly, even after 25 years of intensive research in the field — or probably just because of this — there is still no unique definition of wavelets. Wim Sweldens, one of the pioneers of wavelet theory, characterized them as [89]:

"Building blocks which can quickly decorrelate data." .

In the following, we will use this "definition" to give some insights about the characteristics of wavelets, and to explain why these bases provide very compact representations for all-frequency signals. We here consider a representation as compact if most of the basis

function coefficients are very small or zero; approximations can then be obtained easily with small error by ignoring the contributions of the smallest basis function coefficients during reconstruction.

"Building Blocks" The basis functions of a wavelet basis all have a very similar structure. In fact, for first generation wavelets all basis functions of a basis are scales and translates of one mother basis function. This similarity leads to the notion of "blocks". "Building" attributes to the aggregation of wavelets to represent all functions in a space.

"Quickly" The word "quickly" refers to the existence of fast, linear-time transform algorithms for both the projection of a signal into a wavelet basis and for the reconstruction of a (possibly approximate) signal from its basis representation.
Computing inner products between dual basis functions and a signal does not lead to such fast algorithms. Therefore, filter coefficients, which are naturally associated with the basis functions, and the hierarchical structure of wavelet bases are used to efficiently compute the transforms. In practice, the filter coefficients are in fact the most useful representation of the basis functions and can also be employed to establish different properties of a basis.

"Decorrelate Data" The signals we want to represent in applications are not random noise — they have structure and similarities in the data. These correlations can be observed in different regions and at different scales. Natural signals are therefore localized in both space and frequency. As discussed earlier, a basis function together with the corresponding basis function coefficient locally resembles a signal. For an efficient representation a basis should therefore exhibit the same structure as the signals they represent. Wavelet bases are designed so that the basis functions are localized in both space

and frequency. Localization is however not sufficient for the compact representation of natural signals. It only employs the spatial dimension of correlations and guarantees therefore that the bases and the signals have the same structure; it does not, however, automatically lead to small basis function coefficients. To obtain compact representations, the similarity in the data has to be exploited. The wavelet basis functions are designed to assess differences in a signal and the basis function coefficients are therefore measures for local dissimilarity: for regions which "look" very similar the basis function coefficients are very small or zero, whereas inhomogeneous regions provide larger basis function coefficients. Representing a natural signal (that has correlations) in a wavelet basis therefore yields a representation in which most of the basis function coefficients are very small or zero. To paraphrase these observations, the compactness of wavelet representations stems from both the localization of the bases in space and frequency and the design of the wavelet basis functions to assess differences.
As a side note, the idea of representing differences rather than homogeneities has interesting connections to information theory, in particular to the definition of information as measure of the predictability in a message (cf. [78]).

With the explanations detailed in this section it becomes clear that wavelets are efficient for the compact representation and approximation of all-frequency signals.

1.3 What about spherical signals?

The simplest approach to representing signals on $\mathbb{S}^2$ is to map the spherical domain onto a plane. Then, for example wavelets in two dimensions can be employed to efficiently represent spherical signals. However, the mapping unavoidably leads to nonuniform distortion between the planar parametrization and the sphere, and thus such representations are only of limited value. In the past, different alternative representations parametrized over the sphere have been proposed. These are free of distortion but each of the techniques

suffers from severe limitations for the applications at which we are aiming at.

These limitations led to the development of spherical wavelets. In addition to the advantages of wavelets which have been discussed previously, the bases are parametrized over the sphere and therefore free of distortion. We believe however that all spherical wavelet bases proposed in the literature are limited in their ability to efficiently approximate and process all-frequency signals on the sphere. As will be discussed in the following, three properties are essential for such an efficient representation.

Orthonormality Orthonormal bases provide a variety of theoretical and practical advantages: most notably the optimal approximation in a specific but highly relevant error measure, the so called ℓ_2 norm, can be computed efficiently. For fixed storage costs, the optimal approximation is given by the k-largest basis function coefficients. The representation of the salient features of a signal in a few basis function coefficients makes wavelets thereby better suited for approximation than other orthogonal bases. Furthermore, obtaining the dual basis functions, which are necessary to obtain the basis representation of a signal, and establishing properties of a representation is in many cases only for orthonormal bases efficiently possible.

Haar-like Nature The basis functions of Haar-like wavelets have minimal support for face-based wavelets. The costs for performing wavelet transforms are therefore minimal, and, more importantly, processing a signal in its basis representation is for Haar-like bases significantly more efficient than for wavelets with basis functions having wider support. In the literature, it has often been assumed that Haar-like bases are only efficient for the representation of piecewise constant signals. Both theoretical and practical results show however that Haar-like wavelet bases are efficient for the representation of functions of bounded variation: natural, all-frequency signals as found in many applications.

Symmetry Symmetry guarantees an orientation-free representation of features in a basis. This avoids distortion when a signal is approximated. The high sensitivity of the human visual system to non-symmetric artifacts makes this particularly important for the visual quality of reconstructed signals.

The discussion above makes clear that an orthonormal and symmetric spherical Haar wavelet basis is particularly suited for an efficient approximation and processing of all-frequency signals on the sphere.

1.4 SOHO wavelets?

The analysis provided in the last sections led us to the development of the *SOHO* wavelet basis. To our knowledge this is the first spherical Haar wavelet basis that is both orthonormal and symmetric. A novel subdivision scheme of the sphere, which provides the partition acting as the domain of the wavelet basis functions, enabled us to obtain the basis. The derivation thereby refutes previous work in which it was claimed that an orthonormal and symmetric spherical Haar wavelet basis does not exist.
The practical relevance of the superior theoretical properties of the SOHO wavelet basis has been verified with experiments. These show that the SOHO wavelet basis provides competitive or lower error rates for the approximation of signals than previously proposed spherical Haar wavelet bases. The visual quality of reconstructed signals confirms these results.

1.5 But we have to rotate our signals?

An important operation for many applications is the rotation of a signal in its basis representation. For example in computer graphics, rotation is necessary to efficiently solve

the rendering equation, and in medical imaging it is used to align spherical data sets for analysis. The objective of the rotation is thereby not primarily to obtain a rotated signal, but to provide a representation of such a signal which permits efficient processing. A change of basis yields such a representation, making it necessary to employ basis transformation matrices for the rotation. In previous work, numerical computation of the coupling coefficients forming these matrices was necessary. We show that for spherical Haar wavelet bases it is possible to analytically compute the matrix elements. The rotation of signals in a representations that is parametrized over the sphere additionally avoids magnification of distortion artifacts that can be observed for planar parametrized representations. An analysis of the structure of the rotation matrices shows that these are quasi block symmetric and very sparse. This follows from the definition of the partitions and the local support of the wavelet basis functions, and is important for efficient computation and minimizing storage costs. Experimental results show that rotation in the SOHO wavelet basis provides competitive or lower error rates than a rotation in other representations for spherical signals. The computations are efficient due to the sparsity of the rotation matrices. We also show that an approximation of the matrices reduces the computational costs and storage requirements by orders of magnitude with only moderately increased error rates in the rotated signals.

1.6 What's next?

After a discussion of related work in Chapter 2, we will present in Chapter 3 the mathematical concepts which underly our work. There, we will also provide the notation for the remainder of the thesis. A constructive proof for the SOHO wavelet basis will be presented in the first part of Chapter 4. In the second part of the chapter, we will establish that the SOHO wavelets are an unconditional basis of the space $L_2(\mathbb{S}^2, d\omega)$. The mathematically less inclined reader can safely omit this section on a first reading. The

derivation of the rotation matrices and the analysis of their properties will be provided in Chapter 5. Chapter 6 is devoted to a presentation of experimental results and an interpretation of the observations. A discussion of avenues for future work is provided in Chapter 7. We conclude the thesis with some summarizing remarks in Chapter 8.

Chapter 2

Related Work

2.1 Representation of Spherical Signals

In the past, different techniques such as bases, frames, and hierarchical subdivision schemes have been used to represent, approximate, analyse, or process signals defined on the sphere $\mathbb{S}^2$. In the following, we will discuss the different representations in more detail and reveal why none of them is well suited for the efficient approximation and processing of all-frequency signals on the sphere.

Spherical Harmonics [48] are the analogue to the Fourier basis on the sphere. The basis functions are defined over Legendre polynomials and therefore arranged into frequency bands yielding a localization of the SH basis in frequency. A localization in space is prevented by the global support of the SH basis functions. Spherical Harmonics are therefore suitable only for the representations of low-frequency signals. High-frequency data cannot be represented efficiently. In fact, the harmonic nature of the basis often yields ringing artifacts for these signals (cf. Figure 2 in [56]). We refer to the book by Edmonds [23] and the excellent tutorial by Green [35] for a more detailed discussion of the properties of the SH basis.

Since their development in the 1940s, Spherical Harmonics have been used widely in particular in physics and chemistry, leading to a variety of algorithms to perform operations in the SH basis. The availability of these techniques helped to establish Spherical Harmonics in many other fields such as geoscience and medical imaging [16, 41]. Since the mid 1980s, the SH basis has also been used widely in computer graphics, for example for the representation of bidirectional reflectance distribution functions (BRDFs) [97], for representing radiance in off-line radiosity computations [80], and for the efficient computation of light transport effects in environment map rendering and precomputed radiance transfer (PRT) [12, 69, 42, 82].

In the past decade, Spherical Harmonics have been complemented by a variety of alternative, spherical and hemispherical harmonic bases. Makhotkin [49] and Koenderink et al. [43] developed bases for the hemisphere based on Jacobi and Zernicke polynomials, respectively. Compared to the SH basis, the costs for evaluating the basis functions are however significantly higher, limiting the practicality of the bases [30]. Alfeld et al. [3] proposed *spherical Bernstein-Bézier polynomials* for the representation of spherical signals. As with analogous Bézier curves in Euclidean spaces, the basis has been used mainly for the approximation of signals, for example for fitting scattered data on the sphere and for interpolation [4]. Obtaining an approximation of a signal in spherical Bernstein-Bézier polynomials requires to solve a sparse linear system that is often ill-conditioned [4]. This makes the basis projection expensive, and spherical Bernstein-Bézier polynomials are therefore ill-suited for many applications. Based on associated Legendre polynomials, Gautron et al. [30] developed *Hemispherical Harmonics* (HSH). The basis is similar to Spherical Harmonics but better suited for the representation of hemispherical signals. Compared to the harmonic bases proposed by Makhotkin [49] and Koenderink et al. [43], Hemispherical Harmonics provide approximately the same error rates for representing hemispherical signals [30]. The costs for evaluating the basis functions are however significantly lower for the HSH basis [30]. Sloan et. al [83] proposed

Zonal Harmonics which are a restricted subset of the SH basis functions. In contrast to Spherical Harmonics, this basis permits efficient rotation of signals in the basis representation.

In addition to specific limitations discussed above, all harmonic bases suffer from global support of the basis functions and lacking efficiency for representing high-frequency data. The bases are therefore not practical for the efficient representation and processing of all-frequency signals.

Similar to harmonic bases, *spherical splines* are likewise defined over polynomial functions. Many of the properties of splines in Euclidean spaces also hold for the spherical domain [32, 11]. The basis is therefore suitable for approximating and processing low-frequency signals, and has been used for example in medical imaging [38, 11, 6]. The smooth nature of the basis functions limits however the practicality of spherical splines for the representation of high-frequency data.

In Euclidean spaces, *principal components analysis* (PCA) [39] and *singular value decomposition* (SVD) are two of the most popular algorithms for approximating high-dimensional data [81, 52]. The techniques are limited in that they are not able to respect the inherent structure of a manifold such as the embedding $\mathbb{S}^2 \subset \mathbb{R}^3$ in the high-dimensional space [73]. To overcome this limitation, Roweis and Saul [73] developed *locally linear embedding* (LLE) [73] as an alternative to obtaining low-dimensional approximations of high-dimensional data lying on a manifold. This technique is however designed for general spaces and does not exploit the known structure of $\mathbb{S}^2$. Additionally, obtaining the representation of a signal with LLE is expensive.

Spherical radial basis functions (SRBFs), sometimes also denoted as multivariate approximations, have been used widely in particular for the approximation and interpolation of spherical data [25]. An SRBF basis is unstructured and formed by kernels which are the equivalents to the well-known radial basis functions on the sphere. The repre-

sentation of a signal is obtained by fitting the position (space) and the size (scale) of the kernel functions to the data. Similar to wavelets, the bases are therefore localized in both space and frequency. The practicality of SRBF bases is limited by the prohibitive costs for obtaining the basis representation of a signal [34, 93]. Additionally, the data-dependent arrangement and the non-hierarchical structure of the basis functions makes it difficult to develop efficient algorithms to perform computations in the basis representation. In particular for wavelet bases such optimizations have shown to be powerful [57, 88]. Applications for SRBF bases can be found for example in astronomy and geoscience [25, 55, 27, 26]. Recently, spherical radial basis functions have also been employed in computer graphics [34, 93].

Continuous spherical wavelets (CSW) have been developed for example in physics and geoscience. In analogy with the Fourier transform which is used in one dimension to derive wavelet bases, Freeden and Windheuser [28], Freeden [26], and Yeo et al. [100] used Spherical Harmonics to develop CSW bases. In physics, group theoretic approaches have been employed to derive continuous wavelets on $\mathbb{S}^2$ [5]. Given the structural similarity between SRBF kernels and the Mexican hat or the Morlet wavelet, it is not surprising that it is possible to construct spherical wavelets based on SRBF kernels [55, 28, 27, 26]. Continuous wavelets are in most cases overcomplete in the sense that these provide redundant representations of a signal. This makes them well suited for signal analysis but inefficient for the compact representation or approximation of signals [5, 99, 100]. Continuous spherical wavelets are therefore not the representation of choice for our applications. We refer to the books by Freeden [26] and Antoine et al. [5], and the references in there, for a more detailed discussion of continuous wavelets on the sphere.

In contrast to continuous wavelets, discrete wavelet bases are suitable for approximating and processing signals, and in the past a variety of representations for spherical signals has been proposed. Lounsbery et al. [46] developed wavelet bases over subdivision surfaces that can represent sphere-like shapes. Their construction can employ a wide range of

subdivision schemes but none of the resulting bases is orthogonal. The global support of the basis functions made it additionally necessary to truncate the wavelets. Such an approximation does however no longer yield true wavelet bases. For the definition of the inner product, Lounsbery et al. also assumed that all partitions at a given level have the same area. This is in general not true.

The first discrete wavelet basis specifically designed for the sphere was proposed by Dahlke et al. [18]. The basis is C^1 and also formed by basis functions of global support.

Girardi and Sweldens [31] developed orthogonal Haar wavelets for general measure spaces. Their scaling functions are identical to those employed in our work. The construction does however not yield a symmetric basis on the sphere.

In their seminal work, Schröder and Sweldens [76] proposed different vertex- and face-based spherical wavelets. Based on the results by Girardi and Sweldens [31], the authors developed the Bio-Haar wavelets, a semi-orthogonal and symmetric spherical Haar wavelet basis. The Lifting scheme has been employed by the authors to obtain smooth, spherical wavelets that are either biorthogonal or semi-orthogonal. The partitions over which the bases are defined are derived from a subdivision of the sphere. The domains at the coarsest level are obtained by projecting a platonic solid with triangular faces such as the octahedron or the icosahedron onto the sphere. The geodesic bisectors of the great arcs forming the edges of the domains give for all levels the new vertices at the next finer level. This results in a 4-fold subdivision. In the remainder of the thesis, we shall refer to this technique as *geodesic bisector subdivision*. To assess the performance of the new bases, Schröder and Sweldens performed experiments with common spherical signals from computer graphics. The results for the approximation of the signals show that spherical wavelet bases are well suited for the representation of functions which are parametrized over the sphere. An interesting side result of the work by Schröder and Sweldens is that Haar-like wavelets are as efficient as smoother bases for the representation of image-like

signals on the sphere. This resembles earlier theoretical results by Donoho [22] which showed that Haar-like bases are close to optimal for the representation of functions of bounded variations. Similar results have also been obtained by Ng et al. [56]. These show that Haar-like bases are efficient for the representation of all-frequency signals, and that they clearly outperform Spherical Harmonics for typical signals in applications.

Nielson et al. [58], and later Bonneau [7], developed semi-orthogonal, symmetric spherical Haar wavelet bases which are nearly orthogonal in that they become orthogonal in the limit case when the subdivision level goes to infinity. These bases are similar to the Bio-Haar wavelets proposed by Schröder and Sweldens [76], and in fact differ only in the definition of the filter coefficients. Roşca [71, 72] likewise developed a family of nearly orthogonal wavelets. Although the definition of the inner product employed in their work limits the bases to be nearly orthogonal, a norm equivalence with the standard norm on $\mathbb{S}^2$ permitted Roşca to establish that the wavelets are unconditional bases for the space $L_2(\mathbb{S}^2, d\omega)$ of functions with finite energy on the sphere. Nielson et al. [58] and Bonneau [7] did not show this for the bases developed in their works.

Ma et al. [47] proposed a Haar-like pseudo wavelet basis defined over the sphere. The basis is identical to that proposed by Bonneau [7], but it is assumed that the subdivision of a (spherical) partition yields child domains of equal area. This is is only true in the limit case and the representation is therefore not a basis of the space $L_2(\mathbb{S}^2, d\omega)$ (cf. Appendix A). With slight abuse of terminology, in the remainder of the thesis we shall refer to this representation as *pseudo Haar wavelets*. In contrast to the Bio-Haar wavelets or nearly orthogonal spherical Haar wavelet bases, the pseudo Haar wavelets provide the advantage that the filter coefficients are constant; in fact, they are identical to those of the non-standard Haar wavelet basis in $2D$ [87]. An area-isometry assumption similar to those by Ma et al. [47] had already been employed earlier by Pastor and Rodrigues [64] for the Bio-Haar wavelets proposed by Schröder and Sweldens [90]. Unfortunately, neither Pastor and Rodrigues nor Ma et al. analysed the error introduced by their assumptions.

Spherical Haar wavelet bases have been employed in different applications. Wang et al. [96] used the Bio-Haar wavelets for image based relighting (IBL). By exploiting the structure of their high-dimensional data sets the authors were able to further compress the representation in spherical wavelets with a standard $2D$ wavelet decomposition yielding even better overall compression rates. Recently, Nain et al. used the Bio-Haar wavelets for $3D$-shape analysis and segmentation [53, 54]. Ma et al. [47] employed the pseudo Haar basis for PRT, enhancing the triple product integral algorithm by Ng et al. [57].

In the literature, next to spherical wavelet bases also wavelets defined over planar domains have been used to represent signals on $\mathbb{S}^2$. In contrast to wavelets parametrized over the sphere, the techniques are limited in that mapping the sphere onto a planar domain unavoidably leads to distortion. The most common planar wavelet representation for spherical signals has been proposed by Ng et al. [56] and uses $2D$ non-standard Haar wavelets parametrized over the faces of a cubemap. In independent work, Roşca developed a very similar representation. She also provides a more formal description of the technique [70]. In the remainder of the thesis, we shall refer to this representation as *Haar cubemap basis*. An alternative technique which uses a planar parametrization of the sphere has been developed by Wang et al. [95]. There, the octahedral map [67] is employed as parametrization of the sphere and the planarized signals are represented in non-standard Haar wavelets in $2D$ [87]. Compared to the Haar cubemap basis this representation suffers from a more severe distortion of the spherical domain (cf. Figure 2 in [95] and Figure 2 in [56]).

In computer graphics, the Haar cubemap basis has been used for example for PRT [57] and PRT for dynamic scenes [101, 88]. Okabe et al. [60] employed the representation for inverse rendering in computer vision. Similar to the work by Ng et al. [56], these authors also demonstrated that Haar-like wavelet bases are better suited for the representation of all-frequency signals than Spherical Harmonics. Lalonde and Fournier [45] used tensor product wavelets for the representation of BRDFs. Although the authors argued that

Haar-like wavelet bases are less efficient for the representation of low-frequency signals than smoother wavelets, their results show that the differences are not significant in practice.

The efficiency of Haar-like wavelet bases for processing signals has been demonstrated in particular in computer graphics. Ng et al. [57] for example demonstrated that Haar-like wavelet bases are significantly more efficient for the computation of triple product integrals than other orthonormal representations such as Spherical Harmonics. Sun and Mukherjee [88] later generalized this work. The use of a Haar-like basis enabled these authors to efficiently compute n-factor product integrals.

The geodesic bisector subdivision is only one possibility to define a partition on the sphere. In particular in geoscience and astronomy a variety of alternative constructions have been developed; in the literature these are often denoted as *Geodesic Discrete Global Grid Systems* (GDGGS) [74].

Many partition schemes are similar to the geodesic bisector subdivision. Following Sahr et al. [74], these can be classified according to three criteria.

Base Polyhedron The most common choices for the base polyhedron are octahedron and icosahedron. The icosahedron minimizes area and shape distortion while the octahedron is better suited for hemispherical signals [76]. The alignment of the domains for the octahedron also coincides with other parametrizations of the sphere.

Subdivision Scheme The subdivision, which yields the hierarchical structure of a partition, can be performed either in the plane or on the surface of the sphere. Subdivision schemes can be further classified by the number of child partitions that result from a subdivision step and by the shape of the domains. For triangular domains, an n^2-fold subdivision is possible by choosing $n - 1$ new points on each edge of a parent

partition. In practice only 4-fold and 9-fold subdivisions are used. In addition to subdivision schemes based on (possibly spherical) triangles, techniques based on quadrilaterals or hexagons have been proposed. Most computations become however more involved for non-triangular domains. Hexagonal domains have the additional disadvantage that they cannot be subdivided into a set of smaller hexagons and approximations have to be employed to obtain a hierarchical, strictly nested structure.

Inverse Map Projection If the subdivision is performed in the plane then the resulting domains have to be projected onto the sphere to establish a partition of $\mathbb{S}^2$. The book by Snyder [85] provides an excellent overview over suitable projections and their properties. Relevant for the construction of a partition is thereby in particular the trade-off between area and shape distortion provided by the individual schemes. The results by White et al. [98] show that the geodesic bisector subdivision provides a good compromise between area and shape distortion.

One of the most interesting partitions proposed in astronomy is the HEALPix scheme [33, 94]. The construction provides the advantage that all domains of the sphere at a given level are of equal area, making the partition well suited for the development of orthonormal bases. The shape distortion for the HEALPix domains is however non-uniform and in particular for the pole regions rather large (cf. Figure 2 in [94]). The construction is therefore less suited for the development of symmetric wavelet bases.

2.2 Basis Transformation Matrices

For many applications such as environment map rendering in computer graphics, molecular electronic structure calculations in physics, and the alignment of spherical data sets in medical imaging, the rotation of spherical signals in their basis representation is necessary. The problem has been studied extensively only for Spherical Harmonics where both ana-

lytic and computational solutions for the rotation have been proposed [23, 13, 42, 44, 65]. For some time it was believed that no efficient algorithm for the rotation of a signal in a wavelet basis representation exists [95]. By employing the same mathematical concepts which permit rotations in the SH basis, Wang et al. [95] were recently able to show that basis transformation matrices can be used for the rotation.

For wavelets, the number of basis functions used in an application is typically higher than for the SH basis. The rotation matrices for wavelet bases are therefore significantly larger than for Spherical Harmonics. Wang et al. [95] showed however that the matrices for wavelets are very sparse. In combination with the sparse nature of the basis function coefficient vectors for typical signals, this enabled Wang et al. to demonstrate that a rotation of signals in a wavelet basis representation is practical in real-time applications [95].

2.3 Connection to the Presented Work

In this chapter different representations for spherical signals have been discussed. None of the existing techniques is however particularly well suited for an efficient approximation and processing of all-frequency signals on the sphere.

The global support of the basis functions makes harmonic bases such as Spherical Harmonics well suited only for the representation of low-frequency signals. Spherical radial basis functions are localized in both space and frequency and therefore efficient for the representation of all-frequency signals. The non-hierarchical structure of the basis functions makes it however very difficult to develop efficient algorithms to process a signal in an SRBF basis. Additionally, the basis projection is prohibitive expensive for spherical radial basis functions. Continuous spherical wavelets are designed for signal analysis and therefore not suited for our applications.

Haar-like wavelet bases have proven to be efficient for approximating and processing all-

frequency signals. For spherical signals, approaches which employ a planar parametrization of the sphere suffer however from distortion artifacts. Spherical Haar wavelets are free of distortion but the bases proposed in the literature are limited to either be symmetric *or* orthogonal, degrading the approximation performance of the representations. In this thesis, we develop the SOHO wavelet basis which is both orthogonal *and* symmetric. Our construction is similar to those by Schröder and Sweldens [76] and by Bonneau [7] but differs in that we modify the geodesic bisector subdivision employed in their works. This permits us to enforce both orthogonality and symmetry simultaneously.

Previous work employed wavelet bases defined over planar domains for the rotation of signals in a wavelet basis representation. This makes a numerical computation of the elements of the basis transformation matrices necessary. Additionally, rotation in a planar parametrized representations can give rise to magnification of parametrization artifacts. We show that for spherical Haar wavelet bases an analytic computation of the rotation matrices is possible. Experimental results verify that spherically parametrized wavelets are better suited for the rotations than representations defined over planar domains.

Chapter 3

Background

In this section we will establish the definitions and the notation for the remainder of the thesis. A basic understanding of algebra and analysis is assumed.

3.1 L_p Spaces and Bases

3.1.1 Banach Spaces, Norms, and L_p Spaces

Definition 1. A *Banach space* X is a vector space over the field $\mathfrak{F}$, of real or complex numbers, with a norm $\|\cdot\| \to [0, \infty[$ such that every Cauchy sequence (with respect to the metric $d(x, y) = \|x - y\|$) in X has a limit in X.

Definition 2. The *dual space* $\tilde{X}$ of a Banach space X is the Banach space of continuous linear maps $X \to \mathfrak{F}$.

In the following we will denote with a "tilde" all entities which are associated with a dual space.

Of particular interest for the discussion in this thesis are the Banach spaces L_p of p-power integrable functions. The norm ℓ_p associated with L_p is defined as

$$\|f\|_p = \left(\int |f|^p \, d\mu \right)^{1/p}, \tag{3.1}$$

where $f \in L_p$ and $\|f\|_p < \infty$, $\forall f \in X$. In the following, we will be mainly concerned with the space L_2 of functions with finite energy. Therefore, if not stated otherwise, $\|\cdot\|$ refers to the 2-norm.

The inner product on a Banach space X is a function $\langle \cdot, \cdot \rangle : X \times X \to \mathfrak{F}$. In this thesis we will only consider real valued inner product spaces so that $\mathfrak{F} = \mathbb{R}$. Every Banach space X with an inner product can be equipped with the norm

$$\|x\| = \langle x, x \rangle^{1/2} \quad , \quad x \in X.$$

3.1.2 Orthogonality and Biorthogonality

Let $\delta_{k,k'}$ be the Kronecker delta with

$$\delta_{k,k'} = \begin{cases} 1 & \text{if } k = k' \\ 0 & \text{otherwise.} \end{cases}$$

The elements of a sequence $\{f_k\}_{k=1}^m$ in a Banach space X are *orthogonal* if

$$\langle f_k, f_{k'} \rangle = \delta_{k,k'}.$$

Two sequences $\{f_k\}_{k=1}^m$ and $\left\{\tilde{f}_k\right\}_{k=1}^m$ in a Banach space X and its dual $\tilde{X}$, respectively, are *biorthogonal* if

$$\left\langle f_k, \tilde{f}_{k'} \right\rangle = \delta_{k,k'}.$$

3.1.3 Bases and Frames of Banach Spaces

Definition 3. Let X be a Banach space. A sequence of vectors $\{e_k\}_{k=1}^m$ belonging to X is a (Schauder) *basis* for X if, for each $f \in X$, there exist unique scalar coefficients $\{c_k(f)\}_{k=1}^m$ such that

$$f = \sum_{k=1}^{m} c_k(f)\, e_k. \tag{3.2}$$

The sequence $\{e_k\}_{k=1}^m$ is an ordered set, and it forms an *unconditional basis* if the sum in Eq. 3.2 converges unconditionally for all $f \in X$; therefore, if $\{e_k\}_{k=1}^m$ is *not* an unconditional basis then there exists a permutation σ of the basis function sequence for which $\left\{e_{\sigma(k)}\right\}_{k=1}^m$ is not a basis of X [14]. Besides the existence of an expansion for every $f \in X$, Definition 3 requires uniqueness of the basis function coefficient sequence $\{c_k(f)\}_{k=1}^m$. This is usually guaranteed by requiring that the basis functions e_k be linearly independent.

Definition 4. Let $\{e_k\}_{k=1}^m$ be a sequence in a Banach space X. The elements of $\{e_k\}_{k=1}^m$ are *linearly independent* if $\sum_{k=1}^m c_k e_k = 0$ implies that $c_k = 0$ for all $k = 1, 2, \ldots m$.

Different types of bases exist. In the past, orthonormal bases have often been considered as particularly desirable. These bases are also of high importance for this thesis.

Definition 5. A sequence $\{e_k\}_{k=1}^m$ belonging to a Banach space X is an *orthonormal basis* for X if $\{e_k\}_{k=1}^m$ is an unconditional basis and $\langle e_k, e_{k'} \rangle = \delta_{k,k'}$ for any k and k'.

A basis is *orthogonal* if $\langle e_k, e_{k'} \rangle = \rho_{k,k'}\, \delta_{k,k'}$, where $\rho_{k,k'} \in \mathbb{R}$ is some constant. Given an orthogonal basis, an orthonormal basis can be obtained easily by normalizing the basis functions so that their norm is one. Unless stated otherwise, in the remainder of the thesis the terms will therefore be used interchangeably.

Orthonormal bases provide a variety of desirable properties. For these bases it is however often difficult to enforce additional constraints on the basis functions. Riesz bases are more flexible:

Definition 6. A sequence of functions $\{f_k\}_{k=1}^m$ is a *Riesz basis* for a Banach space X if and only if it is an unconditional basis for X and

$$0 < \inf_k \|f_k\| \leq \sup_k \|f_k\| < \infty.$$

As a corollary to Definition 6, it is easy to see that every orthogonal basis is a Riesz basis. The basis function coefficients $\{c_k\}_{k=1}^m \in \mathfrak{F}$ of a Riesz basis can be obtained with a basis $\left\{\tilde{f}_k\right\}_{k=1}^m$ of the dual space $\tilde{X}$ of X. The $\left\{\tilde{f}_k\right\}_{k=1}^m$ form a continuous linear map from X into $\mathfrak{F}$. This is summarized in the following theorem:

Theorem 1. *Let $\{f_k\}_{k=1}^m$ be a Riesz basis for a Banach space X, then there exists a unique sequence $\left\{\tilde{f}_k\right\}_{k=1}^m$ such that*

$$f = \sum_{k=1}^m \langle f, \tilde{f}_k \rangle f_k = \sum_{k=1}^m c_k f_k \tag{3.3}$$

for every $f \in X$. The sequence $\left\{\tilde{f}_k\right\}_{k=1}^m$ is a Riesz basis of the dual space $\tilde{X}$ of X, and $\{f_k\}_{k=1}^m$ and $\left\{\tilde{f}_k\right\}_{k=1}^m$ are biorthogonal. The series in Eq. 3.3 is guaranteed to converge unconditionally.

A proof can be found in the book by Christensen [14]. The sequence $\left\{\tilde{f}_k\right\}_{k=1}^m$ is called the *dual basis* of the *primary basis* $\{f_k\}_{k=1}^m$, and the dual of $\left\{\tilde{f}_k\right\}_{k=1}^m$ is again $\{f_k\}_{k=1}^m$. The term *coordinate functionals* is sometimes also used to refer to the dual basis [90]. Note the practical importance of Theorem 1: It states how the sequence of basis function coefficients $\{c_k\}_{k=1}^m$ can be obtained given a basis and its dual.

Corollary 1. *The dual basis of an orthonormal basis $\{f_k\}_{k=1}^m$ is $\{f_k\}_{k=1}^m$.*

For an orthonormal basis it is therefore trivial to obtain the dual basis. This is not true for general Riesz bases.

Remark 1. Computing the basis function coefficients for a function f is commonly denoted as *projection* or *analysis*. The weighted sum of the basis function coefficients and the primary basis functions, which again yields f, is called *reconstruction* or *synthesis*.

A generalization of Riesz bases are frames as we now discuss:

Definition 7. A countable family of elements $\{f_k\}_{k=1}^m$ in a Banach space X is a *frame* for X if there exist strictly positive constants A and B such that

$$A\|f\|^2 \leq \sum_{k=1}^{m} |\langle f, f_k\rangle|^2 \leq B\|f\|^2, \quad \forall f \in X. \tag{3.4}$$

Note that $\{f_k\}_{k=1}^m$ is no longer required to be a basis of X. The lower condition in Eq. 3.4 implies that $\operatorname{span}\{f_k\}_{k=1}^m = X$, and it can be shown that for frames a similar expansion exists as for bases in Eq. 3.2. Frames are *overcomplete* and one can think of them as redundant bases. They can therefore provide alternative representations of signals.

3.2 Wavelets

The first wavelet basis was developed by Haar as early as 1910 [37]. After the Second World War the development mainly continued in the area of signal processing with the work on windowed Fourier transforms [29] and quadrature mirror filters [17]. A thorough and systematic understanding of the underlying concepts did however not begin until the 1980s. Contributions came then from a variety of fields such as signal processing, physics, computer graphics, and applied mathematics. This led to a substantial mathematical theory but gave also rise to applicable and fast algorithms.

Some of the first non-trivial wavelets were developed by Daubechies, Meyer, and Grossmann, to name a few of the many contributors. The applicability of these *first generation wavelets* was however limited by restrictive settings over which they were defined. In the 1990s, the work by Mallat, Sweldens and others generalized the concept of wavelets. The resulting *second generation wavelets* can be defined on general subspaces of $\mathbb{R}^n$, with weighted measures, and irregularly sampled data.

Despite the significant theory behind wavelets, there is no comprehensive definition of

them in a strictly mathematical sense. Three properties of a sequence $\{f_k\}_{k=1}^m$ in a space L_p, with fixed but arbitrary $0 < p < \infty$, are usually required to consider it as a wavelet:

(P1) The sequence $\{f_k\}_{k=1}^m$ forms a Riesz basis or a frame of L_p. This guarantees perfect reconstruction.

(P2) The elements of $\{f_k\}_{k=1}^m$ are localized in both space and frequency. The localization guarantees efficient decorrelation of signals which is important for compression. For typical signals a large proportion of the basis function coefficients is zero or close to zero, and a few coefficients are sufficient to represent the salient characteristics of a signal.

(P3) Fast algorithms for the analysis, synthesis, and processing of a signal in its basis representation exist.

For wavelets typically the space L_2 is considered and we will therefore restrict ourselves to this space for the remainder of the thesis.

The characterization of wavelets as stated above is a rather liberal one, following those in an article by Sweldens [91]. In this thesis we are only interested in wavelets that are bases. This corresponds to a more conservative characterisation found for example in another, more technical article by Sweldens [90]. In the following we will therefore only consider *wavelet bases* and the term "wavelet" will always refer to this restrictive characterization.

3.3 First Generation Wavelets

Next to properties (P1) to (P3) from the last section, first generation or classic wavelets are characterized by two additional properties:

- The basis functions are dyadic scales and translates of one *mother wavelet* ψ:

$$\psi_{j,k} = 2^j \psi + k, \tag{3.5}$$

  where j defines the scale or dilation of the basis functions and k determines the translation on level j.

- Fourier analysis can be used to develop the basis and establish its properties.

For first generation wavelets much research was devoted to obtaining bases with two properties: compact support and linear phase. Compact support is important because the costs for analysis and synthesis increase rapidly with the support size. Linear phase is desirable because it is an only mild form of phase distortion. This avoids the loss in frequency localization which follows from nonlinear phase shift and guarantees that efficient approximation and coding techniques exist. From a theoretical point of view, bases with zero phase distortion are even more desirable. For many practical settings however, for example when causality is required, bases with zero phase shift do not exist [61]. *Symmetry* of the basis functions is a sufficient condition for linear phase. In the literature, therefore often symmetry rather than linear phase is required for a wavelet basis. Note that the symmetry of the SOHO wavelet basis is not related to the symmetry of first generation wavelets. The interested reader is referred to the excellent book by Chui [15] for a more detailed treatment of first generation wavelets.

Although classic wavelets do not suffer from global support of the basis functions, many limitations of the Fourier basis still apply [90]:

(L1) First generation wavelets are defined in (infinite) Euclidean spaces $\mathbb{R}^n$. Practical applications require bases defined over finite spaces or arbitrary subspaces of $\mathbb{R}^n$.

(L2) Applications such as analysis on curves and surfaces, and weighted approximations require bases adapted to weighted measures. First generation wavelets are usually limited to spaces with translation invariant (Haar-Lebesgue) measures.

(L3) In practice it is often necessary to work with irregularly sampled data. First generation wavelets require a regular sampling of the data.

3.4 Second Generation Wavelets

Second generation wavelets overcome the limitations of first generation wavelets and permit the representation of functions in L_2, the space of functions with finite energy, in a very general setting $L_2 \equiv L_2(X, \Sigma, \mu)$, where $X \subseteq \mathbb{R}^n$ is a spatial domain, Σ denotes a σ-algebra defined over X, and μ is a (possibly weighted) measure on Σ. First generation wavelets are therefore a subset of second generation wavelets where $X = \mathbb{R}^n$ and where the Haar-Lebesgue measure is used for μ. The connection between first and second generation wavelets has also been studied by Daubechies and Sweldens [19].

3.4.1 Forest and Trees

We will employ forests and trees as hierarchical index sets.

Definition 8. A *forest* $(\mathcal{F}, g, p, C, <)$ consists of a countable set $\mathcal{F}$ of *nodes*, along with a set of root nodes $R \subseteq \mathcal{F}$, a generation function $g : \mathcal{F} \to \mathbb{Z}$, a parent function $p : \mathcal{F} \setminus R \to \{\mathcal{F}, \emptyset\}$, a children function $C : \mathcal{F} \to p(\mathcal{F})$, and a partial ordering $<$ of the elements of $\mathcal{F}$ [31]. For arbitrary nodes $\triangle, \triangledown \in \mathcal{F}$, a forest can be characterized by:

1. $C(\triangle) = \{\triangledown \in \mathcal{F} \mid p(\triangledown) = \triangle\}$.
2. $0 \leq \#C(\triangle) < \infty$.
3. If $\triangledown \in C(\triangle)$ then $g(\triangledown) = 1 + g(\triangle)$.
4. If $p(\triangle) = \emptyset$ then $\triangle \in R$, that is $\triangle$ is a root node.
5. The ordering $<$ linearly orders the children $C(\triangle)$ for all $\triangle \in \mathcal{F}$.

6. If $g(\triangle) < g(\triangledown)$ and $p^n(\triangle) = p^m(\triangledown)$ for some $n, m \geq 0$, then $\triangle < \triangledown$, with $n, m \in \mathbb{Z}^+$.

The power function p^n of the parent function p is defined as the identity for $n = 0$ and $p^n(\triangle) = p(p^{n-1}(\triangle))$ for $n > 0$, with $n \in \mathbb{Z}^+$. An analogous definition is used for the power function C^n of the children function C. We note that $p(\triangle)$ has cardinality zero or one, while $C(\triangle)$ is of bounded but potentially arbitrarily large cardinality.

The given partial ordering extends to a linear ordering of the whole forest when each $\mathcal{F}_j$ of $\mathcal{F}$ is ordered linearly, where

$$\mathcal{F}_j = \{\triangle \in \mathcal{F} \mid g(\triangle) = j\}.$$

With the linear ordering we can index the elements of $\mathcal{F}$ with two indices $j \in \mathcal{J}$ and $k \in \mathcal{K}(j)$, where $\mathcal{J}$ can be identified with the generation function, and $\mathcal{K}(j)$ is defined by the linear ordering of $\mathcal{F}_j$.

The depth $d(\mathcal{F})$ of a forest is defined as

$$d(\mathcal{F}) = \max_{\triangle \in \mathcal{F}} g(\triangle).$$

A *leaf* $\oslash \in \mathcal{F}$ of a forest is a node which has no children, that is $\#C(\oslash) = \emptyset$. We will denote with $\mathcal{B}$ the set of all leaves in $\mathcal{F}$. It is often convenient to think of leaves as repeating at later generations:

$$\mathcal{F}_j^* = \mathcal{F}_j \bigcup \left\{ \bigcup_{i<j} \mathcal{B} \cap \mathcal{F}_i \right\}.$$

A *tree* $\mathcal{T}$ is a subset $\mathcal{T} \subseteq \mathcal{F}$ so that for all $\triangle, \triangledown \in \mathcal{T}$ there are $n, m \in \mathbb{Z}^+$ so that $\bigcirc = p^n(\triangle) = p^m(\triangledown)$. The node $\bigcirc \in \mathcal{T}$ is the root node of the tree and $\#R = 1$.

3.4.2 Multiresolution Analysis

The basis functions of first generation wavelets are scales and translates of one mother wavelet function. For arbitrary spaces $X \subseteq \mathbb{R}^n$ it is not possible to define the notion of

scaling and translation. In the second generation setting a *multiresolution analysis* $\mathcal{M}$ is employed to define the basis functions.

Definition 9. A *multiresolution analysis* $\mathcal{M} = \{V_j \subset L_2 \mid j \in \mathcal{J} \subset \mathbb{Z}\}$ is a sequence of nested subspaces V_j on different scales $j \in \mathcal{J}$ which satisfies:

1. $V_j \subset V_{j+1}$.
2. $\bigcup_{j\in\mathcal{J}} V_j$ is dense in L_2.
3. For every $j \in \mathcal{J}$, a Riesz basis of V_j is given by scaling functions $\{\varphi_{j,k} \mid k \in \mathcal{K}(j)\}$.

The $k \in \mathcal{K}(j)$ form a general index set defined over the scaling functions on level j. It follows from the fact that the V_j are Banach spaces and from Definition 2 that a dual multiresolution analysis $\tilde{M} = \left\{\tilde{V}_j \mid j \in \mathcal{J} \subset \mathbb{Z}\right\}$ formed by the dual spaces $\tilde{V}_j$ exists. A basis of the spaces $\tilde{V}_j$ is given by dual scaling functions $\tilde{\varphi}_{j,k}$. These are required to be biorthogonal to the primary scaling functions on the same level:

$$\langle \varphi_{j,k} \ , \ \tilde{\varphi}_{j,k'} \rangle = \delta_{k,k'} \quad k, k' \in \mathcal{K}(j). \tag{3.6}$$

With Theorem 1, a basis expansion of a function $f \in V_{j_0}$, for some fixed $j_0 \in \mathcal{J}$, is then given by

$$f = \sum_{k\in\mathcal{K}(j_0)} \langle f \ , \ \tilde{\varphi}_{j_0,k} \rangle \, \varphi_{j_0,k} = \sum_{k\in\mathcal{K}(j_0)} \lambda_{j_0,k} \ \varphi_{j_0,k},$$

where $\lambda_{j_0,k}$ are scaling function coefficients.

3.4.3 Partition

Definition 10. Let Σ be a σ-algebra of a space $X \subseteq \mathbb{R}^n$. A set of measurable subsets $\mathcal{S} = \{S_{j,k} \in \Sigma \mid j \in \mathcal{J}, \ k \in \mathcal{K}(j)\}$ is a *partition* of X iff:

1. $\forall j \in \mathcal{J}$: clos $\bigcup_{k\in\mathcal{K}(j)} S_{j,k} = X$ and the union is disjoint; that is for fixed j, the $S_{j,k}$ provide a simple cover of X.

2. $\mathcal{K}(j) \subset \mathcal{K}(j+1)$.

3. $S_{j+1,k} \subset S_{j,k}$.

4. For a fixed $k_0 \in \mathcal{K}(j_0)$, $\bigcap_{j>j_0} S_{j,k_0}$ is a set containing one point $x_{k_0} \in X$.

5. $S_{j,k} = \bigcup_{l \in C(S_{j,k})} S_{j+1,l}$.

A partition forms a forest where the nodes are the $S_{j,k}$.

3.4.4 Scaling Basis Functions

It follows from the nested structure of the spaces V_j that the scaling functions $\varphi_{j,k}$ satisfy a refinement relationship. Every $\varphi_{j,k}$ can be written as linear combination of scaling functions $\varphi_{j+1,l}$ at the next finer level:

$$\varphi_{j,k} = \sum_{l \in \mathcal{K}(j+1)} h_{j,k,l}\ \varphi_{j+1,l}. \tag{3.7}$$

The $h_{j,k,l}$ are scaling function filter coefficients. An analogous relationship with dual scaling function filter coefficients $\tilde{h}_{j,k,l}$ holds for the $\tilde{\varphi}_{j,k}$. In the following, it is assumed that all filters are of finite extent and uniformly bounded. This implies that finite index sets $\mathcal{L}(j,k)$ and $\mathcal{K}(j,l)$ exist with

$$\mathcal{L}(j,k) = \{l \in \mathcal{K}(j+1) \ \mid \ h_{j,k,l} \neq 0\}$$

$$\mathcal{K}(j,l) = \{k \in \mathcal{K}(j) \ \mid \ h_{j,k,l} \neq 0\}\,.$$

Analogous index sets $\tilde{\mathcal{L}}(j,k)$ and $\tilde{\mathcal{K}}(j,l)$ exist for the dual scaling functions. Unless stated otherwise, l is assumed to run over $\mathcal{L}(j,k)$ or $\tilde{\mathcal{L}}(j,k)$ and k over $\mathcal{K}(j,l)$ or $\tilde{\mathcal{K}}(j,l)$.

A necessary condition for the existence of a wavelet basis is the convergence of the *cascade algorithm* to the primary and dual scaling functions. The algorithm for the primary scaling basis functions is outlined below in Remark 2.

Remark 2. Let $\{\lambda_{j_0,k} = \delta_{k,k_0} \mid k \in \mathcal{K}(j_0)\}$ be a Kronecker sequence for fixed but arbitrary $j_0 \in \mathcal{J}$ and $k_0 \in \mathcal{K}(j_0)$. The sequences $\{\lambda_{j,k} \mid k \in \mathcal{K}(j)\}$, for $j > j_0$, is generated by recursively applying

$$\lambda_{j+1,l} = \sum_k h_{j,k,l}\ \lambda_{j,k}.$$

The function $f^{(j)}_{j_0,k_0}$ is defined as

$$f^{(j)}_{j_0,k_0} = \sum_{k \in \mathcal{K}(j)} \lambda_{j,k}\ \chi_{S_{j,k}} \qquad \text{for} \quad j \geq j_0, \tag{3.8}$$

where $\chi_{S_{j,k}}$ is the characteristic function of $S_{j,k}$. If $\lim_{j\to\infty} f^{(j)}_{j_0,k_0}$ converges to a function in L_2 then it is defined to be the scaling function φ_{j_0,k_0}. For $j > j_0$, the function $f^{(j)}_{j_0,k_0}$ satisfies [90]:

$$f^{(j)}_{j_0,k_0} = \sum_l h_{j_0,k_0,l}\ f^{(j)}_{j_0+1,l}. \tag{3.9}$$

The cascade algorithm for the dual scaling functions is defined analogously.

If the cascade algorithm converges for all $j_0 \in \mathcal{J}$ and $k_0 \in \mathcal{K}(j_0)$ then the partition $\mathcal{S}$ and the filter coefficients $h_{j,k,l}$ and $\tilde{h}_{j,k,l}$ define sets of primary and dual scaling functions that satisfy the refinement relationship in Eq. 3.7. This can be seen by letting $j \to \infty$ in Eq. 3.9.

3.4.5 Wavelet Basis Functions

The wavelet basis functions $\{\psi_{j,m} \mid j \in \mathcal{J},\ m \in \mathcal{M}(j)\}$ span the difference spaces W_j, with $V_j \oplus W_j = V_{j+1}$. The $m \in \mathcal{M}(j)$ form a general index set defined over the wavelet basis functions at level j. It follows from the definition of the $\psi_{j,m}$ over the subspace $W_j \subset V_{j+1}$ that wavelet basis function filter coefficients $g_{j,m,l}$ exist with

$$\psi_{j,m} = \sum_{l \in \mathcal{K}(j+1)} g_{j,m,l}\ \varphi_{j+1,l}. \tag{3.10}$$

Analogous to the primary wavelet basis functions $\psi_{j,m}$, dual wavelet basis functions $\tilde{\psi}_{j,m}$ exist. These span the difference spaces $\tilde{W}_j$, with $\tilde{V}_j \oplus \tilde{W}_j = \tilde{V}_{j+1}$. Dual wavelet basis

function filter coefficients $\tilde{g}_{j,m,l}$ define the $\tilde{\psi}_{j,m}$ as linear combinations of dual scaling functions $\tilde{\varphi}_{j+1,l}$. As with $\mathcal{K}(j,l)$ and $\tilde{\mathcal{K}}(j,l)$, the index sets $\mathcal{M}(j,l)$ and $\tilde{\mathcal{M}}(j,l)$ are likewise defined, and $\mathcal{L}(j,m)$ and $\tilde{\mathcal{L}}(j,m)$ are index sets which run over the nonzero wavelet basis function filter coefficients. Unless stated otherwise, in the following l is assumed to run over $\mathcal{L}(j,m)$ or $\tilde{\mathcal{L}}(j,m)$ and m to run over $\mathcal{M}(j,l)$ or $\tilde{\mathcal{M}}(j,l)$.

The primary and dual wavelet basis functions are biorthogonal:

$$\left\langle \psi_{j,m}\,,\,\tilde{\psi}_{j',m'} \right\rangle = \delta_{j,j'}\,\delta_{m,m'} \quad \text{for} \quad k \in \mathcal{K}(j),\ k' \in \mathcal{K}(j'). \tag{3.11}$$

3.4.6 Filter Coefficients

The biorthogonality of the basis functions can be related back to the filter coefficients:

$$\begin{aligned} \textstyle\sum_l\ g_{j,m,l}\ \tilde{g}_{j,m',l} = \delta_{m,m'} \qquad \textstyle\sum_l\ h_{j,k,l}\ \tilde{g}_{j,m,l} = 0 \\ \textstyle\sum_l\ h_{j,k,l}\ \tilde{h}_{j,k',l} = \delta_{k,k'} \qquad \textstyle\sum_l\ \tilde{h}_{j,k,l}\ g_{j,m,l} = 0, \end{aligned} \tag{3.12}$$

for all $j \in \mathcal{J}$, and $k \in \mathcal{K}(j)$ and $m \in \mathcal{M}(j)$.

Proof. (Sketch) Given sets of primary and dual scaling basis functions, Eq. 3.6 together with Eq. 3.11 yields

$$\delta_{k,k'} = \langle \varphi_{j,k}\,,\,\tilde{\varphi}_{j,k'} \rangle = \left\langle \sum_l h_{j,k,l}\,\varphi_{j+1,l}\,,\,\sum_{l'} \tilde{h}_{j,k',l'}\,\tilde{\varphi}_{j+1,l'} \right\rangle.$$

It follows from the biorthogonality of the scaling basis functions that $\langle \varphi_{j,k}, \tilde{\varphi}_{j,k'} \rangle = 0$ if $k \neq k'$. Therefore only the case $k = k'$ with $\delta_{k,k} = 1$ has to be considered

$$1 = \left\langle \sum_l h_{j,k,l}\,\varphi_{j+1,l}\,,\,\sum_{l'} \tilde{h}_{j,k,l'}\,\tilde{\varphi}_{j+1,l'} \right\rangle.$$

From the properties of the inner product it follows that

$$1 = \sum_l \sum_{l'} h_{j,k,l}\,\tilde{h}_{j,k,l'}\,\langle \varphi_{j+1,l}\,,\,\tilde{\varphi}_{j+1,l'} \rangle\,.$$

Eq. 3.6 implies that $\langle \varphi_{j+1,l}, \tilde{\varphi}_{j+1,l'} \rangle = \delta_{l,l'}$ and therefore

$$1 = \sum_{l} h_{j,k,l}\, \tilde{h}_{j,k,l}.$$

Analogous derivations show that the other relationships in Eq. 3.12 hold. □

3.4.7 Wavelet Bases

A set of basis functions provides *perfect reconstruction* if the conditions in Eq. 3.12 hold, and [75]

$$\sum_{k} h_{j,k,l}\ \tilde{h}_{j,k,l} + \sum_{m} g_{j,m,l}\ \tilde{g}_{j,m,l} \ = \ 1. \tag{3.13}$$

Definition 11. A *biorthogonal wavelet basis* Ψ is a sequence

$$\Psi = \{\varphi_{0,0}\,,\ \psi_{j,m} \ \mid \ j \in \mathcal{J},\ m \in \mathcal{M}(j)\}\,,$$

where the basis functions provide perfect reconstruction. The primary basis functions of Ψ are denoted $\hat{\psi}_{j,m} \in \{\varphi_{0,0}, \psi_{j,m}\}$ with $\hat{\psi}_{-1,0} \equiv \varphi_{0,0}$, and analogously $\breve{\psi}_{j,m} \in \left\{\tilde{\varphi}_{0,0}, \tilde{\psi}_{j,m}\right\}$ with $\breve{\psi}_{-1,0} \equiv \tilde{\varphi}_{0,0}$ for the dual basis functions .

A function $f \in L_2$ can be represented in a wavelet basis as

$$f \ = \ \sum_{i \in \mathcal{I}} \left\langle f\,,\, \breve{\psi}_i \right\rangle \ \hat{\psi}_i \ = \ \sum_{i \in \mathcal{I}} \gamma_i\ \hat{\psi}_i, \tag{3.14}$$

where the γ_i are the basis function coefficients, and $i \in \mathcal{I}$ is a general index set defined over all basis functions of Ψ. Note that the basis functions form a forest and $\mathcal{I}$ results from the linear ordering of the forest.

The second generation setting assumes biorthogonal wavelets. For orthogonal wavelet bases, the primary and dual basis functions coincide for all j and m [76], or, equivalently, every basis function is orthogonal to every other basis function [87]. Orthogonal wavelets are therefore a subset of biorthogonal wavelet bases. It can be shown that the perfect reconstruction condition in Eq. 3.13 is satisfied for all orthogonal wavelet bases.

3.4.8 Fast Wavelet Transform

The *fast wavelet transform* is a pair of efficient linear-time algorithms for computing the wavelet transforms of a signal. The forward transform projects a signal into the wavelet basis and yields the basis function coefficients for all levels $j > n$, where n is a finest level on which the scaling function coefficients are known. The inverse wavelet transform reconstructs a signal from its basis representation.

Theorem 2. *Let Ψ be a wavelet basis, and $\varphi_{j,k}$, with $j \in \mathcal{J}$ and $k \in \mathcal{K}(j)$, be the associated scaling basis functions, and let S be a signal represented in the basis formed by the scaling functions at a level n.*

The projection of S into the wavelet basis Ψ and the reconstruction of the signal from its basis representation can be computed efficiently by recursively performing analysis and synthesis steps, respectively.

An analysis step of the fast wavelet transform is given by

$$\lambda_{j,k} = \sum_l \tilde{h}_{j,k,l}\ \lambda_{j+1,l} \quad \textit{and} \quad \gamma_{j,m} = \sum_l \tilde{g}_{j,m,l}\ \lambda_{j+1,l}, \tag{3.15}$$

and computes the basis function coefficients at level j as linear combination of the scaling function coefficients at level $j+1$. A synthesis step takes the form

$$\lambda_{j+1,l} \ = \ \sum_k h_{j,k,l}\ \lambda_{j,k} \ + \ \sum_m g_{j,m,l}\ \gamma_{j,m}, \tag{3.16}$$

and reconstructs the scaling function coefficients at level $j+1$ from the basis function coefficients at level j.

Proof. (Sketch) From Theorem 1 it is known that the basis function coefficient associated with a wavelet basis function $\psi_{j,m}$ can be obtained as

$$\gamma_{j,m} = \left\langle S\,,\, \tilde{\psi}_{j,m} \right\rangle.$$

From the refinement relationship in Eq. 3.10 it follows that

$$\gamma_{j,m} = \left\langle S\,,\, \sum_l \tilde{g}_{j,m,l}\ \tilde{\varphi}_{j+1,l} \right\rangle.$$

With the signal in its basis representation at level $j+1$, we can write

$$\gamma_{j,m} = \left\langle \sum_{k' \in \mathcal{K}(j+1)} \lambda_{j+1,k'} \ \varphi_{j+1,k'} + \sum_{m' \in \mathcal{M}(j+1)} \gamma_{j+1,m'} \ \psi_{j+1,m'} \ , \ \sum_{l} \tilde{g}_{j,m,l} \ \tilde{\varphi}_{j+1,l} \right\rangle,$$

and with the definition of the inner product it follows that

$$\gamma_{j,m} = \sum_{k' \in \mathcal{K}(j+1)} \sum_{l} \lambda_{j+1,k'} \ \tilde{g}_{j,m,l} \ \langle \varphi_{j+1,k'} \ , \ \tilde{\varphi}_{j+1,l} \rangle + \sum_{m' \in \mathcal{M}(j+1)} \sum_{l} \gamma_{j+1,m'} \ \tilde{g}_{j,m,l} \ \langle \psi_{j+1,m'} \ , \ \tilde{\varphi}_{j+1,l} \rangle$$

The biorthogonality of the scaling basis functions $\langle \varphi_{j,k} \ , \ \tilde{\varphi}_{j,k'} \rangle = \delta_{k,k'}$ and $\langle \psi_{j,m} \ , \ \tilde{\varphi}_{j,k} \rangle = 0$ [76] yields

$$\gamma_{j,m} = \sum_{l} \tilde{g}_{j,m,l} \ \lambda_{j+1,l}.$$

The proofs for the other equations of the fast wavelet transform are analogous. □

In general, the relationship between the scaling function coefficients at a finest level n and a signal can only be approximated [5]. For Haar-like bases an exact computation of the coefficients is possible.

Theorem 3. *Let $S = \sum_{k \in \mathcal{K}(n)} s_{n,k} \ \chi_{n,k}$ be a discrete signal defined over the domains of a partition at level n, and let Ψ be a Haar-like wavelet basis defined over the same partition with the associated scaling functions $\varphi_{j,k} = \eta_{j,k} \chi_{j,k}$, with $j \in \mathcal{J}$ and $k \in \mathcal{K}(j)$, where $\eta_{j,k}$ is a normalization factor. The scaling function coefficients of S in Ψ at level n are $\lambda_{n,k} = \frac{s_{n,k}}{\eta_{n,k}}$.*

Proof. It is easy to see that the sequence $\{\varphi_{n,k}\}_{k \in \mathcal{K}(n)}$ is a basis of the space over which S is defined. From the representation of the discrete signal it follows that

$$\begin{aligned} S &= \sum_{k \in \mathcal{K}(n)} \frac{\eta_{n,k}}{\eta_{n,k}} \ s_{n,k} \ \chi_{n,k} \\ &= \sum_{k \in \mathcal{K}(n)} \frac{s_{n,k}}{\eta_{n,k}} \ \varphi_{n,k} \\ \Rightarrow \lambda_{n,k} &= \frac{s_{n,k}}{\eta_{n,k}}. \end{aligned}$$

To obtain the original signal from its wavelet representation the normalization has to be cancelled, that is $s_{n,k} = \eta_{n,k} \ \lambda_{n,k}$. □

Chapter 4

SOHO Wavelets

In this section we will derive the SOHO wavelet basis. To our knowledge this is the first spherical Haar wavelet basis that is both orthogonal and symmetric. A novel subdivision scheme of the sphere, which is used to construct the partition, enables us to obtain the basis. The properties of the SOHO wavelets make the basis well suited for the approximation and processing of all-frequency signals on the sphere.

The SOHO wavelet basis spans the space $L_2 \equiv L_2(\mathbb{S}^2, d\omega)$ of functions with finite energy on the sphere. The standard area measure $d\omega$ on $\mathbb{S}^2$ is defined as $d\omega \equiv d\omega(\theta, \phi) = \sin(\theta)\ d\theta\ d\phi$, where $\omega = (\theta, \phi)$ are the polar coordinates of a point on the unit sphere, and $\theta \in [0, \pi]$ and $\phi \in [0, 2\pi]$.

4.1 The Partition Scheme

The SOHO wavelet basis is defined over a partition $\mathcal{P} = \{T_{j,k} \mid j \in \mathcal{J}, k \in \mathcal{K}(j)\}$. The domains $T_{0,k}$ at the coarsest level are obtained by projecting a platonic solid with triangular faces onto the sphere. The domains at the next finer level are formed by a 4-fold subdivision. Every $T_{j,k}$ has therefore four child domains $T^k_{j+1,l}$. As shown in Figure 4.1,

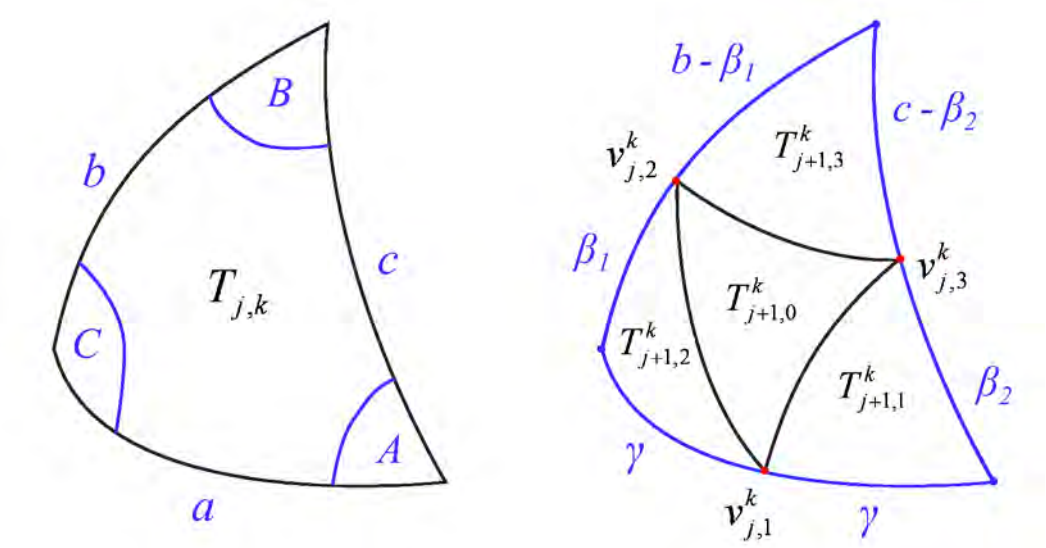

Figure 4.1: Subdivision of a spherical triangle.

these are obtained by inserting one new vertex $v^k_{j,l}$ on each of the arcs forming the sides of $T_{j,k}$. The domains at the coarsest level $T_{0,k}$ are therefore the root nodes of a set of partition trees and $\mathcal{P}$ is formed by the union of these trees.

In contrast to the partition used by Schröder and Sweldens [76], we do not employ the geodesic bisector to define the new vertex positions. Instead we constructed a partition for which the three outer child triangles $T^k_{j+1,1}$, $T^k_{j+1,3}$, and $T^k_{j+1,3}$ have equal area. This is the key to the derivation of a basis which is both orthogonal and symmetric. In Section 4.4 the definition of the subdivision scheme employed in our work will be detailed.

The characteristic function $\tau_{j,k} \equiv \tau_{j,k}(\omega)$ of the spherical triangle $T_{j,k}$ is defined as

$$\tau_{j,k}(\omega) = \begin{cases} 1 & \text{if } \omega \in T_{j,k}, \\ 0 & \text{otherwise.} \end{cases}$$

The area of $T_{j,k}$ will be denoted $\alpha_{j,k}$ with

$$\alpha_{j,k} = \int_{\mathbb{S}^2} \tau_{j,k}(\omega) d\omega = \int_{T_{j,k}} d\omega.$$

4.2 Scaling Basis Functions

For a Haar-like basis, the scaling basis functions $\varphi_{j,k}$ are constant over their support $T_{j,k}$ so that

$$\varphi_{j,k} = \eta_{j,k}\ \tau_{j,k},$$

where $\eta_{j,k}$ is a normalization constant that is chosen so that the scaling functions satisfy Eq. 3.6. It follows immediately from the disjoint nature of the $T_{j,k}$, for fixed j, that the scaling basis functions on the same level j are orthogonal, that is $\langle \varphi_{j,k}, \varphi_{j,k'} \rangle = 0$ if $k \neq k'$. With the definition of the inner product on $\mathbb{S}^2$, the normalization constant is

$$\begin{aligned}
\int_{\mathbb{S}^2} \varphi_{j,k}\ \varphi_{j,k}\ d\omega &= 1 \\
\int_{T_{j,k}} (\eta_{j,k}\ \tau_{j,k})\,(\eta_{j,k}\ \tau_{j,k})\,d\omega &= 1 \\
\eta_{j,k}^2 \int_{T_{j,k}} d\omega &= 1 \\
\eta_{j,k}^2 \alpha_{j,k} &= 1 \\
\Rightarrow \eta_{j,k} &= \frac{1}{\sqrt{\alpha_{j,k}}}.
\end{aligned}$$

The scaling functions for the SOHO wavelet basis are thus

$$\varphi_{j,k} = \frac{\tau_{j,k}}{\sqrt{\alpha_{j,k}}}. \tag{4.1}$$

An example for a scaling basis function at level 0 is shown in Figure 4.2. Given the $\varphi_{j,k}$, the filter coefficients $h_{j,k,l}$ have to be chosen so that the refinement relationship in Eq. 3.7 is satisfied:

$$\begin{aligned}
\varphi_{j,k} &= \sum_{l \in \mathcal{L}(j,k)} h_{j,k,l}\ \varphi_{j+1,l} \\
\frac{\tau_{j,k}}{\sqrt{\alpha_{j,k}}} &= \sum_{l \in \mathcal{L}(j,k)} h_{j,k,l}\ \frac{\tau^k_{j+1,l}}{\sqrt{\alpha^k_{j+1,l}}}.
\end{aligned}$$

It follows from the partition that $\#\mathcal{L}(j,k) = 4$ and that the union of the $\tau^k_{j+1,l}$ is $\tau_{j,k}$. The filter coefficients are therefore

$$h_{j,k,l} = \frac{\sqrt{\alpha^k_{j+1,l}}}{\sqrt{\alpha_{j,k}}}. \tag{4.2}$$

Theorem 4. *For the filter coefficients in Eq. 4.2 and the partition $\mathcal{P}$ defined in Section 4.1, the cascade algorithm converges to the scaling functions defined in Eq. 4.1.*

Proof. Let $\{\lambda_{j_0,k} = \delta_{k,k_0} \mid k \in \mathcal{K}(j_0)\}$ be a Kronecker sequence for fixed but arbitrary $j_0 \in \mathcal{J}$ and $k_0 \in \mathcal{K}(j_0)$. The sequences $\{\lambda_{j,k} \mid k \in \mathcal{K}(j)\}$, for $j > j_0$, are generated recursively with

$$\lambda_{j+1,l} = \sum_{k \in \mathcal{K}(j,l)} h_{j,k,l}\ \lambda_{j,k}\ . \tag{4.3}$$

With the scaling function filter coefficients for the SOHO wavelets, Eq. 4.3 becomes

$$\lambda_{j+1,l} = \sum_{k \in \mathcal{K}(j,l)} \frac{\sqrt{\alpha^k_{j+1,l}}}{\sqrt{\alpha_{j,k}}}\ \lambda_{j,k}, \tag{4.4}$$

where $\#\mathcal{K}(j,l) = 1$ for the partition defined in Section 4.1. With $\lambda_{j_0,k_0} = 1$, recursively applying Eq. 4.4 yields

$$\begin{aligned} \lambda_{j+1,l} &= \frac{\sqrt{\alpha_{j+1,l}}}{\sqrt{\alpha_{j,k_m}}} \frac{\sqrt{\alpha_{j,k_m}}}{\sqrt{\alpha_{j-1,k_{m-1}}}} \cdots \frac{\sqrt{\alpha_{j_0+2,k_2}}}{\sqrt{\alpha_{j_0+1,k_1}}} \frac{\sqrt{\alpha_{j_0+1,k_1}}}{\sqrt{\alpha_{j_0,k}}} \lambda_{j_0,k_0} \\ &= \frac{\sqrt{\alpha_{j+1,l}}}{\sqrt{\alpha_{j_0,k_0}}}. \end{aligned} \tag{4.5}$$

The coefficients $\lambda_{j,k}$ in Eq. 4.4 and Eq. 4.5 are normalized. It was shown in Section 3.4.8 that for a Haar-like basis the scaling function coefficients $\lambda_{j,k}$ must be denormalized to obtain the original signal; for the cascade algorithm this is $f^{(j)}_{j_0,k_0}$ as defined in Equation 3.8.

With the normalization constant $\eta_{j,k} = 1/\sqrt{\alpha_{j,k}}$ and the characteristic function $\tau_{j,k}$, the limit of Eq. 3.8 for $j \to \infty$ becomes

$$f^{(\infty)}_{j_0,k_0} = \lim_{j \to \infty} \left(\sum_{k \in \mathcal{K}(j)} \frac{1}{\sqrt{\alpha_{j,k}}} \lambda_{j,k}\ \tau_{j,k} \right).$$

With Eq. 4.5 this simplifies to

$$f^{(\infty)}_{j_0,k_0} = \lim_{j\to\infty} \left(\sum_{k\in\mathcal{K}(j)} \frac{1}{\sqrt{\alpha_{j,k}}} \frac{\sqrt{\alpha_{j,k}}}{\sqrt{\alpha_{j_0,k_0}}} \tau_{j,k} \right)$$

yielding

$$f^{(\infty)}_{j_0,k_0} = \frac{1}{\sqrt{\alpha_{j_0,k_0}}} \lim_{j\to\infty} \left(\sum_{k\in\mathcal{K}(j)} \tau_{j,k} \right). \tag{4.6}$$

It follows from the definition of the partition that the union of the $\tau_{j,k}$, which form the complete set of descendants of τ_{j_0,k_0} at a fixed but arbitrary level j, is τ_{j_0,k_0}. Eq. 4.6 can then be written as

$$f^{(\infty)}_{j_0,k_0} = \frac{1}{\sqrt{\alpha_{j_0,k_0}}} \tau_{j_0,k_0},$$

showing that the limit functions $f^{(\infty)}_{j_0,k_0}$ are identical to the scaling functions of the SOHO wavelet basis defined in Eq. 4.1. □

4.3 Wavelet Basis Functions

We use a custom two-step approach to derive the wavelet basis functions for the SOHO wavelets: In the first step we develop a semi-orthogonal basis, and in the second step orthogonality and symmetry are enforced.

For a Haar-like basis, the wavelet basis functions associated with a partition $T_{j,k}$ are exclusively defined over the child partitions $T^k_{j+1,l}$. Two wavelet basis functions $\psi_{j,m}$ and $\psi_{j,m'}$ defined on the same level j but over different partitions are thus trivially orthogonal. For $\langle \psi_{j,m}, \psi_{j',m'} \rangle = 0$ with $j \neq j'$ to be true, we require that the wavelet basis functions have a vanishing integral. To see that this in fact implies that the basis functions on different levels are orthogonal, two configurations have to be considered. Without loss of generality, let $j < j'$, and let $\psi_{j,m}$ and $\psi_{j',m'}$ be defined over $T_{j,k}$ and $T_{j',k'}$, respectively.

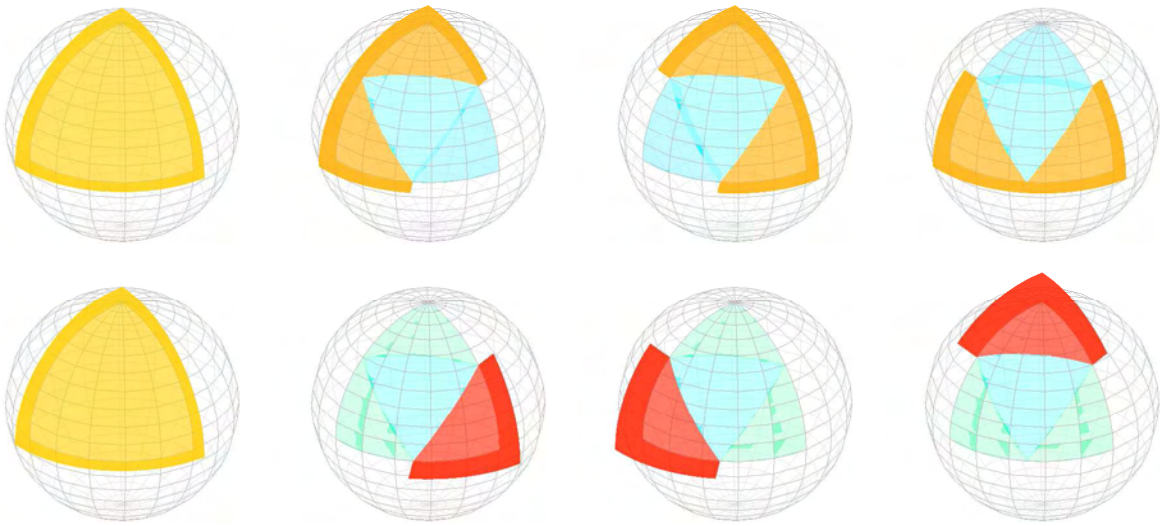

Figure 4.2: The scaling basis function and the three wavelet basis functions defined over a partition at level 0. The top row shows the basis functions where the plus sign has been employed in Eq. 4.15 to obtain a, the bottom row show the basis functions when the negative sign has been used. The basis is defined over a partition derived from an octahedron. Reddish tones indicate positive filter coefficients, bluish tones negative ones.

In case $T_{j',k'}$ is a child of $T_{j,k}$, it follows from the strictly nested nature of the partition that $\psi_{j,m}$ is constant over the support of $\psi_{j',m'}$. The vanishing integral of $\psi_{j',m'}$ then implies that the inner product of $\psi_{j,m}$ and $\psi_{j',m'}$ is zero. If $T_{j',k'}$ is not a child of $T_{j,k}$ then the support of the basis functions is disjoint. In this case the orthogonality is again trivial.

For a Haar-like basis for which the wavelet basis functions have a vanishing integral it is therefore sufficient to consider only one partition $T_{j,k}$, for fixed but arbitrary $j \in \mathcal{J}$ and $k \in \mathcal{K}(j)$, together with its child partitions $T^k_{j+1,l}$ for the derivation of the wavelet basis functions (cf. [7]). Similar to the scaling functions derived in Section 4.2, the result will be a definition of the wavelets basis functions as functions of j and k. To simplify the notation, the wavelet basis functions defined over $T_{j,k}$ will be denoted $\psi^i_{j,k}$, with $i = 1, 2, 3$, and the area of the partitions of interest will be abbreviated $\alpha_l \equiv \alpha^k_{j+1,l}$ and

$\alpha_p \equiv \alpha_{j,k}$; analogous notation will be used for the characteristic functions. In some cases we will also omit the indices j and k. It is then understood that these are the fixed j and k of $T_{j,k}$.

We already discussed the advantages of symmetric bases but did not yet provide a formal definition [58].

Definition 12. A spherical Haar wavelet basis is *symmetric* if the basis function coefficients associated with a partition $T_{j,k}$, for arbitrary but fixed $j \in \mathcal{J}$ and $k \in \mathcal{K}(j)$, are invariant to the labelling of the child domains $T^k_{j+1,1}$, $T^k_{j+1,2}$, and $T^k_{j+1,3}$.

This implies that we can change the labelling of $T^k_{j+1,1}$, $T^k_{j+1,2}$, and $T^k_{j+1,3}$, for a fixed parent partition, without changing the numerical values of the associated basis function coefficients (cf. Figure 4.1). Intuitively, this explains why symmetric bases provide visually superior results. Note again, that this definition of symmetry is unrelated to the concept of symmetry for first generation wavelets where it was a sufficient condition for the linear phase of a basis.

For a fixed partition $T_{j,k}$, the analysis and synthesis steps in Eq. 3.15 and Eq. 3.16 can be expressed as compact matrix-vector products. Perfect reconstruction requires that the product of the analysis and synthesis matrices $A_{j,k}$ and $S_{j,k}$, respectively, is the identity I, that is $A_{j,k}S_{j,k} = I$. This is equivalent to $A_{j,k} = S^{-1}_{j,k}$. Basic results from linear algebra imply the relationship simplifies to $A_{j,k} = S^T_{j,k}$ for an orthonormal basis. A synthesis step in matrix-vector notation takes the form

$$\begin{pmatrix} \lambda_{j+1,0} \\ \lambda_{j+1,1} \\ \lambda_{j+1,2} \\ \lambda_{j+1,3} \end{pmatrix} = \begin{pmatrix} h_{j,0} & g^0_{j,0} & g^1_{j,0} & g^2_{j,0} \\ h_{j,1} & g^0_{j,1} & g^1_{j,1} & g^2_{j,1} \\ h_{j,2} & g^0_{j,2} & g^1_{j,2} & g^2_{j,2} \\ h_{j,3} & g^0_{j,3} & g^1_{j,3} & g^2_{j,3} \end{pmatrix} \begin{pmatrix} \lambda_j \\ \gamma^0_j \\ \gamma^1_j \\ \gamma^2_j \end{pmatrix}, \tag{4.7}$$

where $g^i_{j,l}$ denotes the l^{th} filter coefficient associated with the i^{th} wavelet basis function $\psi^i_{j,k}$ defined over $T_{j,k}$, and the $h_{j,l}$ are the filter coefficients derived in Section 4.2. The vector

on the right hand side in Eq. 4.7 contains the basis function coefficients associated with $T_{j,k}$, and the result on the left hand side are the scaling function coefficients associated with the child domains of $T_{j,k}$.

A *semi-orthogonal* wavelet basis is a biorthogonal basis for which the wavelet basis functions are orthogonal to the scaling functions. For fixed $T_{j,k}$, this implies

$$\left\langle \psi^0_{j,k} \ , \ \varphi_{j,k} \right\rangle = \left\langle \psi^1_{j,k} \ , \ \varphi_{j,k} \right\rangle = \left\langle \psi^2_{j,k} \ , \ \varphi_{j,k} \right\rangle = 0. \tag{4.8}$$

Eq. 4.8 can be expressed in Dirac bra-ket notation:

$$[\langle \Phi_j \mid \Psi_j \rangle] = 0, \tag{4.9}$$

where $[\langle X \mid Y \rangle]$ denotes the matrix of inner products of the two function sets X and Y, and Φ_j and Ψ_j are the matrices containing the scaling and wavelet basis functions defined over $T_{j,k}$, respectively. Eq. 4.9 can be expanded with the refinement relationship in Eq. 3.10 [87, 24]:

$$[\langle \Phi_j \mid \Phi_{j+1} \rangle] \, G_j = 0.$$

The matrix Φ_j is degenerate, containing only $\varphi_{j,k}$, and Φ_{j+1} is formed by the four scaling basis functions $\varphi^k_{j+1,l}$ defined over the child partitions $T^k_{j+1,l}$. The matrix of inner products is thus

$$[\langle \Phi_j \mid \Phi_{j+1} \rangle] = \frac{1}{\sqrt{\alpha_p}} \left[\sqrt{\alpha_0}\, \tau_0, \sqrt{\alpha_1}\, \tau_1, \sqrt{\alpha_2}\, \tau_2, \sqrt{\alpha_3}\, \tau_3 \right].$$

G_j contains the desired wavelet basis function filter coefficients $g^i_{j,l}$. The matrix spans the nullspace of $[\langle \Phi_j \mid \Phi_{j+1} \rangle]$ and can therefore be obtained using existing techniques:

$$G_j = \begin{bmatrix} -\frac{\sqrt{\alpha_1}}{\sqrt{\alpha_0}} & -\frac{\sqrt{\alpha_2}}{\sqrt{\alpha_0}} & -\frac{\sqrt{\alpha_3}}{\sqrt{\alpha_0}} \\ 1 & 0 & 0 \\ 0 & 1 & 0 \\ 0 & 0 & 1 \end{bmatrix}. \tag{4.10}$$

Note that the wavelet basis functions defined in Eq. 4.10 are, up to a scaling factor, identical to those of the Bio-Haar wavelets proposed by Schröder and Sweldens [76]. As shown in the following the functions have a vanishing integral.

Proof. We want to show that

$$0 = \int_{\mathbb{S}^2} \psi^0_{j,k} \; d\omega.$$

Expanding this equation with the refinement relationship in Eq. 3.10 yields

$$\Omega \equiv \int_{\mathbb{S}^2} \psi^0_{j,k} \; d\omega = \int_{\mathbb{S}^2} \sum_l g^i_{j,l} \; \varphi_{j+1,l} \; d\omega.$$

Using the results from Eq. 4.10 gives

$$\Omega = \int_{\mathbb{S}^2} -\frac{\sqrt{\alpha_1}}{\sqrt{\alpha_0}} \frac{\tau_0}{\sqrt{\alpha_0}} + \frac{\tau_1}{\sqrt{\alpha_1}} \; d\omega.$$

The filter coefficients and the normalization constants do not depend on the integrand so that

$$\Omega = -\frac{\sqrt{\alpha_1}}{\sqrt{\alpha_0}\sqrt{\alpha_0}} \int_{\mathbb{S}^2} \tau_0 \; d\omega + \frac{1}{\sqrt{\alpha_1}} \int_{\mathbb{S}^2} \tau_1 \; d\omega.$$

Performing the integration then yields the result

$$\begin{aligned} \Omega &= -\frac{\sqrt{\alpha_1}}{\sqrt{\alpha_0}\sqrt{\alpha_0}} \alpha_0 + \frac{\alpha_1}{\sqrt{\alpha_1}} \\ &= -\sqrt{\alpha_1} + \sqrt{\alpha_1} \\ &= 0. \end{aligned}$$

The derivations for the other two wavelet basis functions are analogous. □

Given the semi-orthogonal basis derived above, we now have to enforce symmetry and orthogonality of the wavelet basis functions, thereby taking care to preserve the properties that have already been established. The intimate relationship between the filter coefficients and the basis functions thereby allows us to mainly consider the filter representation of the basis functions in the derivation, orthogonality of the basis functions can for example be guaranteed by requiring that the corresponding filter coefficient sequences are orthogonal.

With slight abuse of terminology, we can consider the basis derived so far as an "initial guess". Let $\tilde{S}_{j,k}$ be a synthesis matrix with the $g^i_{j,l}$ and $h_{j,l}$ derived previously. To obtain a basis that has all desired properties, we could augment each wavelet basis function coefficient in $\tilde{S}_{j,k}$ with an additional free parameter. A linear system could then be used to enforce the required properties of the wavelet basis. The solution of the system, if it exists, are the desired wavelet basis functions. However, we were not able to obtain a solution for the system. In fact, we believe at the moment that a solution might not exist.

We therefore decided to make the problem more tractable, requiring that the areas of the three outer child partitions be equal; in Section 4.4 it will be shown that the partition $\mathcal{P}$ can be constructed so that this constraint is satisfied. Given the area isometry of the three outer child triangles, symmetry can be guaranteed by the following parametrization of the synthesis matrix:

$$\tilde{S}_{j,k} = \begin{bmatrix} \frac{\sqrt{\alpha_0}}{\sqrt{\alpha_p}} & -c\,\frac{\sqrt{\alpha_1}}{\sqrt{\alpha_0}} & -c\,\frac{\sqrt{\alpha_1}}{\sqrt{\alpha_0}} & -c\,\frac{\sqrt{\alpha_1}}{\sqrt{\alpha_0}} \\ \frac{\sqrt{\alpha_1}}{\sqrt{\alpha_p}} & b & a & a \\ \frac{\sqrt{\alpha_1}}{\sqrt{\alpha_p}} & a & b & a \\ \frac{\sqrt{\alpha_1}}{\sqrt{\alpha_p}} & a & a & b \end{bmatrix}, \tag{4.11}$$

where a, b, and c are the remaining free parameters. We used a linear system derived from Eq. 4.11 to obtain a solution for the parameters. It follows from the symmetry of the wavelet basis functions and the area isometry of the three outer child partitions that three equations are sufficient to enforce the orthogonality of the basis functions and to preserve the already established properties:

$$0 = -c\,\frac{\sqrt{\alpha_1}}{\sqrt{\alpha_p}} + 2a\,\frac{\sqrt{\alpha_1}}{\sqrt{\alpha_p}} + b\,\frac{\sqrt{\alpha_1}}{\sqrt{\alpha_p}} \tag{4.12}$$

$$0 = c^2\frac{\alpha_1}{\alpha_0} + a^2 + 2ab \tag{4.13}$$

$$0 = -c\,\sqrt{\alpha_1} + 2a\,\sqrt{\alpha_1} + b\sqrt{\alpha_1}, \tag{4.14}$$

where the first equation guarantees semi-orthogonality, the second equation establishes

the orthogonality of the wavelet basis functions, and the last equation enforces the vanishing integral of the $\psi^i_{j,k}$. In fact, only two equations are necessary to enforce all constraints. It is easy to see that Eq. 4.12 and Eq. 4.14 are not linearly independent and differ only by a constant. One parameter can therefore be chosen freely. We set $c = 1$. The solution to the linear system gives the wavelet basis functions for the SOHO wavelet basis:

$$\begin{aligned}
\psi^0_{j,k} &= \frac{\Lambda_1}{\Lambda_0}\tau_0 \; + \frac{1}{\Lambda_1}(\; (-2a+1)\;\tau_1 \; + a\;\tau_2 \; + a\;\tau_3) \\
\psi^1_{j,k} &= \frac{\Lambda_1}{\Lambda_0}\tau_0 \; + \frac{1}{\Lambda_1}(\; a\;\tau_1 \; + (-2a+1)\;\tau_2 \; + a\;\tau_3) \\
\psi^2_{j,k} &= \frac{\Lambda_1}{\Lambda_0}\tau_0 \; + \frac{1}{\Lambda_1}(\; a\;\tau_1 \; + a\;\tau_2 \; + (-2a+1)\;\tau_3),
\end{aligned}$$

with

$$a = \frac{1 \pm \sqrt{1+3\Delta^2}}{3}, \tag{4.15}$$

where $\Lambda_l \equiv \sqrt{\alpha_l}$ and $\Delta = \sqrt{\alpha_1/\alpha_0}$. The area measures α_0 and α_1 are always positive and thus a in Eq. 4.15 is guaranteed to be real. Note that there are two solutions for a and therefore two different sets of wavelet basis functions. A side-by-side comparison of the two sets is shown in Figure 4.2.

An orthonormal basis can be obtained by augmenting the wavelet basis functions $\psi^l_{j,k}$ with the normalization constant

$$\varrho_{j,k} = \frac{1}{\sqrt{9a^2 - 6a + 1}}.$$

Proof. For a normalized basis the inner product of a wavelet basis function and itself has to satisfy

$$\left\langle \psi^i_{j,k}\,,\, \psi^i_{j,k} \right\rangle = 1.$$

Expanding the equation with the refinement relation in Eq. 3.10 and augmenting the wavelet basis function with a (yet unknown) normalization constant $\varrho_{j,k}$ yields

$$1 = \int_{S^2} \sum_l \varrho_{j,k}\; g^i_{j,l}\; \varphi^k_{j+1,l} \; \sum_{l'} \varrho_{j,k}\; g^i_{j,l'}\; \varphi^k_{j+1,l'}\; d\omega.$$

The support of the scaling basis functions at level $j+1$ is disjoint so that

$$1 = \sum_l \varrho_{j,k}^2 \left(g_{j,l}^i\right)^2 \int_{S^2} \left(\varphi_{j+1,l}^k\right)^2 \, d\omega.$$

The scaling basis functions are normalized and the integral in the last equation is therefore one. Expanding the sum then yields

$$\begin{aligned} 1 &= \varrho_{j,k}^2 \left(\frac{\alpha_1}{\alpha_0} + a^2 + a^2 + (1-2a)^2 \right) \\ &= \varrho_{j,k}^2 \left(\frac{\alpha_1}{\alpha_0} + 6a^2 - 4a + 1 \right). \end{aligned} \tag{4.16}$$

Solving Eq. 4.15 for α_1 gives $\alpha_1 = a\alpha_0 (3a-2)$. Employing this result in Eq. 4.16 yields

$$1 = \varrho_{j,k}^2 \left(\frac{\alpha_0 (3a^2 - 2a)}{\alpha_0} + 6a^2 - 4a + 1 \right).$$

The result then follows immediately

$$\varrho_{j,k} = \frac{1}{\sqrt{9a^2 - 6a + 1}}.$$

It follows from the symmetry of the SOHO wavelet basis that the normalization constant is identical for all three wavelet basis functions defined over $T_{j,k}$. □

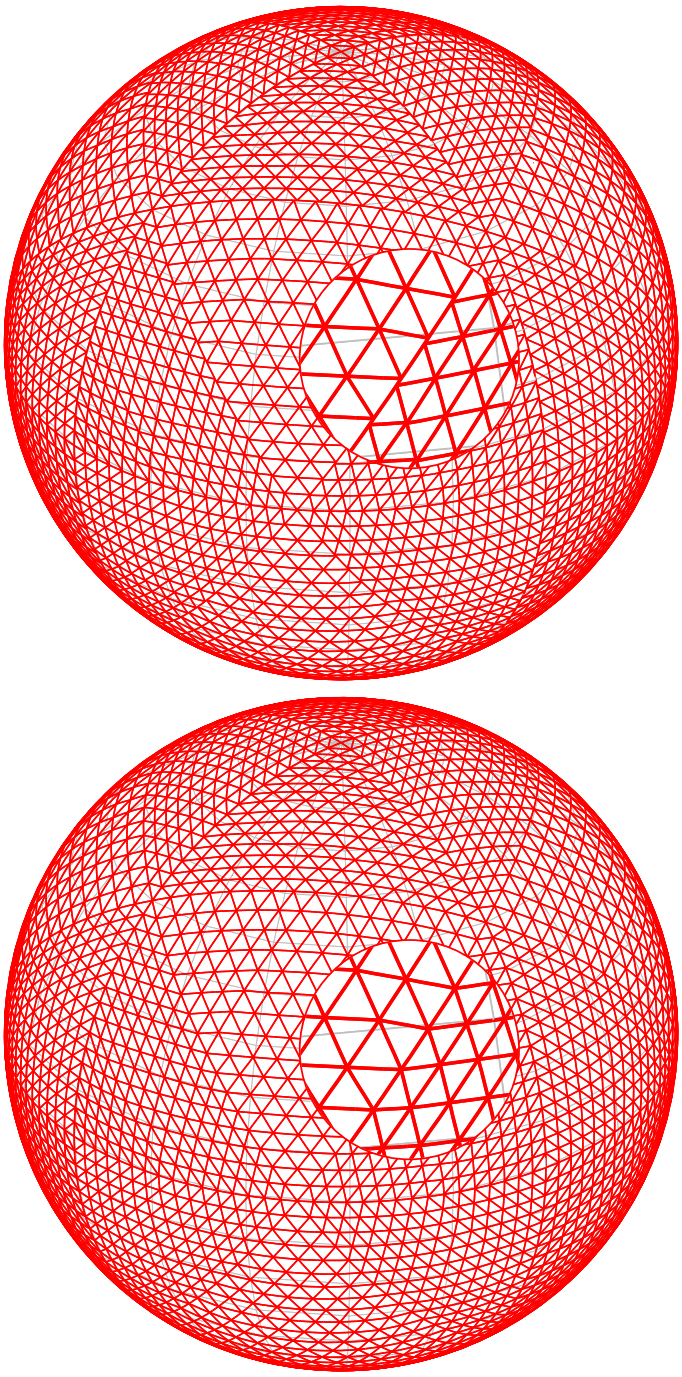

Figure 4.3: Differences between the equal-area subdivision developed for the SOHO wavelet basis (top) and the geodesic bisector subdivision employed by Schröder and Sweldens (bottom) [76]. It can be seen that our new subdivision scheme only slightly displaces the vertices from the geodesic bisector.

4.4 Construction of the Partition

In the last section it has been demonstrated that the SOHO wavelet basis can be constructed provided the three outer child triangles $T^k_{j+1,l}$, $T^k_{j+1,2}$, and $T^k_{j+1,3}$ of a partition $T_{j,k}$ have equal area. In this section we will introduce a novel subdivision scheme of the sphere that yields a partition satisfying this constraint.

In the following, we consider again only one partition $T_{j,k}$, with fixed but arbitrary $j \in \mathcal{J}$ and $k \in \mathcal{K}(j)$. Previous work positioned the vertices $v^k_{j,l}$ at the geodesic bisectors of the spherical edges a, b, and c of the parent domain $T_{j,k}$ (cf. Figure 4.1). This does not yield child triangles with equal area. However, $\mathcal{P}$, as defined in Section 4.1, only imposes a topology on the partition. The $v^k_{j,l}$ can therefore be positioned so that $\alpha_1 = \alpha_2 = \alpha_3$ (cf. [58]).

Let $v^k_{j,1}$ still be the geodesic bisector. The positions of $v^k_{j,2}$ and $v^k_{j,3}$ can then be obtained from a system of equations:

$$\cot\left(\frac{1}{2}E\right) = \cot(C) + \frac{\cot\left(\frac{1}{2}\beta_1\right)\cot\left(\frac{1}{2}\gamma\right)}{\sin(C)} \tag{4.17}$$

$$\cot\left(\frac{1}{2}E\right) = \cot(B) + \frac{\cot\left(\frac{1}{2}\beta_2\right)\cot\left(\frac{1}{2}\gamma\right)}{\sin(B)} \tag{4.18}$$

$$\cot\left(\frac{1}{2}E\right) = \cot(A) + \frac{\cot\left(\frac{1}{2}b - \frac{1}{2}\beta_1\right)\cot\left(\frac{1}{2}c - \frac{1}{2}\beta_2\right)}{\sin(A)}, \tag{4.19}$$

where we used Eq. 36 from the book by Todhunter [92] to define the equations. The variables on the right hand side of the equations are given in Figure 4.1, and E denotes the spherical excess of the three outer child partitions. Solving this system for β_1 and β_2 yields the positions of $v^k_{j,2}$ and $v^k_{j,3}$. The resulting formulae are lengthy and therefore omitted.

In the following it will be shown that only one solution for the vertex positions exists if the angles of the parent domain are labelled consistently. For the proof it is assumed that the partition is derived from an octahedron or an icosahedron.

Eq. 4.17, Eq. 4.18, and Eq. 4.19 have to be satisfied to obtain area isometry of the three outer child partitions. To show that only one configuration satisfies this constraint the following two equations will be examined

$$\cot(C) + \frac{\cot\left(\frac{1}{2}\beta_1\right)\cot\left(\frac{1}{2}\gamma\right)}{\sin(C)} = \cot(B) + \frac{\cot\left(\frac{1}{2}\beta_2\right)\cot\left(\frac{1}{2}\gamma\right)}{\sin(B)} \tag{4.20}$$

$$\cot(B) + \frac{\cot\left(\frac{1}{2}\beta_2\right)\cot\left(\frac{1}{2}\gamma\right)}{\sin(B)} = \cot(A) + \frac{\cot\left(\frac{1}{2}b - \frac{1}{2}\beta_1\right)\cot\left(\frac{1}{2}c - \frac{1}{2}\beta_2\right)}{\sin(A)}. \tag{4.21}$$

Eq. 4.20 and Eq. 4.21 state that the areas of child partitions two and three, α_2 and α_3, and child partitions two and one, α_2 and α_1, are equal, respectively. Both equations can be solved for β_1. The resulting functions $f_1(\beta_2)$ and $f_2(\beta_2)$ represent all (not necessarily valid) configurations so that $\alpha_2 = \alpha_3$ and $\alpha_2 = \alpha_1$, respectively. The area isometry of all outer child partitions is satisfied at the intersection point of $f_1(\beta_2)$ and $f_2(\beta_2)$. The objective in the following is therefore to show that the two functions $f_1(\beta_2)$ and $f_2(\beta_2)$ have exactly one intersection point for $\beta_1 \in (0, b]$ and $\beta_2 \in (0, c]$.

Remark 3. The angles A, B, and C are in $[0, \pi]$ and let

$$\begin{aligned} A_s &\equiv \sin(A) \quad A_c \equiv \cos(A) \quad A_t \equiv \cot(A) \\ B_s &\equiv \sin(B) \quad B_c \equiv \cos(B) \quad B_t \equiv \cot(B) \\ C_s &\equiv \sin(C) \quad C_c \equiv \cos(C) \quad C_t \equiv \cot(C). \end{aligned}$$

We will denote with a "bar" variables in cotangent space:

$$\bar{\gamma} \equiv \cot\left(\tfrac{1}{2}\gamma\right) \quad \bar{b} \equiv \cot\left(\tfrac{1}{2}b\right) \quad \bar{c} \equiv \cot\left(\tfrac{1}{2}c\right)$$

and

$$\bar{\beta}_1 \equiv \cot\left(\tfrac{1}{2}\beta_1\right) \quad \bar{\beta}_2 \equiv \cot\left(\tfrac{1}{2}\beta_2\right),$$

where $a = 2\gamma$, b, $c \in (0, \pi/2]$.

The inverse cotangent function $\operatorname{acot}(x)$ has a pole at $x = 0$ and further

$$\begin{aligned} \lim_{x\to\infty} \operatorname{acot}(x) &= 0 \qquad \lim_{x_+\to 0} \operatorname{acot}(x) = \infty \\ \lim_{x\to-\infty} \operatorname{acot}(x) &= 0 \qquad \lim_{x_-\to 0} \operatorname{acot}(x) = -\infty. \end{aligned}$$

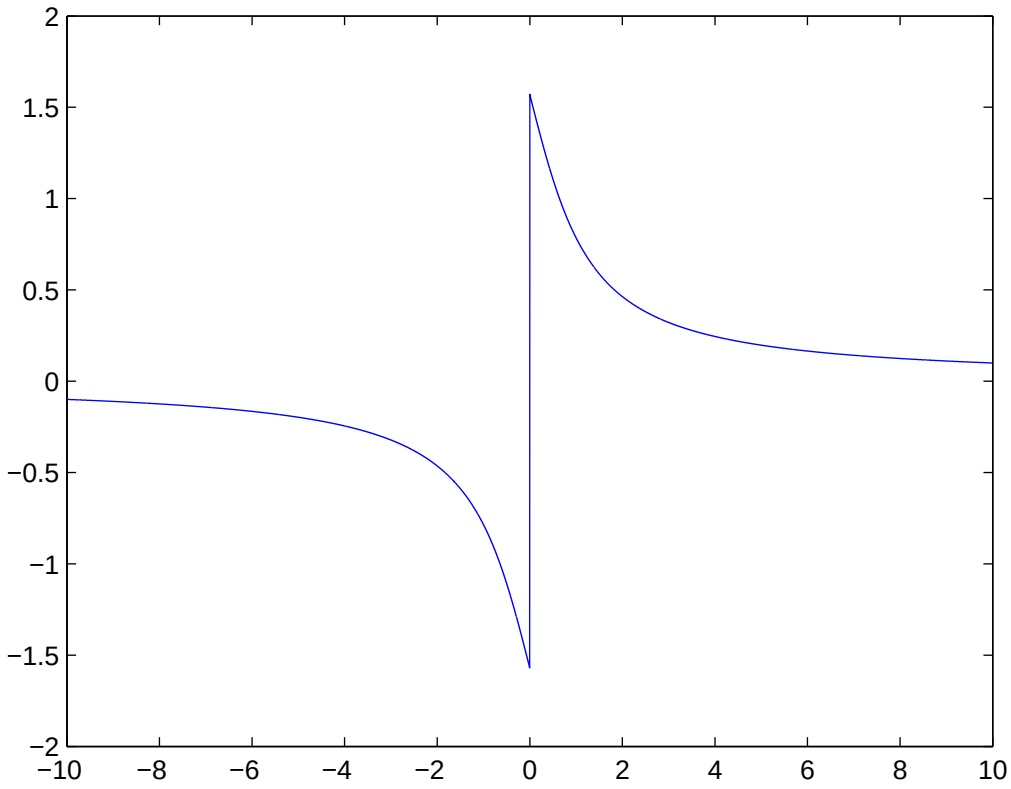

Figure 4.4: Inverse cotangent.

For $x \in (0, \infty]$ and $x \in [-\infty, 0)$ the inverse cotanget is continuous (cf. Figure 4.4).

Note that in cotangent space

$$\lim_{\beta_2 \to 0} \cot\left(\frac{1}{2}\beta_2\right) = \infty,$$

and the domains of interest are then $\bar{\beta}_1 \in [\bar{b}, \infty)$ and $\bar{\beta}_2 \in [\bar{c}, \infty)$. Using the notation introduced in Remark 3, the representations of $f_1(\beta_2)$ and $f_2(\beta_2)$ in cotangent space, $\bar{g}_1(\bar{\beta}_2)$ and $\bar{g}_2(\bar{\beta}_2)$, respectively, are

$$\bar{g}_1(\bar{\beta}_2) = \frac{C_s B_t}{\gamma} - \frac{C_c}{\bar{\gamma}} + \frac{C_s}{B_s}\bar{\beta}_2 \tag{4.22}$$

and

$$\bar{g}_2(\bar{\beta}_2) = -\frac{\bar{b}\bar{\gamma}A_s\bar{\beta}_2(\bar{\beta}_2 - \bar{c}) + B_s\left[1 + \bar{b}A_tA_s(\bar{c} - \bar{\beta}_2) + \bar{c}\bar{\beta}_2 + \bar{b}A_sB_t(\bar{\beta}_2 - \bar{c})\right]}{\bar{\gamma}A_s\bar{\beta}_2(\bar{c} - \bar{\beta}_2) + B_s\left[\bar{b} + A_sB_t(\bar{c} - \bar{\beta}_2) + \bar{b}\bar{c}\bar{\beta}_2 + A_tA_s(\bar{\beta}_2 - \bar{c})\right]}. \tag{4.23}$$

Here the identity

$$\cot(x - y) = \frac{-1 - \cot(x)\cot(y)}{\cot(x) - \cot(y)}$$

has been used for the derivation [2].

Lemma 1. *The function $\bar{g}_1(\bar{\beta}_2)$ does not have a root for $\bar{\beta}_2 \in [c, \infty)$.*

Proof. Eq. 4.22 is a linear equation in $\bar{\beta}_2$. Therefore, if both $\lim_{\bar{\beta}_2 \to \infty} \bar{g}_1(\bar{\beta}_2) > 0$ and $\bar{g}_1(c) > 0$ then the function may not be a root for $\bar{\beta}_2 \in [\bar{c}, \infty)$. It is easy to see that

$$\lim_{\bar{\beta}_2 \to \infty} \bar{g}_1(\bar{\beta}_2) = \infty,$$

and that

$$\begin{aligned}\bar{g}_1(\bar{c}) &= \frac{C_sB_t}{\bar{\gamma}} - \frac{C_c}{\bar{\gamma}} + \frac{C_s}{B_s}\bar{c} \\ &= \frac{C_c}{\bar{\gamma}}\left[\frac{C_s}{C_c}\frac{B_c}{B_s} - 1\right] + \frac{C_s}{B_s}\bar{c}.\end{aligned}$$

It follows from

$$\frac{C_c}{\bar{\gamma}}\left[\frac{C_s}{C^c}\frac{B_c}{B_s} - 1\right] > 0 \tag{4.24}$$

that $\bar{g}_1(\bar{c}) > 0$. To see that Eq. 4.24 is true, four different configurations have to be considered. Without loss of generality, the angles in the parent triangle are defined so that the following statements are true:

- $B < \frac{\pi}{2}$ and $C < \frac{\pi}{2}$: $B < C$.
- $B > \frac{\pi}{2}$ and $C > \frac{\pi}{2}$: $B > C$.
- One angle is greater than $\frac{\pi}{2}$ and one angle is smaller: $B < \frac{\pi}{2}$ and $C > \frac{\pi}{2}$.
- At least one angle equals $\frac{\pi}{2}$: $C = \frac{\pi}{2}$.

It is easy to verify that in each case Eq. 4.24 holds. □

Lemma 2. *The function $\bar{g}_2(\bar{\beta}_2)$ does not have a root for $\bar{\beta}_2 \in [\bar{c}, \infty)$.*

Proof. For $\bar{g}_2(\bar{\beta}_2)$ to have a root in $\bar{\beta}_2 \in [\bar{c}, \infty)$ the numerator in Eq. 4.23, in the following denoted by $\bar{h}(\bar{\beta}_2)$, has to have a root in the interval. The number of terms in $\bar{h}(\bar{\beta}_2)$ makes it difficult to directly show that there are no roots in the domain of interest. It will therefore be shown that $\lim_{\bar{\beta}_2 \to \infty} \bar{h}(\bar{\beta}_2)$ and $\bar{h}(\bar{c})$ are strictly positive and that the equation does not have a critical point in $\bar{\beta}_2 \in [\bar{c}, \infty)$. This implies that the quadratic equation $\bar{h}(\bar{\beta}_2)$ has no root in the interval of interest.

For $\bar{\beta}_2 \to \infty$ it is again easy to see that

$$\lim_{\bar{\beta}_2 \to \infty} \bar{h}(\bar{\beta}_2) = \infty.$$

With $\bar{\beta}_2 = c$ it follows that

$$\begin{aligned}
\bar{h}(\bar{c}) &= \bar{b}\bar{\gamma}A_s\bar{\beta}_2(\bar{c} - \bar{c}) + B_s\left[1 + \bar{b}A_tA_s(\bar{c} - \bar{c}) + \bar{c}^2 + \bar{b}A_sB_t(\bar{c} - \bar{c})\right] \\
&= B_s + B_s\bar{c}^2 \\
&> 0.
\end{aligned}$$

The derivative $\frac{d\bar{h}(\bar{\beta}_2)}{d\bar{\beta}_2} = \bar{h}'(\bar{\beta}_2)$ is given by

$$\bar{h}'(\bar{\beta}_2) = (\bar{c} - \bar{b}A_tA_s + \bar{b}A_sB_t)B_s + \bar{b}A_s\bar{\beta}_2 + \bar{b}\bar{\gamma}A_s(\bar{\beta}_2 - \bar{c}),$$

which is a linear equation in $\bar{\beta}_2$. Again examining the function values at the boundaries of the interval of interest shows that

$$\lim_{\bar{\beta}_2 \to \infty} \bar{h}'(\bar{\beta}_2) = \infty,$$

and

$$\begin{aligned}
\bar{h}'(\bar{c}) &= (\bar{c} - \bar{b}A_tA_s + \bar{b}A_sB_t)B_s + \bar{b}A_s\bar{c} + \bar{b}\bar{\gamma}A_s(\bar{c} - \bar{c}) \\
&= (\bar{c} - \bar{b}A_tA_s + \bar{b}A_sB_t)B_s + \bar{b}A_s\bar{c} + \bar{b}\bar{\gamma}A_s(\bar{c} - \bar{c}) \\
&= (\bar{c} + \bar{b}A_s(B_t - A_t)))B_s + \bar{b}A_s\bar{c}.
\end{aligned}$$

As with the inverse cotangent, the cotangent function $\cot(x)$ is monotonic for $x \in (0, \infty]$ and $x \in [-\infty, 0)$. Without loss of generality, choosing A and B so that $B > A$ then guarantees that $\bar{h}'(\bar{c}) > 0$. This implies that the derivative has no root for $\bar{\beta}_2 \in [\bar{c}, \infty)$ and it follows that $\bar{g}_2(\bar{\beta}_2)$ does not have a root in the interval of interest. □

Theorem 5. *The functions $f_1(\beta_2)$ and $f_2(\beta_2)$ have exactly one intersection point for $\beta_2 \in (0, c]$, and $\beta_1 \in (0, b]$ is satisfied for this point.*

Proof. It follows from Lemma 1 and Lemma 2 and the properties of the inverse cotangent that $f_1(\beta_2)$ and $f_2(\beta_2)$ are continuous and monotonic for $\beta_2 \in (0, c]$. Applying the inverse cotangent to the results obtained in the proof of Lemma 1 shows that

$$\lim_{\beta_2 \to 0} f_1(\beta_2) = 0 \quad \text{and} \quad f_1(c) > 0.$$

The function values of $\bar{g}_2(\bar{\beta}_2)$ at the boundaries of the interval of interest are

$$\lim_{\bar{\beta}_2 \to \infty} \bar{g}_2(\bar{\beta}_2) = -\frac{\bar{\beta}_2^2}{\bar{\beta}_2^2} \left(\frac{\bar{b}\bar{\gamma}A_s + 0}{-\bar{\gamma}A_s + 0} \right) = \bar{b}$$

and

$$\begin{aligned} \bar{g}_2(\bar{c}) &= -\frac{\bar{b}\bar{\gamma}A_s\bar{\beta}_2(\bar{c} - \bar{c}) + B_s\left[1 + \bar{b}A_tA_s(\bar{c} - \bar{c}) + \bar{c}^2 + \bar{b}A_sB_t(\bar{c} - \bar{c})\right]}{\bar{\gamma}A_s\bar{\beta}_2(\bar{c} - \bar{c}) + B_s\left[\bar{b} + A_sB_t(\bar{c} - \bar{c}) + \bar{b}\bar{c}^2 + A_tA_s(\bar{c} - \bar{c})\right]} \\ &= -\frac{B_s + \bar{c}^2}{B_s\bar{b} + \bar{b}\bar{c}^2} \\ &= -\frac{1}{\bar{b}}, \end{aligned}$$

and therefore

$$\lim_{\beta_2 \to 0} f_2(\beta_2) = 2\ \mathrm{acot}\left(\cot\left(\frac{1}{2}b\right)\right) > 0 \quad \text{and} \quad f_2(c) = 2\ \mathrm{acot}\left(-\frac{1}{\cot\left(\frac{1}{2}b\right)}\right) < 0.$$

Note that here is no contradiction with Lemma 2. The function $\bar{g}_2(\bar{\beta}_2)$ has a pole for $\bar{\beta}_2 \in [\bar{c}, \infty)$ in cotangent space which yields a root of $f_2(\beta_2)$. Of importance for the proof is however only that $f_2(\beta_2)$ is continuous for $\beta_2 \in (0, c]$. This is assured by the fact that $\bar{g}_2(\bar{\beta}_2)$ has no root in the interval of interest.

Subdivision Scheme	Octahedron		Icosahedron	
Level	5	7	5	7
Our subdivision	43.0864	43.0417	53.5981	53.5808
Geodesic midpoint	45.0345	45.0022	54.0163	54.0010

Table 4.1: Shape distortion for the partition proposed in this thesis and the geodesic bisector subdivision employed by Schröder and Sweldens [76]. The minimum internal angle (in degrees) over all partitions was used as distortion measure.

The monotonicity of $f_1(\beta_2)$ and $f_2(\beta_2)$ now implies that there must exist exactly one intersection point between the two functions for $\beta_2 \in (0, c]$. From the function values of $f_1(\beta_1)$ at the boundaries of $\beta_2 \in (0, c]$ it follows that $\beta_1 \in (0, b]$. The intersection point is the desired configuration where the area of the three outer child triangles is equal (cf. Fig 4.5). □

For the partition $\mathcal{T}$ it is desirable to yield spherical triangles that are uniform so that the arc lengths and the angles of the domains are equal. We have not yet been able to prove bounds on the distortion introduced by our subdivision scheme. Numerical experiments show however that it is not significantly larger than that for the geodesic bisector subdivision. We used the minimum internal angle over all partitions to measure the shape distortion. The results are given in Table 4.1.

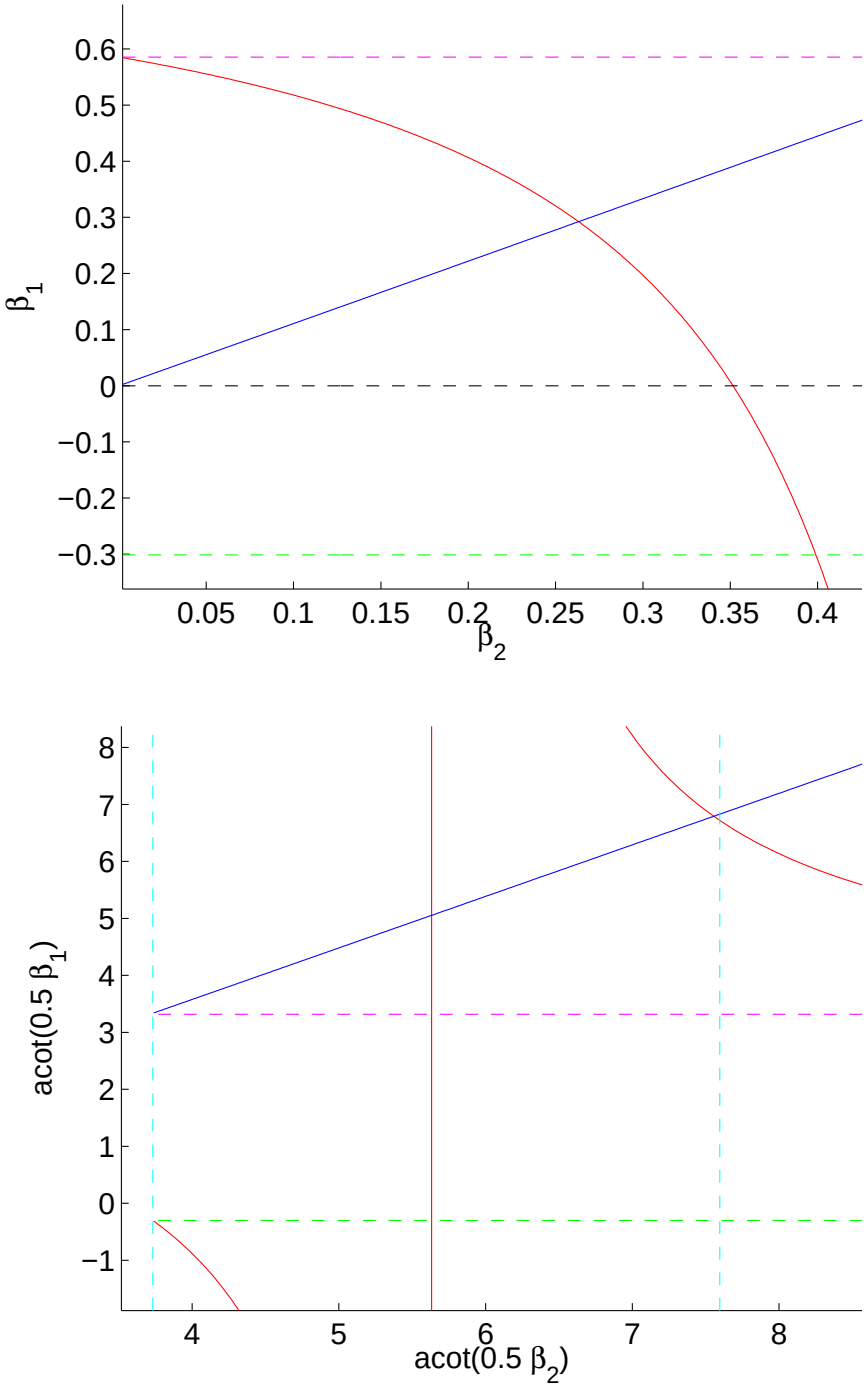

Figure 4.5: In the top figure $f_1(\beta_2)$ (blue) and $f_2(\beta_2)$ (red) are shown, $\bar{g}_1(\bar{\beta}_2)$ (blue) and $\bar{g}_2(\bar{\beta}_2)$ (red) are graphed in the bottom plot. The limits for the functions are shown in magenta and green.

4.5 Unconditional Basis Property

In this section we will provide a proof which shows that the SOHO wavelets are an orthonormal basis of $L_2 \equiv L_2(\mathbb{S}^2, d\omega)$. In a first step, it will be verified that the wavelets developed in this thesis are an unconditional basis of L_2. The result then follows immediately from the orthogonality of the basis functions. The proof is based on the results by Girardi and Sweldens [31] and these authors deserve the most credit for the derivation.

In Section 3.1.3 a definition for an unconditional basis has already been provided. For the proof we will employ an alternative, more practical one [31, 14]:

Theorem 6. *A sequence of functions $\{e_k\}_{k=1}^m$ is an unconditional basis for a Banach space X if for every $f \in X$ a unique family $\{c_k\}_{k=1}^m$ of real numbers exists so that $\sum_{k=1}^m c_k\, e_k$ converges unconditionally to f. This is true iff the following two conditions hold:*

(C1) $\operatorname{clos}\operatorname{span}\{e_k\}_{k=1}^m = X$

(C2) *A constant Γ exists so that for all finite subsets $K \subset \mathbb{Z}^+ \setminus 0$*

$$\left\| \sum_{k\in K} \epsilon_k\ c_k\ e_k \right\|_p \leq \Gamma \left\| \sum_{k\in K} c_k\ e_k \right\|_p , \tag{4.25}$$

for all choices of $c_k \in \mathbb{R}$ and $\epsilon_k = \pm 1$. For fixed p, the smallest Γ for which the inequality holds is the unconditional basis constant Γ_p.

See for example the book by Christensen [14] for a proof. Note that the ϵ_k guarantee that the sequence $\sum_{k=1}^m c_k\ e_k$ converges unconditionally.

To prove that the SOHO wavelets are an unconditional basis of L_2 we will show that conditions (C1) and (C2) in Theorem 6 hold. As detailed in Section 4.1, the SOHO wavelet basis is defined over a forest of partition trees. The disjoint nature of the trees implies that it is sufficient to show that Theorem 6 holds for a basis defined over one partition tree $\mathcal{T}$ (cf. [31]). We will employ the index set $\mathcal{H}$ defined over $\mathcal{T}$ for the proof.

For convenience, we define the set $G(\triangle) \in \mathcal{H}$ with $\#(G(\triangle)) = \#(C(\triangle) - 1)$ to index the wavelet basis functions defined over a partition $\tau_\triangle$, $\triangle \in \mathcal{H}$. Note that

$$\mathcal{I} = \left(\bigcup_{\triangle \in \mathcal{T}} G(\triangle) \right) \cup \varphi_{0,0},$$

where $\mathcal{I}$ is defined as in Section 3.4.5 and denotes an index set over all basis functions.

Remark 4. Consider the equality

$$\text{span}\left\{\varphi_\triangledown \mid \triangledown \in C(\triangle)\right\} = \text{span}\left\{\varphi_\triangle, \psi_\gamma \mid \gamma \in G(\triangle)\ \right\}, \tag{4.26}$$

where $\triangle, \triangledown \in \mathcal{H}$. To verify that the sequences on the left and right hand side of Eq. 4.26 are in fact identical we examine their properties using basic results from the previous sections:

1. The functions in each set are orthogonal.
2. The cardinality of both sets is identical.
3. Both sets are defined over the same set of partitions, namely $\{\tau_\triangledown \mid \triangledown \in C(\triangle)\}$.

The third property implies that the sequences in Eq. 4.26 are defined over the same space and it follows from property one and property two that the sequences are bases. Thus the sequences are two different orthogonal bases of the same space. From the refinement relationships for the scaling and wavelet basis functions it follows that

$$\text{span}\left\{\varphi_\triangledown \mid \triangledown \in C^i(\triangle)\right\} = \text{span}\left\{\varphi_\triangle, \psi_\gamma \mid \gamma \in \bigcup_{k=0}^{i-1} G(C^k(\triangle))\right\}, \tag{4.27}$$

for fixed i.

Remark 5. It follows from the definition of a partition that

$$L_2 = \text{clos}\,\text{span}\left\{\tau_\triangle \mid \triangle \in \mathcal{H}\right\}. \tag{4.28}$$

From the definition of the scaling functions it then follows immediately that

$$L_2 = \text{clos span}(\Phi), \tag{4.29}$$

where $\Phi = \{\varphi_\triangle \mid \triangle \in \mathcal{H}\}$.

Lemma 3.

$$L_2 = \text{clos span}(\Psi)$$

Proof. With Eq. 4.29 it is sufficient to prove that

$$\tau_\delta \in \text{clos}\,\text{span}(\Psi) \quad , \quad \forall \delta \in \mathcal{H}. \tag{4.30}$$

From the definition of a wavelet basis it is known that $\varphi_{0,0} \in \Psi$. Eq. 4.30 therefore trivially holds when δ is the root node of $\mathcal{H}$. In the following it is therefore assumed that $g(\delta) \geq 0$. Let $\triangle \in \mathcal{H}$ be of the form $\triangle = p^i(\delta)$ for some $i > 0$. We define the function f_i as

$$f_i = \tau_\delta - \frac{\alpha_\delta}{\alpha_\triangle}\tau_\triangle. \tag{4.31}$$

Now consider Eq. 4.27 where the indices for i and $\triangle$ correspond to those in this proof. Obviously, τ_δ is in the span of the left hand side of Eq. 4.27, and $\tau_\triangle$ is in the span because it can be defined in terms of its descendants using the refinement relationship in Eq. 3.7. Thus, f_i is in the span of the sequence on the left hand side of Eq. 4.27. It then follows immediately that f_i is also in the span of the sequence one the right hand side of this equation.

By construction, f_i has a vanishing integral. The scaling function $\varphi_\triangle$ on the right hand side of Eq. 4.27 is constant over the support of f_i. Therefore, $\langle \varphi_\triangle, f_i \rangle = 0$, that is f_i does not have a component along $\varphi_\triangle$. It follows that

$$f_i \in \text{span}\left\{ \psi_\gamma \mid \gamma \in \bigcup_{k=0}^{i-1} G(C^k(\alpha)) \right\}. \tag{4.32}$$

We can always choose i so that $\triangle$ is the root node of $\mathcal{H}$. This implies that $\tau_\triangle$ lies in the span of Ψ because $\varphi_{0,0} \in \Psi$. Since f_i and $\tau_\triangle$ are in span(Ψ) and the vector space L_2 is closed under addition, τ_δ has to be in the span of Ψ (by simply writing τ_δ as sum of f_i and $\frac{\alpha_\delta}{\alpha_\triangle}\tau_\triangle$ from Eq. 4.31). □

Definition 13. Let a sequence $\mathcal{X}$ of random variables $X_1, X_2, X_3, \ldots$ be a discrete-time stochastic process (DTSP). A DTSP $\mathcal{Y}$ is a *martingale* with respect to another DTSP $\mathcal{X}$ if

$$E(Y_{n+1} \mid X_1, \ldots, X_n) = Y_n, \quad \forall n,$$

that is the conditional expected value of the next event Y_{n+1} given all the past observations $(X_1, \ldots, X_n)$ is equal to the last event Y_n.

Definition 14. A *martingale difference sequence* is a martingale satisfying

$$E(Y_{n+1} \mid X_1, \ldots, X_n) = 0, \quad \forall n.$$

For the proof of (C2) we also employ Burkholder's inequality.

Theorem 7. *If $\{f_i\}_{i=1}^n$ is a simple martingale with respect to a non-decreasing sequence $\{\Sigma_i\}_{i=1}^n$ of sub-σ-fields of Σ, then its corresponding martingale difference sequence $\{d_i\}_{i=1}^n$ satisfies*

$$\left\| \sum_{i=1}^{n} \epsilon_i \; c_i \; d_i \right\|_p \leq (p^* - 1) \left\| \sum_{i=1}^{n} c_i \; d_i \right\|_p, \tag{4.33}$$

for all $n \in \mathbb{N}$ and all choices of $c_i \in \mathbb{R}$ and $\epsilon = \pm 1$.

See [8, 9, 10] for proofs. The form of Burkholder inequality is essentially identical to those of Eq. 4.25. (C2) can therefore be shown by verifying that Ψ is a martingale difference sequence. The unconditional basis constant is then $(p^* - 1)$, with $p^* = 2$ for L_2.

Let the conditional expected value of a piecewise constant function f be

$$E(f \mid \Sigma) = \sum_{i=1}^{n} \frac{\int_{E_i} f d\mu}{\mu(\tau_{E_i})} \; \tau_{E_i}, \tag{4.34}$$

where $\tau_0 \in \Sigma$ and $\text{supp}(f) \subset \text{supp}(\tau_0)$. The sub-$\sigma$-field Σ_0 of Σ is generated by a partition $\pi = \{E_1, E_2, \ldots E_n\}$ of τ_0. For the proof we employ the convention $0/0 = 0$.

Lemma 4. *Fix a finite subset $\{\gamma_i\}_{i=1}^n$ from $\mathcal{I}$ that satisfies $\gamma_1 < \gamma_2 < \ldots < \gamma_n$. Let $\tau_0 \in \Sigma^+$ be such that $\text{supp}\,(\psi_{\gamma_i}) \subset \tau_0$ for all i. Consider the partition*

$$\pi_i = \left\{ \tau_1^i, \tau_2^i, \tau_3^i, \tau_4^i, \tau_0 \setminus \left(\tau_1^i \cup \tau_2^i \cup \tau_3^i \cup \tau_4^i \right) \right\}, \tag{4.35}$$

of τ_0*, where the* $\tau_l^i \in \Sigma^+$ *are the partitions over which* ψ_{γ_i} *is defined. Let* $\Sigma_i = \sigma(\{\pi_j \mid 1 \leq j \leq i\})$*. Then*

1. ψ_{γ_i} *is* Σ_i*-measurable for* $i = 1, \ldots, n$*,*
2. $E(\psi_{\gamma_{i+1}} | \Sigma_i) = 0$ *for* $i = 1, \ldots, n-1$*.*

Proof. The first property holds because ψ_{γ_i} is defined over the first four atoms of the subset π_i of Σ_i. Because $i = 1, \ldots, n-1$, the atoms ς of Σ_i

- are disjoint from the support of $\psi_{\gamma_{i+1}}$, if $g(\varsigma) = g(\psi_{\gamma_{i+1}})$ and $p(\varsigma) \neq p(\psi_{\gamma_{i+1}})$,
- contains the support of $\psi_{\gamma_{i+1}}$, if $g(\varsigma) < g(\psi_{\gamma_{i+1}})$,
- are identical to the atoms over which $\psi_{\gamma_{i+1}}$ is defined, if $p(\varsigma) = p(\psi_{\gamma_{i+1}})$.

From the vanishing integral of $\psi_{\gamma_{i+1}}$ it then follows that the second property holds. □

We can now show that Ψ is an unconditional basis of L_2.

Theorem 8. *The wavelets* Ψ *form a unconditional basis for* L_2 *with basis constant* 1*.*

Proof. With Lemma 3 it is sufficient to show that Burkholder's inequality holds for Ψ.

Consider the sequence $\{f_i\}_{i=1}^n$ given by

$$f_i = \sum_{j=1}^{i} \psi_{\gamma_j}, \tag{4.36}$$

where γ_i and Σ_i are defined as in Lemma 4. Σ_i contains all π_j corresponding to the ψ_j which form f_i. From property 1 of Lemma 4 it then follows that f_i is Σ_i-measurable, and therefore $f_i = E(f_i, \Sigma_i)$.

The linearity of the conditional expectation operator and property 2 of Lemma 4 yield

$$E(f_{i+1} \mid \Sigma_i) - E(f_i \mid \Sigma_i) = E(f_{i+1} - f_i \mid \Sigma_i) = E(\psi_{\gamma_{i+1}}, \Sigma_i) = 0,$$

and thus $E(f_{i+1} \mid \Sigma_i) = f_i$. Therefore $\{f_i\}_{i=1}^n$ is a martingale with the martingale difference sequence Ψ. □

Chapter 5

Basis Transformation Matrices for Rotation

Many applications require the alignment of data sets. Image processing is one well known example (Figure 5.1), but also product integral calculations in physics and computer graphics, and processing and analysis of spherical data sets in medical imaging rely on a common alignment of signals. For applications where basis representations are employed alignment corresponds to representing all functions in the *same* basis, requiring a change of basis for those signals that are represented in a basis other than the *target basis* used for the computations. The projection of a signal into a target basis can be accomplished by multiplying its representation in the original *source basis* with a *basis transformation matrix*. The elements a_{ij} of these matrices project the information represented by the j^{th} basis function in the source basis onto the i^{th} basis function in the target basis. The size of matrices is hence $N \times M$, where M and N are the numbers of basis functions in the source and target basis, respectively. Despite their significant size, basis transformation matrices are nonetheless practical due to the *highly* sparse nature of both the matrices and basis function coefficient vectors for typical signals.

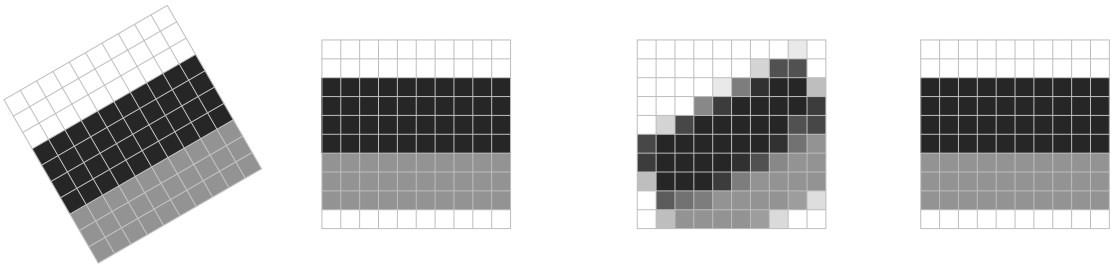

(a) (b)

Figure 5.1: Comparing the signals in (a) is not possible due to the different alignment of the partitions. After resampling a comparison of the signals in (b) is possible. Clearly visible are the resampling artifacts which occur for domains of finite extent.

In computer graphics, a well-known application involving the alignment of data sets is the solution of the *rendering equation* [40]:

$$B(x,\omega_0) = \int_{\Omega_n} L(x,\omega)V(x,\omega)\rho(x,\omega_0,\omega)\,(\omega \circ n(x))\,d\omega, \tag{5.1}$$

where x is a surface point in a scene, $B(x,\omega_0)$ is the reflected light at x into direction ω_0, $L(x,\omega)$ is the incident radiance at x from direction ω, $V(x,\omega)$ is the binary visibility term which determines if light coming from direction ω is blocked by objects in the scene, $\rho(x,\omega_0,\omega)$ is the BRDF of the surface in the local coordinate system at x, and $n(x)$ is the surface normal. The integral is computed over all possible directions ω of incident radiance in the upper hemisphere Ω_n of the local surface coordinate system at x. For efficiency, in most cases the factors of the product integral are represented in a suitable basis such as spherical Harmonics or wavelets.

To compute the appearance of a virtual scene, the rendering equation has to be solved at all visible surface points. Storing a basis representation of the BRDF for all possible orientations of the local surface coordinate system is however impractical. A feasible alternative is to store *one* representation of the BRDF and employ rotation in the basis to align the function to local surface coordinate systems. For wavelet bases the alignment amounts to rotating the partition over which the basis is defined (Figure 5.2). The

(a) (b) (c)

Figure 5.2: Rotation of a signal. The original signal is shown on the left hand side. A rotated version of the signal is obtained by rotating the partition over which the basis is defined (middle). Performing the basis transformation yields the rotated signal in the target basis (right). Note that the partition of the target basis has the same alignment of the partition of the original, unrotated basis.

rotated basis then depends on the orientation of the local surface coordinate system and is no longer aligned with the basis representations of the other factors of the rendering equation, making an efficient solution of the product integral impossible. Considering the rotated basis as source basis, we can employ a basis transformation matrix to project the rotated BRDF into the basis of the remaining factors of the product integral. After projection, the light transport factors are again aligned, allowing an efficient solution of the rendering equation.

What is commonly referred to as *rotation in a wavelet basis representation* is therefore not only the rotation of a signal but also the projection from the rotated source basis into a target basis which is better suited for processing. In many cases, such as the previous example, the original basis of the unrotated signal and the target basis are identical (Figure 5.2). Important for the practicality of rotations in a wavelet basis representation is that it is *not* necessary to explicitly obtain the representation of a signal in the rotated source basis. With the results from Chapter 3.4 it follows that the basis representations

of the unrotated signal in the original basis and those of the rotated signal in the source basis are identical.

In the following, we will first develop basis transformation matrices for general Riesz bases. The result will then be employed to derive the rotation matrices for spherical Haar wavelet bases. To compare the rotation in spherically and planar parametrized representations, we also derive the rotation matrices for the Haar cubemap basis. In contrast to the work by Wang et al., we chose the Haar cubemap basis as planar representation because it is more common for applications [57, 101, 88] and the distortion of mapping the sphere onto a planar domain is for the cubemap less severe than for the octahedral map [67].

5.1 Basis Transformation Matrices for Riesz Bases

Let $\{f_{i_1}\}_{i_1 \in \mathcal{I}_1}$ and $\{g_{i_2}\}_{i_2 \in \mathcal{I}_2}$ be two normalized Riesz bases acting as source and target bases, respectively, and let $\left\{\tilde{f}_{i_1}\right\}_{i_1 \in \mathcal{I}_1}$ and $\{\tilde{g}_{i_2}\}_{i_2 \in \mathcal{I}_2}$ be the corresponding dual bases as defined in Theorem 1.

The representation of a signal S in the source basis is $\sum_{i_1 \in \mathcal{I}_1} c_{i_1} f_{i_1}$. The target basis representation of S can then be obtained by the projection:

$$\begin{aligned} S &= \sum_{i_2 \in \mathcal{I}_2} \left\langle \left(\sum_{i_1 \in \mathcal{I}_1} c_{i_1} f_{i_1} \right), \tilde{g}_{i_2} \right\rangle g_{i_2} \\ &= \sum_{i_2 \in \mathcal{I}_2} \sum_{i_1 \in \mathcal{I}_1} c_{i_1} \left\langle f_{i_1}, \tilde{g}_{i_2} \right\rangle g_{i_2} \\ &= \sum_{i_2 \in \mathcal{I}_2} \sum_{i_1 \in \mathcal{I}_1} c_{i_1} \ \beta_{i_1,i_2} \ g_{i_2}. \end{aligned}$$

The *coupling coefficients* β_{i_1,i_2} forming the basis transformation matrices Υ are defined as

$$\beta_{i_1,i_2} = \left\langle f_{i_1} \, , \, \tilde{g}_{i_2} \right\rangle . \tag{5.2}$$

We emphasize that the derivation in this section holds for arbitrary Riesz bases $\{f_{i_1}\}_{i_1 \in \mathcal{I}_1}$ and $\{g_{i_2}\}_{i_2 \in \mathcal{I}_2}$; rotation, where the bases differ in their alignment, is only one possible application.

5.2 Rotation Matrices for Spherical Haar Wavelets

5.2.1 Derivation of Coupling Coefficients

Let Ψ_1 and Ψ_2 be two spherical Haar wavelet bases acting as source and target basis, respectively, and let $\mathcal{P}_1 = \{T_{j_1,k_1} \mid j_1 \in \mathcal{J}_1, k_1 \in \mathcal{K}_1(j_1)\}$ and $\mathcal{P}_2 = \{T_{j_2,k_2} \mid j_2 \in \mathcal{J}_2, k_2 \in \mathcal{K}_2(j_2)\}$ be the partitions over which the bases are defined. Furthermore, let the source basis be a rotated version of the target basis so that Ψ_1 has then been obtained by rotating the partition over which Ψ_2 is defined, that is

$$T_{j_1,k_1} = R\,T_{j_2,k_2} \quad \text{for all} \quad j_1 = j_2, k_1 = k_2, \tag{5.3}$$

where $R \in SO(3)$ is a unitary rotation around the origin. The partition of a spherical Haar wavelet basis is defined over the sphere. The rotation therefore only alters the position of the domains T_{j_2,k_2} on the sphere but does not affect their shape. The definition of the basis functions over the partitions implies then that the source and target bases differ only in the position of the basis functions on the sphere, allowing a straightforward, analytic computation of the coupling coefficients (cf. [95]).

Let $\hat{\psi}_{i_1} = \hat{\psi}_{j_1,m_1} \in \Psi_1$, with $i_1 \in \mathcal{I}_1 \setminus 0$, and $\breve{\psi}_{i_2} = \breve{\psi}_{j_2,m_2} \in \Psi_2$, with $i_2 \in \mathcal{I}_2 \setminus 0$, be a primary and a dual wavelet basis function in the source and target basis, respectively.

With Eq. 5.2, the coupling coefficient between the two basis functions is

$$\begin{aligned}
\beta_{i_1,i_2} &= \int_{\mathbb{S}^2} \hat{\psi}_{j_1,m_1} \breve{\psi}_{j_2,m_2} \, d\omega \\
&= \int_{\mathbb{S}^2} \sum_{l_1} \; g_{j_1,m_1,l_1} \; \varphi_{j_1+1,l_1} \sum_{l_2} \; \tilde{g}_{j_2,m_2,l_2} \; \tilde{\varphi}_{j_2+1,l_2} d\omega \\
&= \sum_{l_1} \sum_{l_2} \; g_{j_1,m_1,l_1} \; \tilde{g}_{j_2,m_2,l_2} \int_{\mathbb{S}^2} \eta_{j_1+1,l_1} \; \tau_{j_1+1,l_1} \; \tilde{\eta}_{j_2+1,l_2} \; \tilde{\tau}_{j_2+1,l_2} d\omega \\
&= \sum_{l_1} \sum_{l_2} \; \eta_{j_1+1,l_1} \; g_{j_1,m_1,l_1} \; \tilde{\eta}_{j_2+1,l_2} \; \tilde{g}_{j_2,m_2,l_2} \int_{\mathbb{S}^2} \tau_{j_1+1,l_1} \; \tilde{\tau}_{j_2+1,l_2} \; d\omega \\
&= \sum_{l_1} \sum_{l_2} \eta_{j_1+1,l_1} \; \tilde{\eta}_{j_2+1,l_2} \; g_{j_1,m_1,l_1} \; \tilde{g}_{j_2,m_2,l_2} \; \alpha_{l_1,l_2}, \qquad (5.4)
\end{aligned}$$

where α_{l_1,l_2} denotes the area over which τ_{j_1+1,l_1} and $\tilde{\tau}_{j_2+1,l_2}$ overlap, and $\eta_{j,l}$ and $\tilde{\eta}_{j,l}$ are the normalization constants of the primary and dual scaling basis functions, respectively. The derivations for the other three configurations of scaling and wavelet basis functions are analogous yielding

$$\begin{aligned}
\beta_{0,i_2} &= \eta_0 \sum_{l_2} \tilde{\eta}_{j_2+1,l_2} \; \tilde{g}_{j_2,m_2,l_2} \; \alpha_{0,l_2} \\
\beta_{i_1,0} &= \tilde{\eta}_0 \sum_{l_1} \eta_{j_1+1,l_1} \; g_{j_1,m_1,l_1} \; \alpha_{l_1,0} \\
\beta_{0,0} &= \eta_0 \, \tilde{\eta}_0 \, \alpha_{0,0},
\end{aligned}$$

where the index 0 denotes the scaling basis functions, and $i_1 \in \mathcal{I}_1 \setminus 0$ and $i_2 \in \mathcal{I}_2 \setminus 0$ are defined exclusively over the wavelet basis functions.

Although the rotation matrices can be computed analytically, in practice the rotated signals suffer from resampling artifacts similar to those in Figure 5.1. These result from the finite extent and unaligned nature of the partitions over which source and target bases are defined.

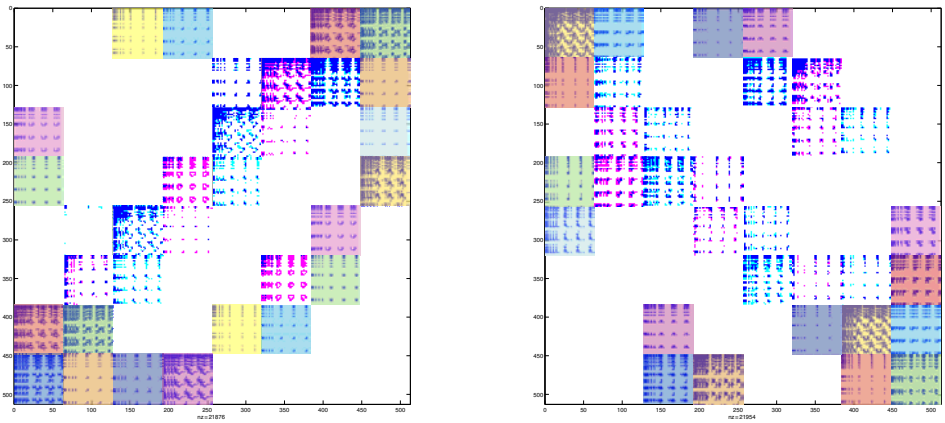

Figure 5.3: Quasi block symmetric structure of the basis transformation matrices for spherical Haar wavelet bases defined over a partition derived from an octahedron. Identical blocks are shown in the same color.

5.2.2 Quasi Block Symmetry

For spherical Haar wavelet bases defined over sphere-symmetric partitions derived from an octahedron or an icosahedron the rotation matrices exhibit the block structure depicted in Figure 5.3. Every block can be observed twice in such a matrix but, in contrast to block symmetric matrices, the positions of the blocks are not symmetric to the main diagonal of the matrix. We denote this structure as *quasi block symmetric*.

In the following, after introducing the necessary notation, we will formally establish that the rotation matrices for spherical Haar wavelet bases have a quasi block symmetric structure. The proof also provides some insights of why the matrices are symmetric.

Let Ψ_1 and Ψ_2 be two SOHO wavelet bases as defined in the derivation in Chapter 5.2.1, and let T_{0,k_2} be the projection of an octahedron or an icosahedron onto the sphere. The basis functions defined over one partition tree are thereby labeled consecutive and the total ordering results from a linear ordering of the trees. We furthermore require that $\mathcal{P}_2$ is symmetric on the sphere so that for every T_{j_2,k_2} exactly one $T_{j_2,k_2'}$ exists with

$v_{j_2,k_2,l} = -v_{j_2,k_2',l}$, for $l = 1, 2, 3$, where the $v_{j_2,k_2,l}$ are the vertices of a spherical triangle that defines a partition. In the following we will denote the symmetric equivalent of an entity with a "bar", the domain symmetric to T_{j_2,k_2} is thus $\bar{T}_{j_2,k_2}$. We can now state the following theorem:

Theorem 9. *Let Ψ_1 and Ψ_2 be a source and a target basis as defined above. The basis transformation matrix Υ projecting Ψ_1 into Ψ_2 is then* quasi block symmetric *in the sense that*

- *the matrix has a block structure,*
- *two nonzero blocks in the matrix are identical.*

Proof. (Sketch) With $R \in SO(3)$ being the unitary rotation which yields the source basis, it follows from the definition of the target basis Ψ_2 on the sphere that applying R to $\mathcal{P}_2$ does not alter the structure of the partition or the shape of the T_{j_2,k_2}, implying that the source basis exhibits the same symmetry on $\mathbb{S}^2$ as the target basis.

Let ψ_{j_1,m_1} and $\bar{\psi}_{j_1,m_1}$ be the same wavelet basis function of the source basis defined over T_{j_1,k_1} and $\bar{T}_{j_1,k_1}$, respectively, and let ψ_{j_2,m_2} and $\bar{\psi}_{j_2,m_2}$ defined over T_{j_2,k_2} and $\bar{T}_{j_2,k_2}$, respectively, be an analogous pair of the target basis. With Eq. 5.4, the coupling coefficient β_{i_1,i_2} between the wavelet basis functions $\psi_{j_1,m_1} = \psi_{i_1}$ and $\psi_{j_2,m_2} = \psi_{i_2}$ is

$$\beta_{i_1,i_2} = \sum_{l_1} \sum_{l_2} \eta_{j_1+1,m_1,l_1}\, \eta_{j_2+1,m_2,l_2}\; g_{j_1,m_1,l_1}\, g_{j_2,m_2,l_2}\; \alpha_{l_1,l_2}, \tag{5.5}$$

where

$$\alpha_{l_1,l_2} = \int_{\mathbb{S}^2} \tau_{j_1+1,l_1}\, \tau_{j_2+1,l_2}\, d\omega. \tag{5.6}$$

For the quasi symmetry to hold, we have to show that β_{i_1,i_2} and $\bar{\beta}_{i_1,i_2}$ are identical, where $\bar{\beta}_{i_1,i_2}$ is the coupling coefficient between $\bar{\psi}_{j_1,m_1}$ and $\bar{\psi}_{j_2,m_2}$.

It follows from the definition of the SOHO wavelet basis that the filter coefficients $g_{j,m,l}$ and the normalization factors $\eta_{j+1,l}$ in Eq. 5.5 only depend on the areas of the domains over which the wavelet basis functions are defined but not on their position on the

sphere. Due to the symmetry of $\mathcal{P}_1$, the domains T_{j_1,m_1} and $\bar{T}_{j_1,m_1}$, and their children have the same shape and scale and therefore also the same area. The filter coefficients and normalization factors associated with ψ_{j_1,m_1} and $\bar{\psi}_{j_1,m_1}$ in Eq. 5.5 are thus identical. The symmetry of $\mathcal{P}_2$ implies that the same is true for ψ_{j_2,m_2} and $\bar{\psi}_{j_2,m_2}$. It is easy to see that the overlaps α_{l_1,l_2} and $\bar{\alpha}_{l_1,l_2}$ between domains τ_{j_1+1,l_1} and τ_{j_2+1,l_2}, and the symmetric equivalents $\bar{\tau}_{j_1+1,l_1}$ and $\bar{\tau}_{j_2+1,l_2}$ are identical for every possible combination of l_1 and l_2.

Given that the filter coefficients and the normalization factors associated with a wavelet basis function and its symmetric equivalent are identical, and that $\alpha_{l_1,l_2} = \bar{\alpha}_{l_1,l_2}$, for all possible combinations of l_1 and l_2, it follows immediately from Eq. 5.5 that $\beta_{i_1,i_2} = \bar{\beta}_{i_1,i_2}$. Analogous derivations show that the identity also holds for coupling coefficients resulting from the remaining configurations of scaling and wavelet basis functions.

The block structure of the rotation matrices results from the definition of the partitions as forests of trees. Each block in a matrix relates the basis functions defined over one partition tree of the source basis to the basis functions defined over one partition tree of the target basis. That the symmetry of individual coupling coefficients β_{i_1,i_2} and $\bar{\beta}_{i_1,i_2}$ carries over to blocks follows from the consistent labeling of the partitions across trees.

The proofs for the quasi block symmetric structure of rotation matrices for other spherical Haar wavelet bases are analogous (then again considering primary and dual basis functions). □

Until now we only *assumed* that the partition $\mathcal{P}_2$ of the target basis is symmetric on $\mathbb{S}^2$. It is easy to see that this is always true for the geodesic bisector subdivision employed by Schröder and Sweldens [76]. For the novel subdivision scheme proposed in Chapter 4.4, the symmetry has to be guaranteed by the construction of the partition. We employ rotation and reflection of one initial partition tree to enforce symmetry.

The quasi block symmetric structure of the rotation matrices is not only of theoretical interest but also important for applications. Basis transformation matrices for wavelet

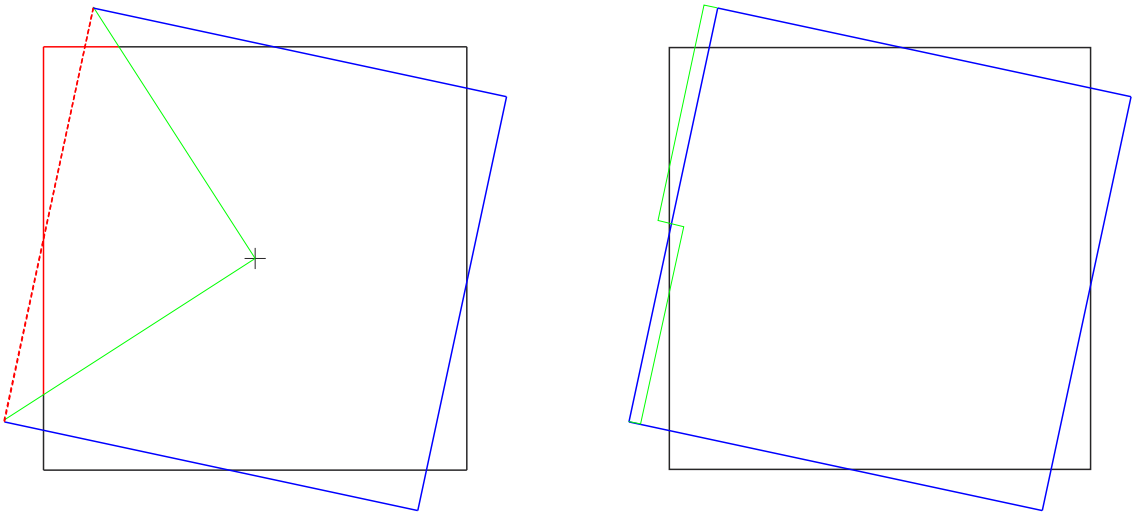

Figure 5.4: Top view of rotated (blue) and unrotated (black) Haar cubemap basis. On the right hand side the projection of a partition of the rotated basis (red, dashed) onto the target basis is shown, a wavelet basis function on level 0 is indicated in green.

bases are usually large [95] and the symmetric structure enables to significantly reduce their storage costs.

5.3 Rotation Matrices for the Haar Cubemap Basis

5.3.1 Derivation of Coupling Coefficients

Computing the coupling coefficients for the Haar cubemap basis is more complex than for spherical Haar wavelets. Let Ψ_1 and Ψ_2 be the source and the target Haar cubemap basis, respectively, and let Ψ_1 be a rotated version of Ψ_2. Except for canonical rotations by multiples of $\pi/2$ around the principal axes, the domains of the basis functions of Ψ_1 and Ψ_2 are not aligned; an example is shown in Figure 5.4. A direct computation of the coupling coefficients is therefore not possible. Different approaches can be employed

to align the domains of the bases. We decided to project the partition of Ψ_1 onto the domain of Ψ_2 yielding a projected source basis $\breve{\Psi}_1$; an example of the projection of a partition on level 0 is shown in the left image in Figure 5.4. The coupling coefficients can then be computed as proposed by Wang et al. [95]: A basis function $\breve{\psi}_{i_1}$ of $\breve{\Psi}_1$ is first resampled onto the domains on the finest level of the partition $\mathcal{P}_2$ of Ψ_2, yielding a resampled version $\bar{\psi}_{i_1}$ of $\breve{\psi}_{i_1}$ in the target basis. The coupling coefficients between $\breve{\psi}_{i_1}$ and all basis functions of the target basis are then obtained by performing a wavelet transform of the signal given by $\bar{\psi}_{i_1}$.

An alternative approach to aligning the domains of the basis functions is to project the partitions of both Ψ_1 and Ψ_2 onto the sphere. The coupling coefficients can then be computed on $\mathbb{S}^2$. This approach might lead to less distortion but we have not yet investigated the idea in more detail.

Note that the projection which is necessary to align the domains of the source and target basis functions can magnify the distortion resulting from a planar parametrization of the sphere. An example is given in Figure 5.5. The magnification is thereby not limited to the Haarcube map basis but can occur for any approach which uses wavelets defined over a planar domain to represent spherical signals.

5.3.2 Pseudo block symmetry

The rotation matrices for the Haar cubemap basis exhibit a similar structure as the matrices for spherical Haar wavelets. However, the structure differs in that some coupling coefficients in the matrices are exchanged and for some the sign is flipped. We therefore denote it as *pseudo block symmetric* structure. The violations from quasi block symmetry exhibit a regular pattern which is independent of the rotation of the source basis making it possible to compress the rotation matrices for the Haar cubemap basis in a similar way as the matrices for spherical Haar wavelets.

The block structure in the matrices arises again from the construction of the partitions as forests of trees. For the Haar cubemap basis each partition tree is defined over one face of the cubemap.

5.4 General Basis Transformation Matrices

We remark that basis transformations as discussed in this chapter are a general concept and rotation is only one particular application. Other interesting operations are for example scaling and resampling, or convolution of signals. In the past such operations have been computed in the native domain of a signal. The ability to perform the computation in the basis representation is becoming increasingly important as the size of many data sets is reaching several gigabytes and beyond [98, 33, 95]; for example digital imagery with several gigapixel resolution became recently available [1]. Manipulating these data sets in their native representation is impossible for most of today's hardware, and the trend in the last years showed that the size of data sets is increasing much more rapidly than available computing power and memory bandwidth. Furthermore, manipulating data sets in a wavelet domain is attractive as many modern data compression schemes are based on wavelet basis representation [20, 50, 95].

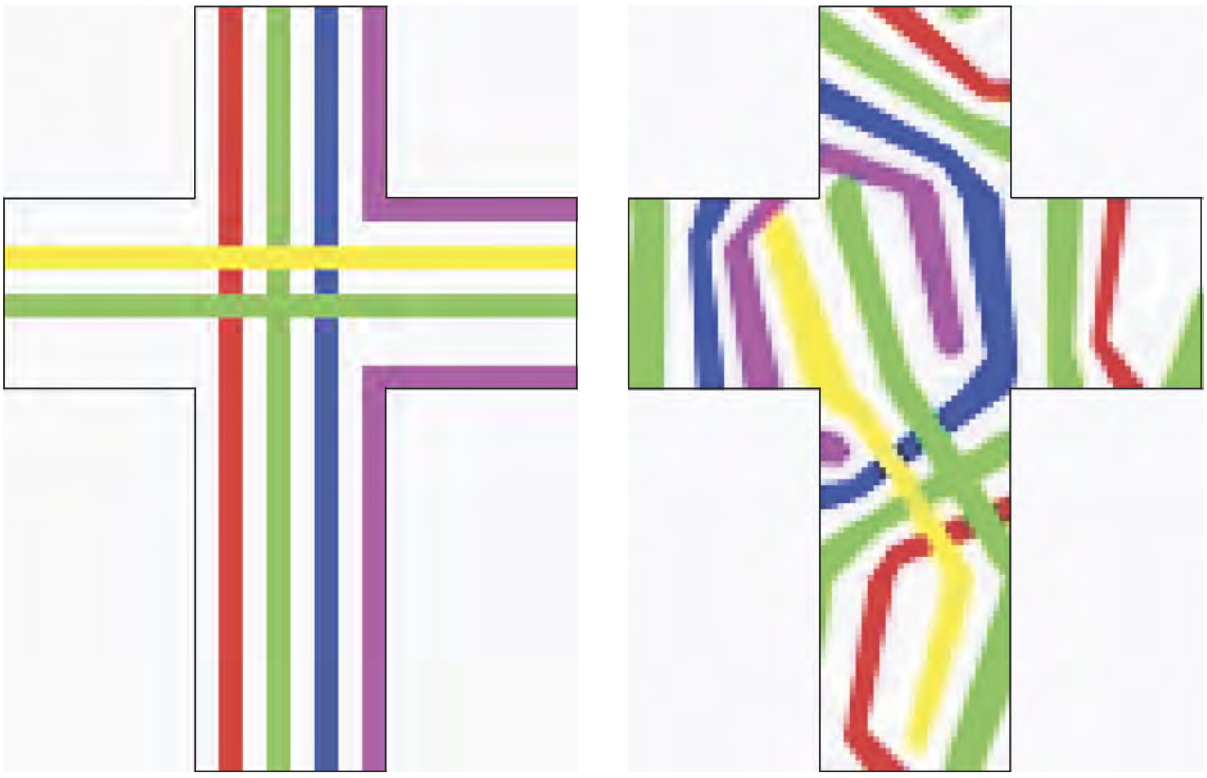

Figure 5.5: Distortion introduced by the rotation for a signal represented in the Haar cubemap basis.

Chapter 6

Experiments

6.1 Introduction

In contrast to other spherical Haar wavelet bases proposed in the literature, the SOHO wavelet basis is both fully orthogonal and symmetric. The superior theoretical properties of the basis do however not necessarily lead to a better performance in practice. We therefore performed a variety of experiments to evaluate the practical relevance of orthogonality and symmetry. To provide results which are useful in a variety of fields, we limited ourselves to general experiments that provide insights for a wide range of applications. The bases that have been employed for comparison are representations which are alternatives to the SOHO wavelet basis in practical settings.

The results presented in this chapter are limited in that we were neither able to explore the whole space of possible parameters, nor could we compare the SOHO wavelet basis to all representations for spherical signals proposed in the literature. It should however be noted that some experiments have been omitted because the results have already been presented in other works. Refer for example to the works by Ng et al. [56] or Okabe et al. [60] for a comparison of Spherical Harmonics and Haar-like bases, or to the work by

Schröder and Sweldens [76] for experiments with smooth discrete wavelets on the sphere.

After a discussion of the methodology (Section 6.2) and the implementation (Section 6.3) which have been used for the experiments, we will first analyze some properties of the SOHO wavelets (Section 6.4), before the approximation performance of the basis is evaluated (Section 6.5), and the efficiency of the rotation matrices developed in Section 5 is assessed (Section 6.6). We conclude the chapter with a discussion of the presented results (Section 6.7).

6.2 Methodology

6.2.1 Bases

To assess the efficacy of the SOHO wavelet basis for the approximation of spherical signals, we compared it to six previously prosposed spherical Haar wavelet bases: the Bio-Haar basis developed by Schröder and Sweldens [76], the pseudo Haar wavelets employed by Ma et al. [47], and the nearly orthogonal bases proposed by Nielson et al. [58] and by Bonneau [7]. We used the Bio-Haar basis because it is the most popular spherical Haar wavelet basis and has been employed in a variety of applications [96, 64, 53]. The pseudo Haar basis was interesting to us for its simplicity — the filter coefficients are in fact identical to those of the non-standard Haar wavelets in $2D$ [87] — although this comes at the price that the pseudo Haar basis is not a basis of the space $L_2(\mathbb{S}^2, d\omega)$. See Appendix A for a proof. Nearly orthogonal bases have in the limit case the same desirable properties as the SOHO wavelets. We were thus interested to see if the limit properties are also of practical relevance.

To evaluate the efficacy of the rotation of signals represented in the SOHO wavelet basis, we compared its performance to three previously proposed representations for spherical signals. Next to the Bio-Haar basis and the pseudo Haar wavelets we also employed the Haar cubemap basis for these experiments. Note that a direct comparison of the SOHO

wavelet basis and the Haar cubemap basis is difficult; the bases are defined over different numbers of partition trees yielding different signal resolutions for fixed tree levels. In Section 6.6.2 therefore only relative error measures are provided.

6.2.2 Signals

Three signals have been employed for the experiments:

- A "real world" signal which has features in the full frequency spectrum.
- A piecewise constant signal only containing jump discontinuities.
- A (very) smooth, unimodal signal.

The signals are shown in Figure 6.1. For convenience we will use nomenclature from computer graphics and refer to the them as "texture map", "visibility map", and "BRDF", respectively. We used 8-bit, low dynamic range versions of the signals for the experiments. Given the longitude-latitude maps shown in Figure 6.1, spherical signals defined over the domains of a partition at a fixed level n have been obtained with Monte-Carlo sampling.

6.2.3 Error Norms

For the experiments we employed the ℓ_1 and the ℓ_2 norm as error measures. The ℓ_2 norm is the standard measure for the space $L_2(\mathbb{S}^2, d\omega)$ and has been used in a variety of applications. In the literature, it has been argued that for images the ℓ_1 error norm better corresponds to the perceived image quality than for the example the error in the ℓ_2 norm [21]. The test signals shown in Figure 6.1 can be seen as images on the sphere and we therefore also employed the ℓ_1 norm in our experiments.

Numerical error measures such as the ℓ_1 and the ℓ_2 norm are valuable in many contexts.

They are however often inadequate to measure the quality of a signal as it is perceived by humans [66]. We therefore also provide reconstructions of approximated and rotated signals which permit a visual, though subjective, evaluation of the quality.

6.2.4 Approximation of Signals

The approximation of a signal is a common objective in many applications where basis representations are used. In most cases the approximation is subject to the constraint that it should minimize the error in an ℓ_p norm, for $0 < p < \infty$, for a given number of basis function coefficients k. Efficiently finding the optimal set of basis function coefficients, that is the set which minimizes the error in the ℓ_p norm under consideration, is however in general not possible (cf. [36]).

Let

$$S = \sum_{i \in \mathcal{I}} \gamma_i \, \hat{\psi}_i$$

be the wavelet basis representation of a signal S, and let $\bar{\mathcal{I}} \subset \mathcal{I}$ be an index set with $\#\bar{\mathcal{I}} < \#\mathcal{I}$ elements. An approximation $\bar{S}$ of S is then given by

$$\bar{S} = \sum_{i \in \bar{\mathcal{I}}} \gamma_i \, \hat{\psi}_i.$$

The set of elements which has been excluded from $\mathcal{I}$ to form $\bar{\mathcal{I}}$ will be denoted as $\Pi = \mathcal{I} \backslash \bar{\mathcal{I}}$. With Eq. 3.1, the approximation error in an ℓ_p norm, for fixed but arbitrary $0 < p < \infty$, is (cf. [86])

$$\begin{aligned} E \equiv \|S - \bar{S}\|_p &= \left(\int_X \left| S - \bar{S} \right|^p dx \right)^{\frac{1}{p}} \\ &= \left(\int_X \left| \sum_{i \in \Pi} \gamma_i \, \hat{\psi}_i \right|^p dx \right)^{\frac{1}{p}}. \end{aligned} \tag{6.1}$$

With the refinement relationship for the wavelet basis functions and $\psi_i = \psi_{j,m}$ this yields

$$E = \left(\int_X \left| \sum_{i \in \Pi} \gamma_i \sum_l g_{i,l} \, \varphi^i_{j+1,l} \right|^p dx \right)^{\frac{1}{p}}.$$

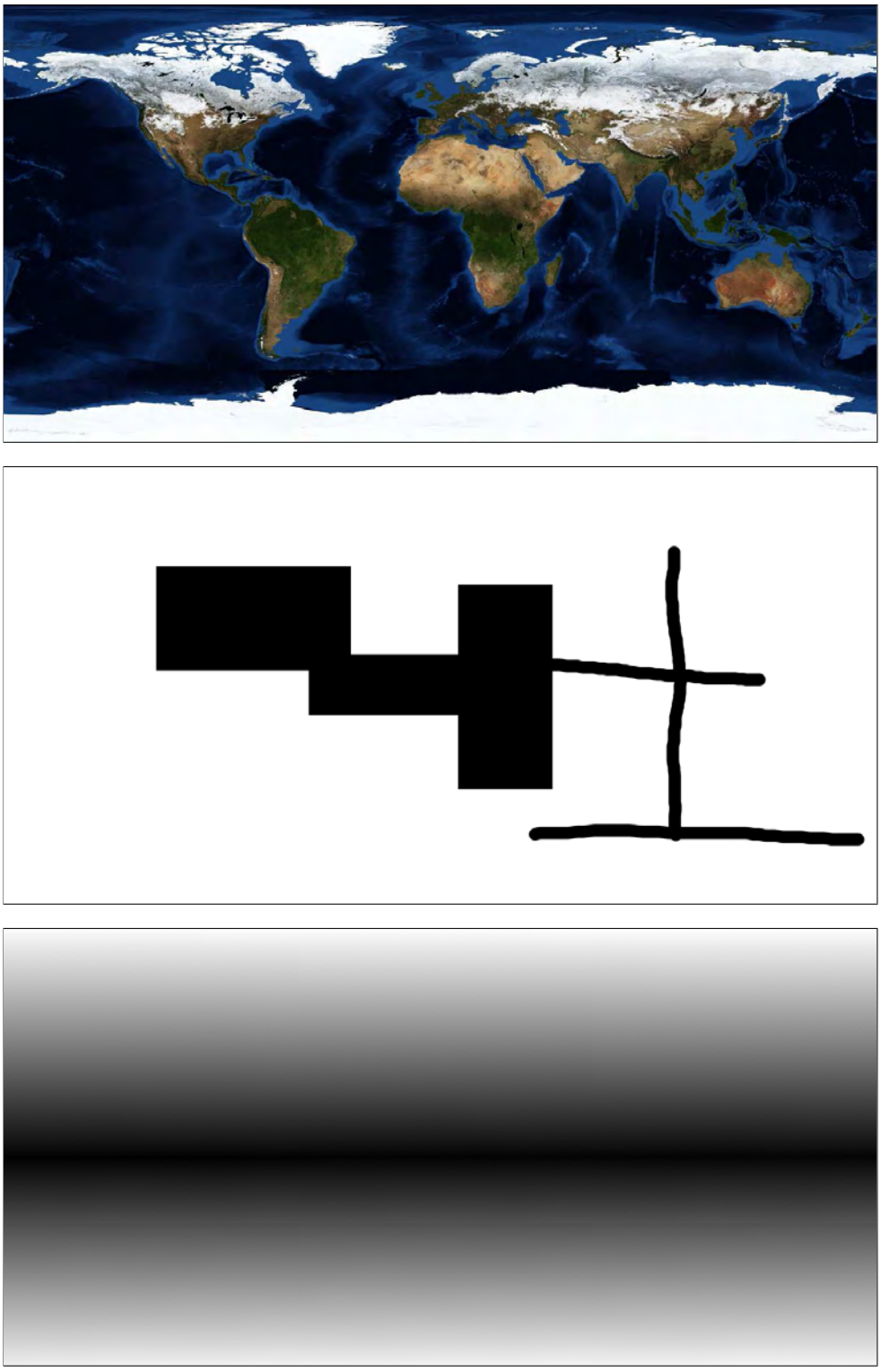

Figure 6.1: Signals (as longitude-latitude maps) employed for the experiments.

In the following, we will split the domain X and integrate over the partitions $S_{n,k}$ separately. The level n corresponds to the partitions over which the wavelet basis functions at the finest level are defined. The normalization constant of the l^{th} scaling basis function over which the i^{th} basis function $\hat{\psi}_i$ is defined will be denoted with $\eta^i_{j+1,l}$, and it is assumed that γ_i is zero if the support of $\hat{\psi}_i$ is disjoint from $\chi_{n,k}$. For a Haar-like basis, we can then write

$$E = \left(\sum_{k \in \mathcal{K}(n)} \int_{S_{n,k}} \left| \sum_{i \in \Pi} \gamma_i \frac{g_{i,l}}{\eta^i_{j+1,l}} \chi_{n,k} \right|^p dx \right)^{\frac{1}{p}}.$$

The integrals over the $S_{n,k}$ are always positive so that

$$E = \left(\sum_{k \in \mathcal{K}(n)} \left| \sum_{i \in \Pi} \gamma_i \frac{g_{i,l}}{\eta^i_{j+1,l}} \right|^p \left(\int_{S_{n,k}} \chi_{n,k} \, dx \right)^p \right)^{\frac{1}{p}}.$$

Performing the integration yields

$$E = \left(\sum_{k \in \mathcal{K}} (n) \left| \sum_{i \in \Pi} \gamma_i \frac{g_{i,l}}{\eta^i_{j+1,l}} \right|^p \mu(S_{n,k})^p \right)^{\frac{1}{p}}. \tag{6.2}$$

From Eq. 6.2 it can be concluded that it is for Haar-like wavelet bases very difficult to efficiently obtain the optimal set of basis function coefficients which minimizes the error in an ℓ_p norm. In particular the absolute value of a sum of signed values in Eq. 6.2 makes it difficult to find the set Π which minimizes the error E. Since Haar-like wavelet bases are the simplest wavelets, the result generalizes to arbitrary wavelet bases.

Theorem 10. *For an orthonormal basis the optimal approximation in the ℓ_2 norm with k basis function coefficients can be obtained efficiently in $O(N \log N)$.*

Proof. Given Eq. 6.1, the squared error in the ℓ_2 norm is

$$\begin{aligned}\left(\|S - \bar{S}\|_2\right)^2 &= \int_X \left(\sum_{i\in\Pi} \gamma_i \ \hat{\psi}_i\right)^2 dx \\ &= \int_X \left(\sum_{i_1\in\Pi} \gamma_{i_1} \ \hat{\psi}_{i_1} \sum_{i_2\in\Pi} \gamma_{i_2} \ \hat{\psi}_{i_2}\right) dx \\ &= \int_X \sum_{i_1\in\Pi}\sum_{i_2\in\Pi} \gamma_{i_1}\gamma_{i_2} \ \hat{\psi}_{i_1}\hat{\psi}_{i_2} \ dx. \end{aligned} \tag{6.3}$$

It follows from Eq. 6.3 that for arbitrary wavelet bases the best approximation in the ℓ_2 norm cannot be computed efficiently (cf. Theorem 11). However, for an orthonormal basis where $\langle\hat{\psi}_{i_1}, \hat{\psi}_{i_2}\rangle = \delta_{i_1,i_2}$, Eq. 6.3 can be further simplified yielding

$$\begin{aligned}\left(\|S - \bar{S}\|_2\right)^2 &= \sum_{i\in\Pi} \gamma_i^2 \langle\hat{\psi}_i, \hat{\psi}_i\rangle \\ &= \sum_{i\in\Pi} \gamma_i^2. \end{aligned} \tag{6.4}$$

For an orthonormal basis the best approximation in the ℓ_2 norm can therefore be obtained by choosing $\bar{\mathcal{I}}$ so that it contains the k largest basis function coefficients from $\mathcal{I}$. □

Thus, finding the optimal approximation for an orthonormal basis in the ℓ_2 norm requires first performing a full wavelet transform of an input signal, and then sorting the resulting coefficients. With a worst case complexity of $O(N \log N)$ for the best sorting algorithms, this yields a log-linear complexity. In practice, for the reconstruction of a signal after approximation all but the k largest basis function coefficients are assumed to be zero. Note that this is similar to the effect of quantization where very small basis function coefficients become zero because of the limited precision of the representation. The main difference is that in the approach employed in our experiments the number of nonzero basis function coefficients is known a priori. In the remainder of the thesis we shall refer to this approximation strategy as *k-largest approximation*.

The Bio-Haar basis is semi-orthogonal. Using the k-largest approximation strategy is therefore not optimal in the ℓ_2 norm. It follows from the minimal support of the basis

functions that the optimal approximation can still be computed at moderate costs.

Theorem 11. *For the Bio-Haar basis employing the k largest coefficients c_{j,m_1} with*

$$c_{j,m_1} = \gamma_{j,m_1} \sum_{m_2} \gamma_{j,m_2} \sum_{l} g_{j,m_1,l}\ g_{j,m_2,l}\ \alpha_{j+1,l} \quad \textit{for} \quad \{m_2 \in \mathcal{M}(j) \mid p(T_{j,m_1}) = p(T_{j,m_2})\},$$

over all $j \in \mathcal{J}$ and $m_1 \in \mathcal{M}(j)$, minimizes the approximation error in the ℓ_2 norm for an approximation with k coefficients.

Proof. Given Eq. 6.3,

$$\left(\|S - \bar{S}\|_2\right)^2 = \sum_{i_1 \in \Pi} \sum_{i_2 \in \Pi} \gamma_{i_1}\, \gamma_{i_2} \left\langle \hat{\psi}_{i_1}\,,\, \hat{\psi}_{i_2} \right\rangle, \tag{6.5}$$

we observe that each basis function coefficient γ_{i_1} is present in more than one term of the double sum. For a basis where the basis functions have global support, γ_{i_1} appears in $\#\Pi$ summands. For a basis with locally supported basis functions the number of (nonzero) terms with γ_{i_1} is given by the number of inner products $\left\langle \hat{\psi}_{i_1}\,,\, \hat{\psi}_{i_2} \right\rangle$ which are nonzero. The vanishing integral of the wavelet basis functions for the Bio-Haar basis implies that the inner product is zero if $\hat{\psi}_{i_1}$ and $\hat{\psi}_{i_2}$ are defined on different levels (cf. Section 4.3) or if one of the basis functions is the scaling basis function on the coarsest level. It follows from the strictly nested nature of the partition that the inner product $\langle \psi_{j,m_1}\,,\, \psi_{j,m_2} \rangle$ of two wavelet basis functions on the same level vanishes if $p(T_{j,m_1}) \neq p(T_{j,m_2})$. For wavelet basis functions defined over the same partition, that is $p(T_{j,m_1}) = p(T_{j,m_2})$, the inner product is

$$\langle \psi_{j,m_1}\,,\, \psi_{j,m_2} \rangle = \sum_{l_1} \sum_{l_2} g_{j,m_1,l_1}\ g_{j,m_2,l_1} \int_{\mathbb{S}^2} \varphi_{j+1,l_1}\ \varphi_{j+1,l_2}\ d\omega. \tag{6.6}$$

For fixed j, the support of the $\varphi_{j,k}$ is disjoint. The integral in Eq. 6.6 is thus nonzero only if $l_1 = l_2$. With the definition of the primary scaling functions for the Bio-Haar basis it follows that

$$\langle \psi_{j,m_1}\,,\, \psi_{j,m_2} \rangle = \sum_{l} g_{j,m_1,l}\, g_{j,m_2,l}\, \alpha_{j+1,l}.$$

The full contribution c_{j,m_1} of a basis function coefficient γ_{j,m_1} to the signal in the ℓ_2 norm is thus

$$c_{j,m_1} = \gamma_{j,m_1} \sum_{m_2} \gamma_{j,m_2} \sum_{l} g_{j,m_1,l}\ g_{j,m_2,l}\ \alpha_{j+1,l} \quad \text{for} \quad \{m_2 \in \mathcal{M}(j) \mid p(T_{j,m_1}) = p(T_{j,m_2})\}\,.$$

□

Finding the optimal approximation in the Bio-Haar basis is significantly more expensive than the k-largest approximation for orthonormal bases. However, overall the computational costs are still moderate.

6.2.5 Error Computation for Rotation

Let

$$S = \sum_{k_1 \in \mathcal{K}(n_1)} c_{k_1} \tau_{n_1,k_1} \quad \text{and} \quad S_r = \sum_{k_2 \in \mathcal{K}(n_2)} c_{k_2} \tau_{n_2,k_2}$$

be the representations of a (reconstructed) signal before and after rotation in a spherical wavelet basis, and let the error introduced by the rotation be

$$E_p = \|S - S_r\|_p.$$

To simplify the notation, in the following we will omit the indices n_1 and n_2 so that $\tau_{k_1} \equiv \tau_{n_1,k_1}$ and $\tau_{k_2} \equiv \tau_{n_2,k_2}$. As discussed in Section 5.2, the partitions over which S and S_r are defined have in general different alignments and thus resampling is necessary to obtain the error E_p. For a fixed source partition τ_{k_1}, let $\left\{\tau_{k_2}^{k_1}\right\}$ be the set of all target partitions that overlap with τ_{k_1}. The difference between the weighted average color of the $\tau_{k_2}^{k_1}$ and the color of τ_{k_1} yields then the error for the fixed source partition. The weights w_{k_1,k_2} of the target partitions are given by the normalized overlaps, that is

$$w_{k_1,k_2} = \frac{\alpha_{k_1,k_2}}{\alpha_{k_1}},$$

where α_{k_1,k_2} denotes the overlap between τ_{k_1} and $\tau_{k_2}^{k_1}$, and α_{k_1} is the area of the fixed source partition τ_{k_1}. Similar to the computation of the rotation matrices, for the Haar

cubemap basis the domains over which the signals are defined have to be aligned prior to resampling. We again employed the approach outlined in Section 5.3 and projected the source partitions onto the domains of the target partitions.

Next to the errors in the ℓ_1 and the ℓ_2 norm, we also analysed the sparsity of the rotation matrices. This is an important measure for the computational costs of performing basis transformations (cf. Chapter 2.7 in [68]). In the plots in this chapter instead of the sparsity the density of the rotation matrices is shown, this measure is defined as the number of nonzero elements in a matrix over the total number of elements.

The error introduced by the rotation and the sparsity of the rotation matrices depend on the particular rotation. For example for a spherical Haar wavelet basis defined over a partition derived from an octahedron, a rotation by multiples of $\pi/2$ around the principal axes does not introduce any error. It is easy to see that the partitions of the source and target basis are aligned in these cases. However, as already discussed, general rotations suffer from resampling artifacts. We used a Monte-Carlo approach to sample the space of all possible rotations and to obtain the results reported in Section 6.6.

6.2.6 Approximation of Rotation Matrices

Many of the nonzero coupling coefficients in a basis transformation matrix are very small (cf. Section 6.6.3). Intuitively, it might thus be possible to approximate basis transformations with small error by employing only the k largest coupling coefficients. Analogous to the discussion in Section 6.2.4, the question then arises if discarding the smallest basis function coefficients yields the optimal approximation, or if otherwise the subset of the coupling coefficients which minimizes the projection error for a fixed number of nonzero coefficients can still be found efficiently.

In the following, it will be shown that in general the k largest coupling coefficients do *not* yield the optimal approximation, and that the optimal set of coupling coefficients is

unlikely to be found efficiently.

Let

$$S_r = \sum_{i_2 \in \mathcal{I}_2} \left(\sum_{i_1 \in \mathcal{I}_1} c_{i_1} \, \beta_{i_1,i_2} \right) \hat{\psi}_{i_2}$$

be the projection of a signal $S = \sum_{i_1} c_{i_1} \hat{\psi}_{i_1}$ from a source wavelet basis with basis functions $\hat{\psi}_{i_1}$ onto a target wavelet basis with basis functions $\hat{\psi}_{i_2}$. An approximation of the projection can be obtained by using only a subset of the coupling coefficients. For fixed i_2, let $\bar{\mathcal{I}}_1^{i_2} \subset \mathcal{I}_1$, with $\#\bar{\mathcal{I}}_1^{i_2} < \#\mathcal{I}_1$, be the index set which runs over the nonzero coupling coefficients after approximation. The projection is then

$$\bar{S}_r = \sum_{i_2 \in \mathcal{I}_2} \left(\sum_{i_1 \in \bar{\mathcal{I}}_1^{i_2}} c_{i_1} \beta_{i_1,i_2} \right) \hat{\psi}_{i_2}.$$

Index sets $\Pi_1^{i_2}$ of coefficients which have been discarded by the approximation can be defined as $\Pi_1^{i_2} = \mathcal{I}_1 \setminus \bar{\mathcal{I}}_1^{i_2}$. The approximation error in an ℓ_p norm, for fixed but arbitrary $0 < p < \infty$, is thus

$$\begin{aligned}
\|S_r - \bar{S}_r\|_p &= \left(\int_{\mathbb{S}^2} \left| \, S_r - \bar{S}_r \, \right|^p d\omega \right)^{1/p} \\
&= \left(\int_{\mathbb{S}^2} \left| \sum_{i_2 \in \mathcal{I}_2} \left(\sum_{i_1 \in \mathcal{I}_1} c_{i_1} \, \beta_{i_1,i_2} \right) \hat{\psi}_{i_2} - \sum_{i_2 \in \mathcal{I}_2} \left(\sum_{i_1 \in \bar{\mathcal{I}}_1^{i_2}} c_{i_1} \, \beta_{i_1,i_2} \right) \hat{\psi}_{i_2} \right|^p d\omega \right)^{1/p} \\
&= \left(\int_{\mathbb{S}^2} \left| \sum_{i_2 \in \mathcal{I}_2} \left(\sum_{i_1 \in \Pi_1^{i_2}} c_{i_1} \, \beta_{i_1,i_2} \right) \hat{\psi}_{i_2} \right|^p d\omega \right)^{1/p} . \qquad (6.7)
\end{aligned}$$

The sum $\sum_{i_1 \in \Pi_1^{i_2}} c_{i_1} \, \beta_{i_1,i_2}$ in Eq. 6.7 yields real numbers and the equation is therefore similar to Eq. 6.1. It follows that it is very difficult to obtain the optimal approximation of a basis transformation in an ℓ_p norm, for arbitrary $0 < p < \infty$.

With Eq. 6.7, the squared error in the ℓ_2 norm is

$$\left(\|S_r - \bar{S}_r\| \right)^2 = \int_{\mathbb{S}^2} \left(\sum_{i_2 \in \mathcal{I}_2} \left(\sum_{i_1 \in \Pi_1^{i_2}} c_{i_1} \, \beta_{i_1,i_2} \right) \hat{\psi}_{i_2} \right)^2 d\omega.$$

For an orthonormal basis this can be simplified to

$$= \sum_{i_2 \in \mathcal{I}_2} \left(\sum_{i_1 \in \Pi_1^{i_2}} c_{i_1} \ \beta_{i_1,i_2} \right)^2 .$$

Minimizing the sum $\sum_{i_1 \in \Pi_1^{i_2}} c_{i_1} \beta_{i_1,i_2}$ is however still difficult. Therefore, also for $p = 2$ and an orthonormal basis it is unlikely that an efficient algorithm for obtaining the optimal approximation of a basis transformation matrix exists.

Rather than using a fixed number of basis function coefficients for the approximation of the rotation matrices, we employed in the experiments a threshold $t \in [0, 1]$ in the range of the matrix elements to find the coupling coefficients which are assumed to be zero. As shown above, this approximation strategy does in general not minimize the projection error. However, it is data-independent and can be computed off-line.

6.2.7 Experimental Setup

To increase the comparability of the results, all experiments have been performed with the same parameters and settings, and usually only one parameter was varied to obtain specific results.

For the Bio-Haar basis the k largest coefficients c_{j,m_1}, as derived in Chapter 6.2.4, were used to obtain approximations; for all other bases the k-largest approximation strategy has been employed. The input signals were defined over domains on level eight of the partition trees. A full wavelet transform therefore yielded for each tree $16,834$ basis function coefficients defined over seven levels. The octahedron was used as the base polyhedron for all spherical Haar wavelet bases.

For the rotation experiments, the source basis was always a rotated version of the target basis as defined in Chapter 5.2.1, and both the basis function coefficient vectors of the signals and the rotation matrices were not approximated.

6.3 Implementation

The experiments presented in this chapter were devoted to exploring and better understanding the properties of the SOHO wavelet basis. The implementation therefore closely resembled the underlying mathematics and was designed to provide a flexible framework to conduct the experiments. Similar to Schröder and Sweldens [76], we employed a tree data structure to represent the partitions and the basis functions. This simplified the computation of statistics and allowed us to easily relate additional data to the nodes. Performance considerations were of no concern in the implementation because the fast wavelet transform guaranteed the existence of linear-time algorithms for the basis projection of a signal and for reconstruction. All experiments were implemented in the Matlab programming environment [51] and computations were performed exclusively in double precision.

The experiments showed that the implementations are very similar for all spherical Haar wavelet bases. The computations for the SOHO wavelet basis differed in that not the geodesic bisector was used to obtain the new vertex positions during subdivision. In contrast to the true spherical Haar wavelet bases, for the pseudo Haar basis at runtime no computation of the filter coefficients was necessary.

We also performed some initial experiments with the *CUDA* general purpose parallel programming language for graphics processing units [59]. These verified that the wavelet transforms for the SOHO wavelet basis can be computed very efficiently. The implementation additionally showed that the computations are amenable to parallelization which is an increasingly important factor for the practical efficiency of algorithms (cf. [62, 63]).

The numerical stability of the SOHO wavelets is guaranteed by the orthonormality of the basis. During our experiments we observed however that it is for the basis advantageous to employ the numerical inverse of the analysis matrix for reconstruction rather than an analytically computed synthesis matrix. Only this guaranteed in the experiments perfect

reconstruction. Otherwise, approximately one digit of precision was lost during each level of the transform.

To compute the coupling coefficients which form the basis transformation matrices it is necessary to determine the overlap between partitions of the source and target basis. For spherical Haar wavelets, the analogue of a 2D clipping algorithm on $\mathbb{S}^2$ was used to obtain the spherical polygon that prescribes the overlap. The area of the polygon was obtained by first subdividing it into spherical triangles and then computing the area of the triangles. For the Haar cubemap basis we used a clipping algorithm on the faces of the cubemap to determine the overlap between a partition of the projected source basis and the domains on the finest level of the target partition. In the future, a rasterization algorithm might provide significantly better performance to obtain the overlap. For the spherical Haar wavelets and the Haar cubemap basis we employed the hierarchical, strictly nested structure of the partition trees to avoid unnecessary computations; that is, if two partitions are disjoint then with Eq. 5.4, and the analogue for the Haar cubemap basis, it is guaranteed that the coupling coefficients between basis functions which are defined over the descendants of the two partitions are zero.

6.4 Properties of the SOHO Wavelet Basis

6.4.1 Optimal SOHO Wavelet Basis

Let Ψ_+ and Ψ_- be SOHO wavelet bases where the plus and the minus sign has been used to compute the parameter a in Eq. 4.15, respectively. Basis functions of Ψ_+ and Ψ_- are shown in Figure 4.2.

Figure 6.2 shows the approximation performance of the two bases. For the texture map and the visibility map, Ψ_- performs better than Ψ_+ in both error norms. For the BRDF,

in the ℓ_2 norm both bases provide almost identical results, and in the ℓ_1 norm slight advantages for Ψ_+ can be observed for this signal. We argue that Ψ_- provides overall better results than Ψ_+. In the following, we will therefore refer to Ψ_- as the SOHO wavelet basis.

6.4.2 Structure of Basis Function Coefficient Vectors

For the SOHO wavelet basis, the Bio-Haar basis, and the pseudo Haar wavelets, Figure 6.4 and Figure 6.5 show mean values of the magnitude of the basis function coefficients on different levels. For all bases an exponential decay (linear in the semi-log plot) in the magnitude of the coefficients can be observed. Figure 6.4 shows that the basis function coefficients for the Bio-Haar basis decay significantly slower than for the SOHO wavelet basis.

In Figure 6.6 and Figure 6.7, the nonzero basis function coefficients over different levels are reported. For the texture map and the BRDF, only a very small number of basis function coefficients is zero for all three bases. This is particularly surprising in the light of the results in Figure 6.4 and Figure 6.5 where an exponential decay in the magnitude of the coefficients has been observed. For the visibility map, shown in Figure 6.7, the number of coefficients which are zero is significantly larger than for the other two signals. A considerable number of nonzero coefficients can still be observed for the SOHO wavelet basis reaching about 80% on level seven. For the Bio-Haar basis about 50% of the basis function coefficients are nonzero on this level. The pseudo Haar basis has a significantly smaller number of nonzero coefficients than the other two bases and at level seven only about 5% of the coefficients are nonzero. We believe that the superior performance of the pseudo Haar basis results from the fact that it is not basis of $L_2(\mathbb{S}^2, d\omega)$; that is, the basis is not able to represent small details and, in contrast to the true spherical Haar wavelet bases, the basis function coefficients are therefore zero.

6.5 Efficiency of Signal Approximation

6.5.1 Optimal Approximation for the Bio-Haar Basis

For the Bio-Haar basis, in Figure 6.3 the k-largest and the optimal approximation strategy derived in Chapter 6.2.4 are compared. The plots show clearly that for the semi-orthogonal Bio-Haar basis the k-largest approximation strategy provides significantly higher error rates than the optimal approximation. An interesting aspect of the results is that the optimal approximation strategy in the ℓ_2 norm also yields lower error rates in the ℓ_1 norm.

6.5.2 Comparison of Spherical Haar Wavelet Bases

For the spherical Haar wavelet bases employed in the experiments, in Figure 6.8 to Figure 6.11 the errors rates in the ℓ_1 and ℓ_2 norm for the approximation of signals with different numbers of nonzero basis function coefficients are shown.

For both error norms, the basis Bonneau2 performs very similar to the SOHO wavelets; in fact, in the plots the two bases are in most cases indistinguishable. For the visibility map, the ℓ_1 and ℓ_2 error rates for the basis Bonneau1 are higher than for the SOHO wavelet basis; for the other two signals both bases achieve very similar results. The two bases developed by Nielson et al. provide almost the same error rates as the SOHO wavelets for the texture map; for the visibility map however, in particular in the ℓ_1 norm, the error rates are higher. The basis Nielson1 is for the BRDF slightly worse than the SOHO wavelet basis whereas the basis Nielson2 provides slight advantages. With the exception of the BRDF where the pseudo Haar wavelets achieve similar results than the SOHO wavelet basis, the Bio-Haar wavelets and the pseudo Haar basis provide for all signals higher error rates than the other bases.

The graphs in Figure 6.9 and Figure 6.11 show that the approximation error for the visibility map vanishes if $8,192$ or more nonzero basis function coefficients are employed for the reconstruction. About five percent of the coefficients are thus sufficient to capture the whole information of the signal. This verifies that Haar-like bases are very efficient for the representation of piecewise constant signals.

Figure 6.12 to Figure 6.17 show reconstructions of approximated signals for the SOHO wavelet basis, the Bio-Haar basis, and the pseudo Haar wavelets. The plots for the nearly orthogonal bases look in most cases very similar to those for the SOHO wavelet basis and are therefore omitted. Detail views of the reconstructed texture map are provided in Figure 6.18 to Figure 6.21. For the texture map 6.25%, or $8,192$, of the basis function coefficients were nonzero for the reconstruction. For the visibility and the BRDF 0.78%, or $1,024$, of the basis function coefficients were retained. For comparison signals that have been obtained by reconstruction with the full coefficient vectors are provided.

Although any judgement of the results is limited by the subjectivity of the perceived error, we believe that the SOHO wavelet basis provides for all signals visually significantly better results than the other two spherical Haar wavelet bases shown in the comparison. For the texture map, the SOHO wavelet basis yields sharper edges and the signal appears less noisy. The basis is also able to preserve more details. This can be observed in particular in the detail views, for example in the regions corresponding to Italy and Cuba. For the BRDF, the reconstructed signal for the SOHO wavelet basis appears significantly smoother than the signals for the other two bases and it is therefore more similar to the original function. Although differences to the reconstruction with the full coefficient vector are visible, all bases capture the characteristics of the BRDF well with a very small number of basis function coefficients. This shows that Haar-like bases are also suitable for the representation of smooth signals. For the visibility map, the SOHO wavelet basis provides again sharper edges than the Bio-Haar basis and the pseudo Haar wavelets.

6.5.3 Comparison of Partitions

The SOHO wavelet basis can be defined over a partition derived from a tetrahedron, an octahedron, or an icosahedron. In the following, we will refer to these bases as Ψ_T, Ψ_O, and Ψ_I, respectively. Figure 6.22 to Figure 6.25 show the error rates in the ℓ_1 and the ℓ_2 norm resulting from an approximation of signals in the different SOHO wavelet bases. For high approximation ratios, Ψ_I provides the best results in the ℓ_2 norm. With an increasing number of nonzero coefficients however, Ψ_T becomes increasingly better and with more than $32,768$ basis function coefficients this basis provides superior results. In the ℓ_2 norm, the results obtained with Ψ_O lie in between those for Ψ_T and Ψ_I. In the ℓ_1 norm, no clear advantage for any of the bases can be observed. For the BRDF, the base polyhedron has almost no effect on the performance and all bases perform very similar. For the texture map, Ψ_T provides significantly better results than the other two bases; the basis is however only slightly better than Ψ_O for the visibility map. In the ℓ_1 norm, for the texture map and the visibility map Ψ_I provides higher error rates than Ψ_T and Ψ_O.

In Figure 6.26 and Figure 6.27 reconstructed signals obtained from Ψ_T, Ψ_O, and Ψ_I with 6.25% nonzero basis function coefficients are shown. Artifacts are clearly visible for the signal obtained from Ψ_T. Visually, Ψ_O and Ψ_I provide similar results. However, we believe that the structure of the partition is more visible for Ψ_I.

6.6 Properties of Rotation Matrices

6.6.1 Comparison of Spherical Haar Wavelet Bases

The errors rates in the ℓ_1 and the ℓ_2 norm resulting from rotations of the test signals in the SOHO wavelet basis, the Bio-Haar basis, and the pseudo Haar wavelets are shown

in Figure 6.32 to Figure 6.34. For the texture map, the SOHO wavelet basis provides in both the ℓ_1 and the ℓ_2 norm the lowest error rates, thereby only slightly outperforming the Bio-Haar basis. The results for the BRDF are similar. For the visibility map, the Bio-Haar basis is slightly better than the SOHO wavelet basis in both error norms. The pseudo Haar basis provides for the BRDF and the visibility map in both the ℓ_1 and the ℓ_2 norm significantly higher error rates than the other two bases. Only for the texture map, the error rates for this basis are similar to those for the SOHO wavelets and the Bio-Haar basis. Figure 6.35 shows that the rotation matrices for the Bio-Haar wavelets are significantly sparser than the matrices for the SOHO wavelet basis and the pseudo Haar basis. This results from the smaller support of the wavelet basis functions for the Bio-Haar basis.

In Figure 6.36 and Figure 6.37 reconstructions of rotated signals in the target basis are shown. In Figure 6.37 also the plot of a rotated signal in the source basis is provided. For all bases the reconstructions appear smoothed which results from the unavoidable resampling. The Bio-Haar basis preserves thereby slightly less detail than the SOHO wavelet basis. Clearly visible is the loss of detail for the pseudo Haar basis. This corresponds well to the results in the error plots.

6.6.2 Rotation Matrices for the Haar Cubemap Basis

In Figure 6.38 to Figure 6.40 the ℓ_1 and ℓ_2 error rates resulting from the rotation of signals in the SOHO wavelet and the Haar cubemap basis are compared. For the texture map and for the visibility map, the SOHO wavelet basis provides significantly lower error rates in both error norms. For the BRDF, the ℓ_2 error rates for both representations are almost identical, and in the ℓ_1 norm the Haar cubemap basis provides lower error rates. In Figure 6.41 the density of the rotation matrices for the two bases is compared. The plots show that the SOHO wavelet basis provides consistently sparser matrices.

6.6.3 Approximation of Rotation Matrices

For the SOHO wavelet basis and the Haar cubemap basis, in Figure 6.42 the ℓ_1 and ℓ_2 error rates resulting from the rotation of the texture map with approximated rotation matrices are shown. The results for other levels and the remaining test signals are similar and therefore omitted. For the experiments discussed in this section the test signal was defined on level four.

For both error norms and for both bases, the error resulting from the rotation increase almost linearly with increasing approximation threshold t. The density of the approximated rotation matrices decreases however exponentially. This is shown in Figure 6.43.

6.7 Discussion

What representation is best suited for an application has to be decided in the specific context. We nonetheless believe that the results presented in this chapter affirm that the SOHO wavelet basis is an attractive representation for a wide range of applications.

In Chapter 6.5 the approximation performance of the different spherical Haar wavelet bases employed in the experiments has been compared. Both the numerical error measures and the quality of reconstructed signals demonstrated that the Bio-Haar basis and the pseudo Haar basis are less efficient for the approximation of signals than the other bases. The nearly orthogonal bases provided approximately the same performance as the SOHO wavelet basis. We expected that these bases are better suited for approximation than the Bio-Haar and the pseudo Haar basis but the observed performance was surprising to us. We initially thought that this might result from the high subdivision level on which the signals were defined. Additional experiments, whose results are not provided in this chapter, showed however that the nearly orthogonal bases achieve also for coarser resolutions of the input signals approximately the same error rates as the SOHO wavelet

basis. In practice a fully orthogonal basis provides therefore no clear advantage over a nearly orthogonal one. If this is also true for other applications such as product integral calculations has to be investigated in the future.

Although the pseudo Haar basis did, overall, not outperform the true spherical Haar wavelet bases, we were nonetheless surprised by its performance. For almost all experiments it provided competitive results. The assumption that the subdivision always yields child domains with equal area [47] seems therefore in practice to be reasonable. It will be interesting to explore if this is also true for other applications such as product integral calculations.

Although the spherical Haar wavelet bases employed for the experiments performed best for the piecewise constant visibility map, the results from Chapter 6.5 nonetheless demonstrate that the bases are also efficient for the representation of *all-frequency* signals. These results affirm earlier observations by Schröder and Sweldens [76] and Ng et al. [56].

As discussed in Chapter 6.4.2 when signals are represented without approximation, for the SOHO wavelet basis a significantly smaller proportion of the basis function coefficients is zero than for the Bio-Haar and pseudo Haar basis. It thus seems to be surprising that the SOHO wavelets outperform the other two bases for the approximation of signals. We believe that this discrepancy hints that the SOHO wavelet basis is able to better decorrelate signals. This argument is strengthened by the results provided in Figure 6.28 to Figure 6.31 where it is shown that for the SOHO wavelet basis a small fraction of the basis function coefficients is sufficient to capture the salient characteristics of a signal.

In Chapter 6.4.2 it was shown that the magnitude of the basis function coefficients decays exponentially with increasing level on which the coefficinets are defined. This result resembles observations made by Shapiro for $2D$ wavelets in image compression applications [79]. The decay in the magnitude of the coefficients is a statistical value and can be interpreted as an increasing likelihood for (spatial) correlations in signals

when the support of the basis functions decreases. Large basis function coefficients can however also be observed on high levels of wavelet transforms. These correspond to high-frequency features such as edges. Results from perception theory indicate that the preservation of these coefficients during approximation is particularly important for the perceived quality of reconstructed signals [79].

In Chapter 6.5.3 the approximation performance of SOHO wavelet bases defined over different base polyhedron has been compared. None of the platonic solids employed in the experiments showed thereby a clear advantage. However, we want to argue that for general applications the octahedron is the best choice. The corresponding basis provided always good results and in none of the experiments did it yield the highest error rates. A partition derived from an octahedron allows additionally to directly represent hemispherical signals, and the alignment of the faces of an octahedron with over parametrizations of the sphere is beneficial for many applications.

For the rotation of signals in a spherical Haar wavelet basis, the numerical results for the SOHO wavelets and the Bio-Haar basis were almost identical. Reconstructions of rotated signals show however that the SOHO wavelet basis is better suited for the rotation than the Bio-Haar basis. A comparison of the rotation performance of the SOHO wavelets and the Haar cubemap basis showed that rotation in the SOHO wavelet basis, both in terms of computational costs and of resulting error, is more efficient. We argue that this observation can be generalized and that spherically parametrized bases are more efficient than other representations for the rotation of signals.

The results from Chapter 6.6.3 demonstrate that the k-largest approximation strategy for rotation matrices provides good results in practice; although we showed that it is in general not optimal. For applications the strategy has the advantage that it is data-independent and can thus be computed off-line. The results from Chapter 6.6.3 also show that an approximation of the matrices is highly efficient: the error rates increase linearly with increasing approximation ratio but the number of nonzero coefficients de-

creases exponentially. Thus, with only modest additional error in the rotated signals, the computation time and the storage costs can be significantly reduced by approximating the rotation matrices.

In recent literature, it has often been argued that orthonormal bases are too restrictive to be useful in a wide range of applications. In particular the missing possibility to enforce additional constraints on the basis functions is considered as impractical. The results provided in this chapter show however that this argumentation is too simplistic. Many applications employ basis representations for the approximation of signals and the ability to efficiently compute the optimal approximation is therefore highly relevant. The k-largest approximation strategy can be computed very efficiently, and in the past it has therefore been used for a wide range of representations. The results from Section 6.5.1 show however that this approximation strategy is far from optimal for non-orthonormal bases.

Although for orthonormal bases the k-largest approximation strategy is provably optimal only in the ℓ_2 norm, the presented results, in particular those from Section 6.5.1, suggest that an optimal or good approximation strategy in the ℓ_2 norm provides also low error rates in the ℓ_1 norm and visually pleasing results.

6.8 Graphs

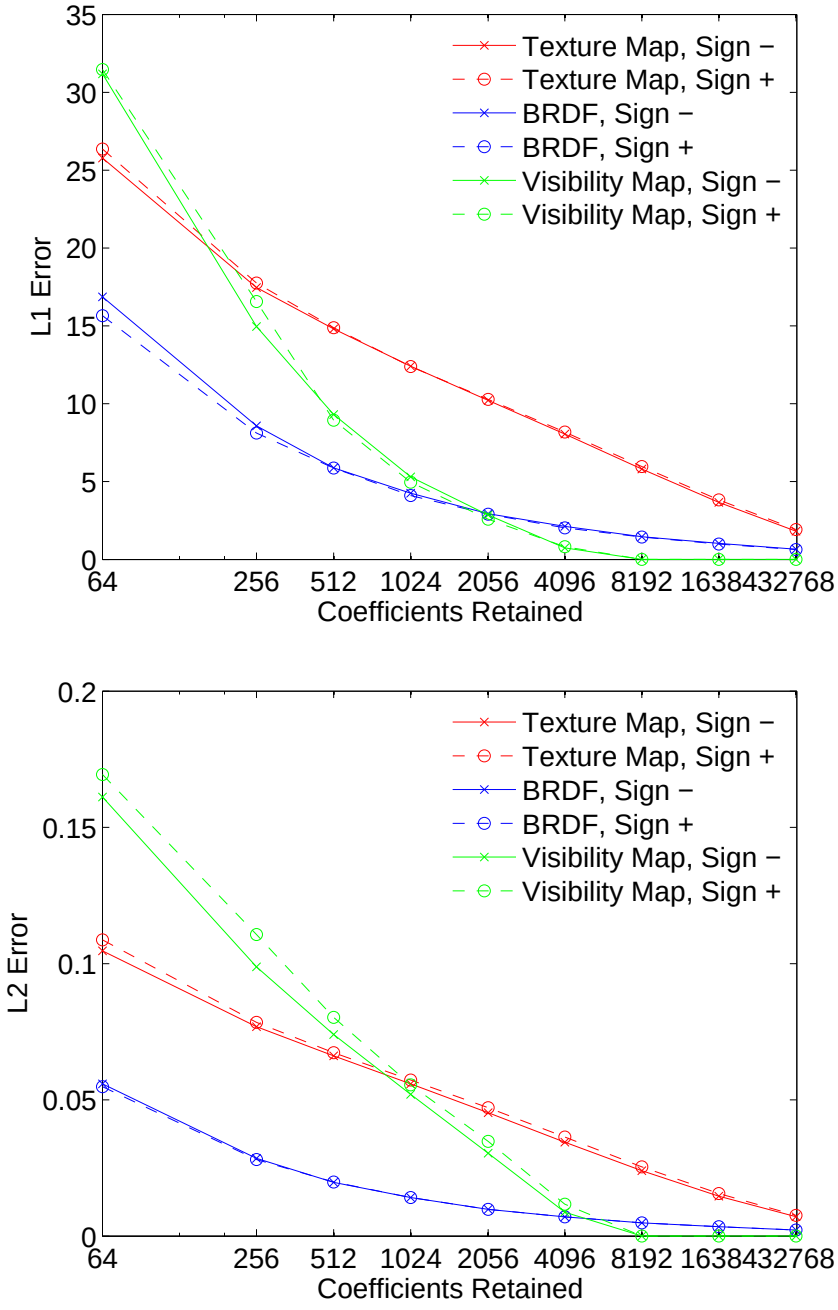

Figure 6.2: Performance of the SOHO wavelet basis for the two possible choices of the sign in the computation of parameter a in Eq. 4.15.

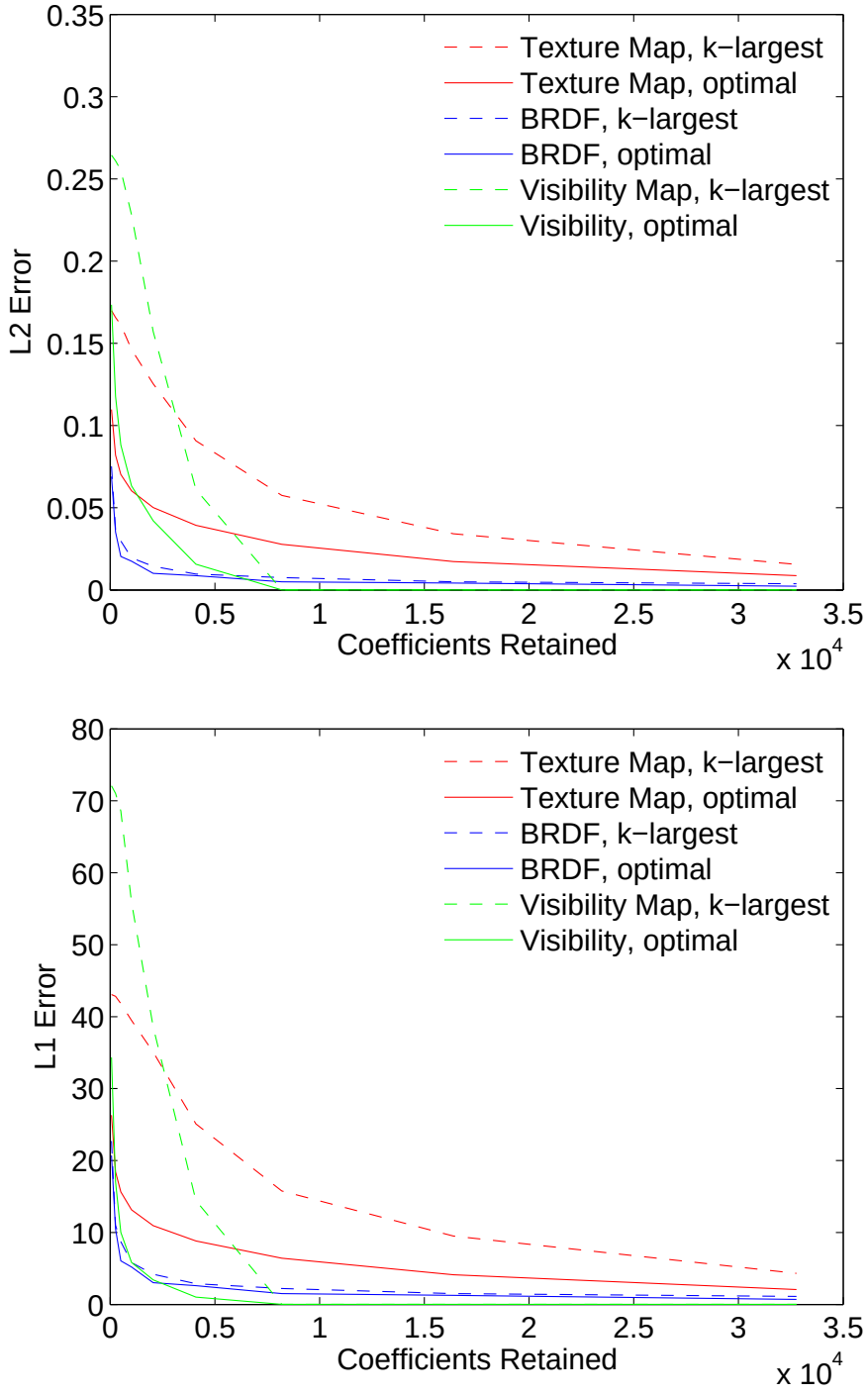

Figure 6.3: Optimal approximation in the ℓ_2 norm, as derived in Section 6.2.3, versus k-largest approximation for the Bio-Haar basis.

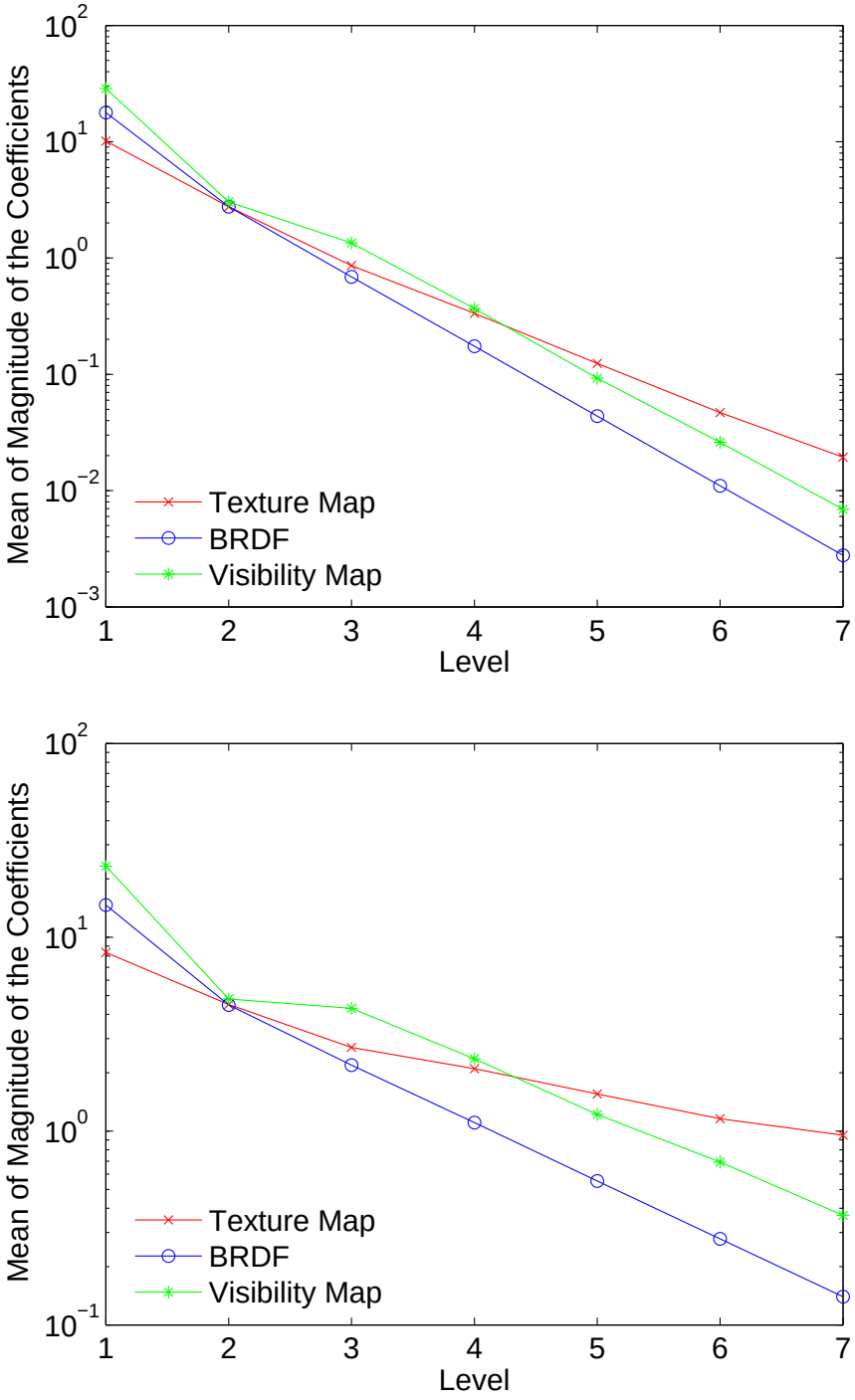

Figure 6.4: Decay of the magnitude of the basis function coefficients for the SOHO wavelet basis (top) and the Bio-Haar basis (top) with increasing level. The reported numbers are the mean over all coefficients at the level.

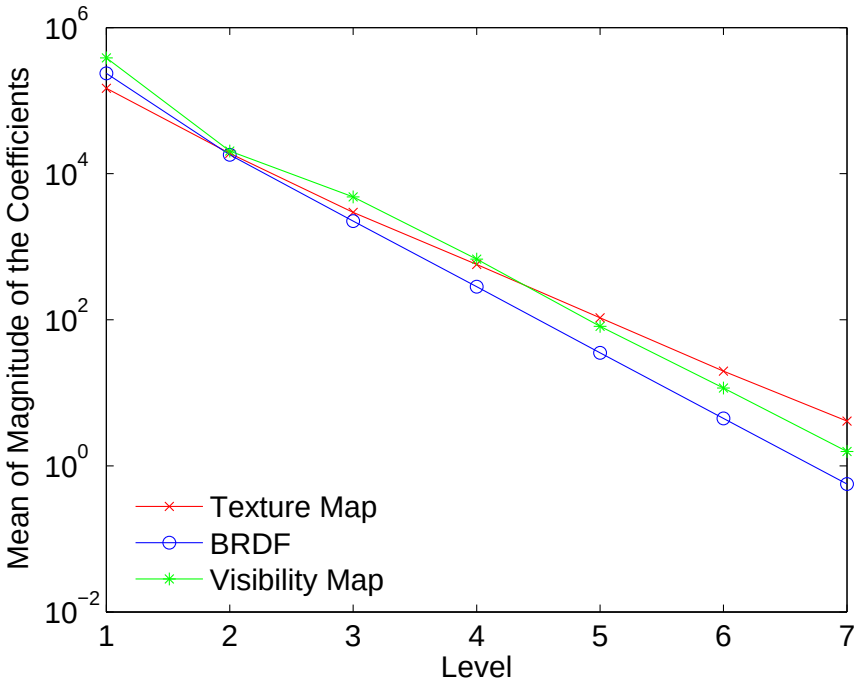

Figure 6.5: Decay of the magnitude of the basis function coefficients for the pseudo Haar basis with increasing level. The reported numbers are the mean over all coefficients at the level. The different scale of the coefficients compared to the SOHO wavelet basis and the Bio-Haar basis in Figure 6.4 results from the fact that the pseudo Haar basis is not normalized.

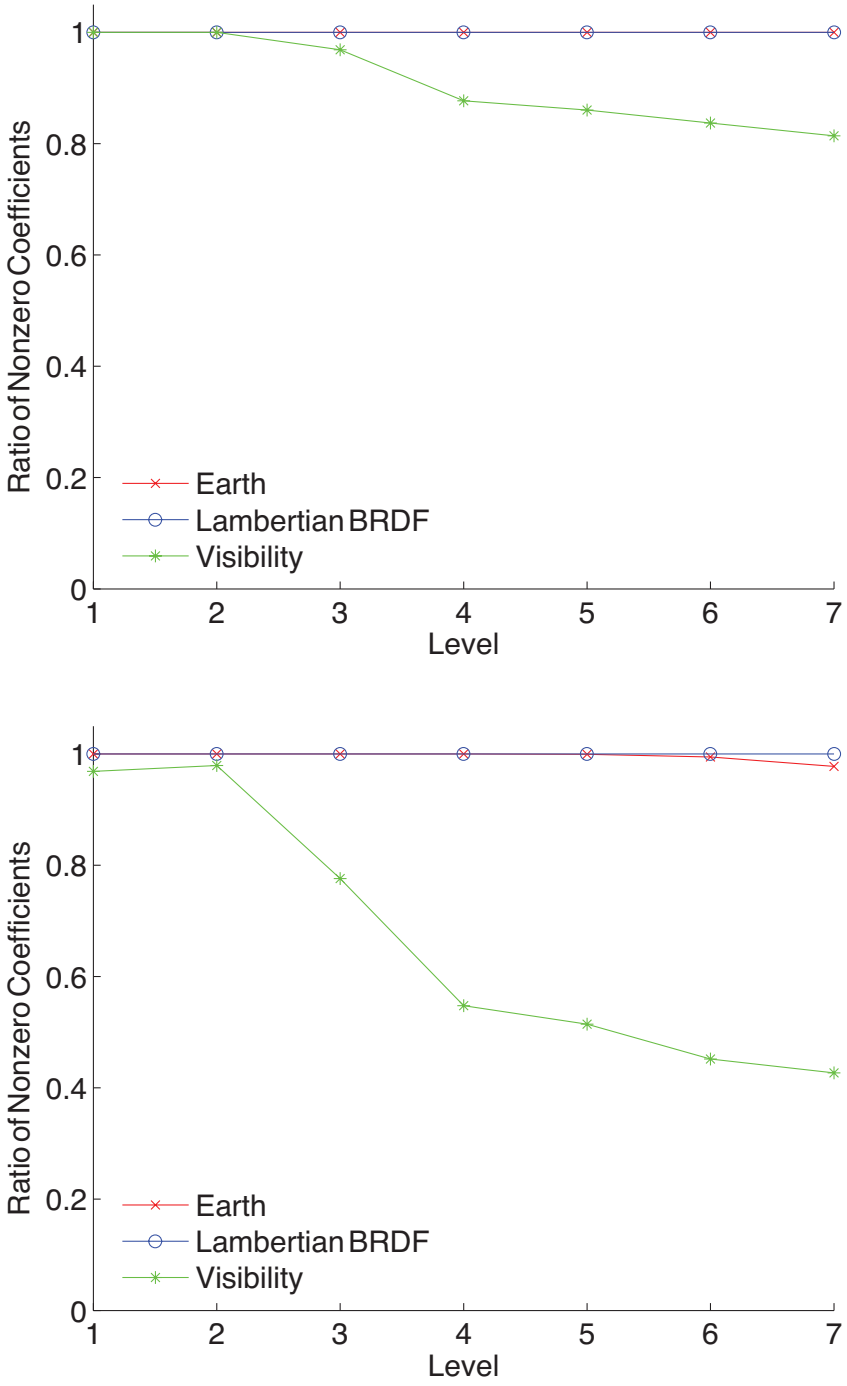

Figure 6.6: Fraction of nonzero coefficients for the SOHO wavelet basis (top) and the Bio-Haar basis (bottom). Note that some graphs coincide and are therefore not clearly visible.

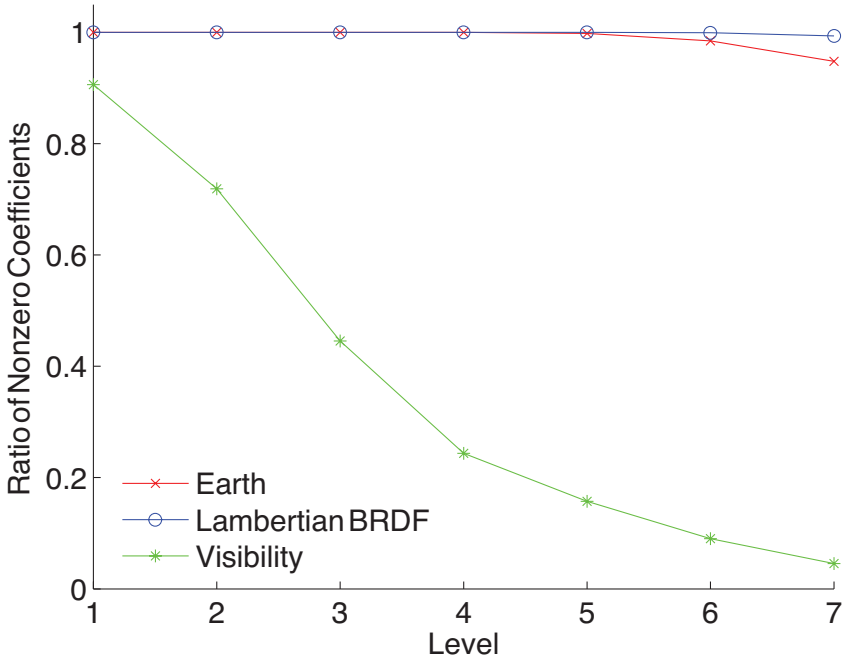

Figure 6.7: Fraction of nonzero coefficients on each level for the pseudo Haar basis. Note that some graphs coincide and are therefore not clearly visible.

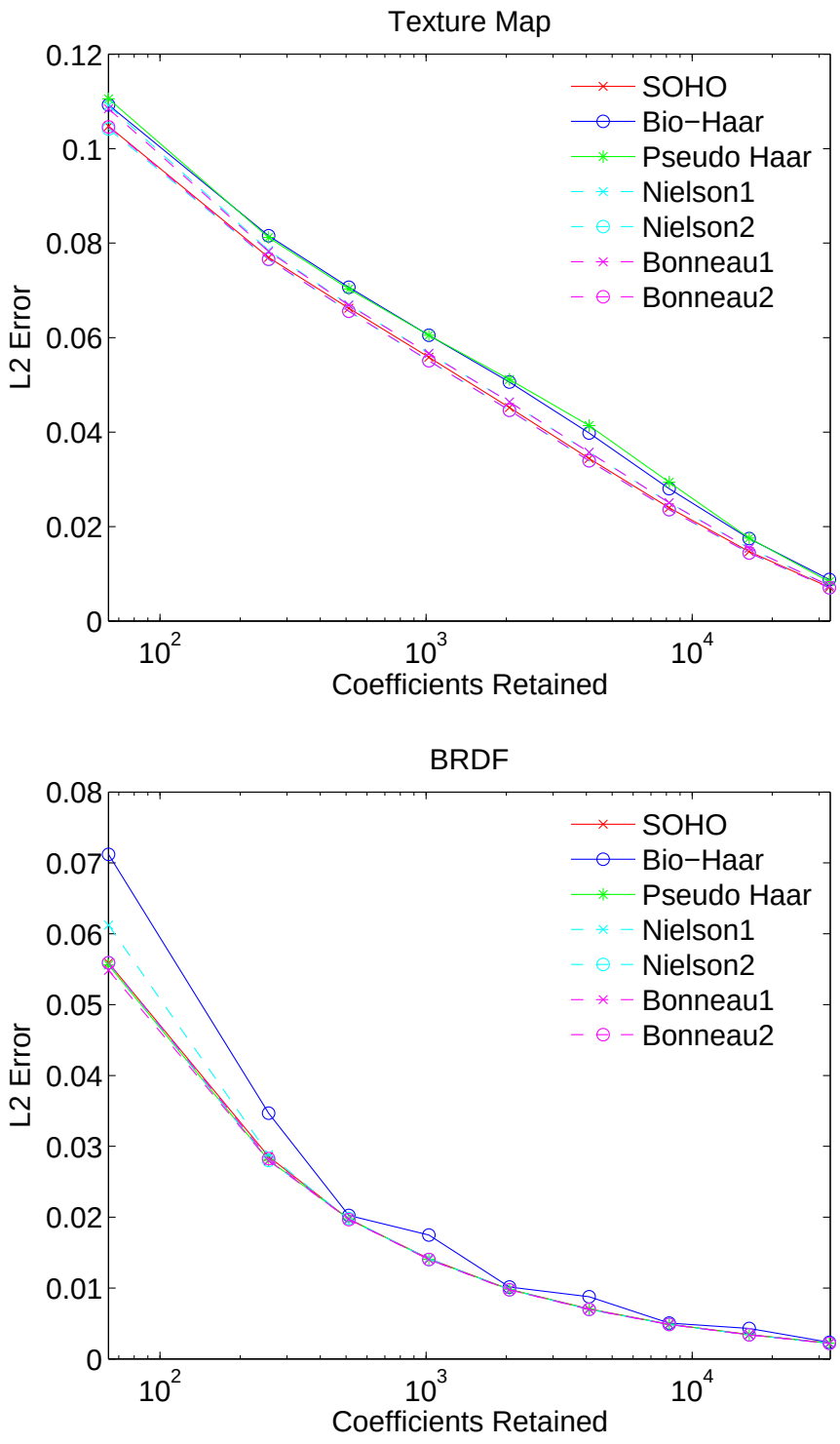

Figure 6.8: Approximation performance of spherical Haar wavelet bases in the ℓ_2 norm for the texture map (top) and the BRDF (bottom).

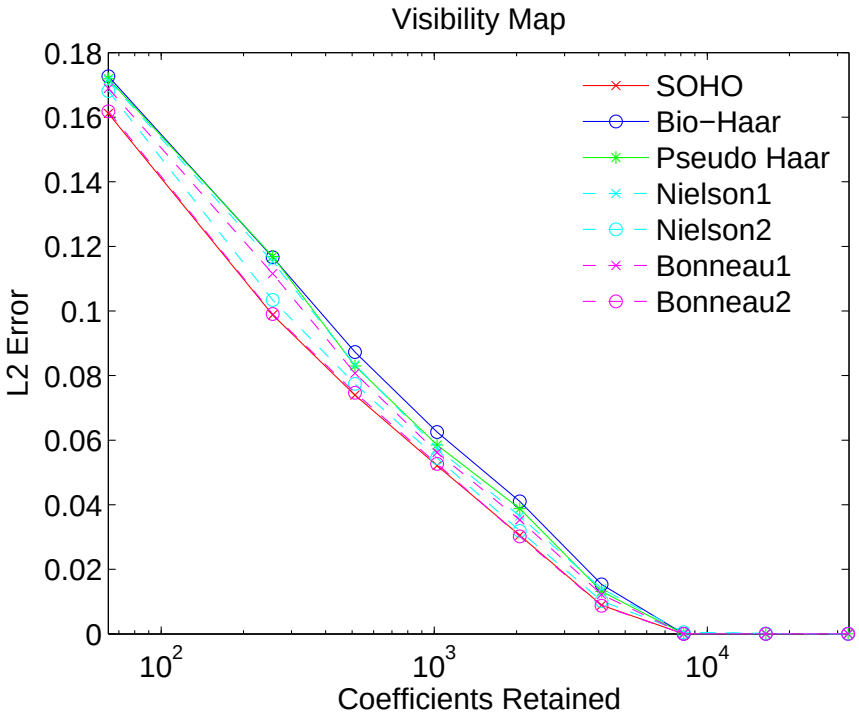

Figure 6.9: Approximation performance of spherical Haar wavelet bases in the ℓ_2 norm for the visibility map.

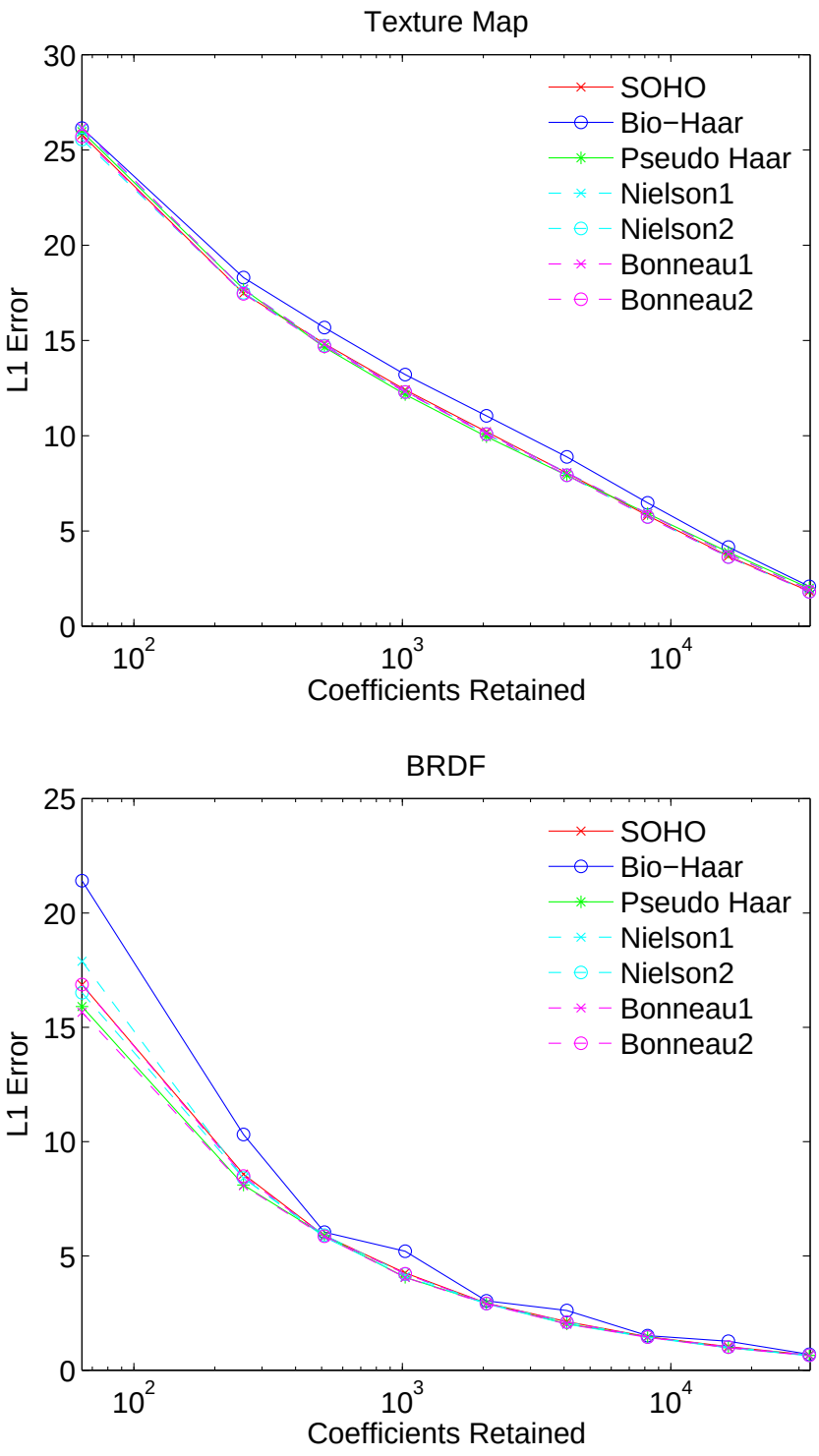

Figure 6.10: Approximation performance of spherical Haar wavelet bases in the ℓ_1 norm for the texture map (top) and the BRDF (bottom).

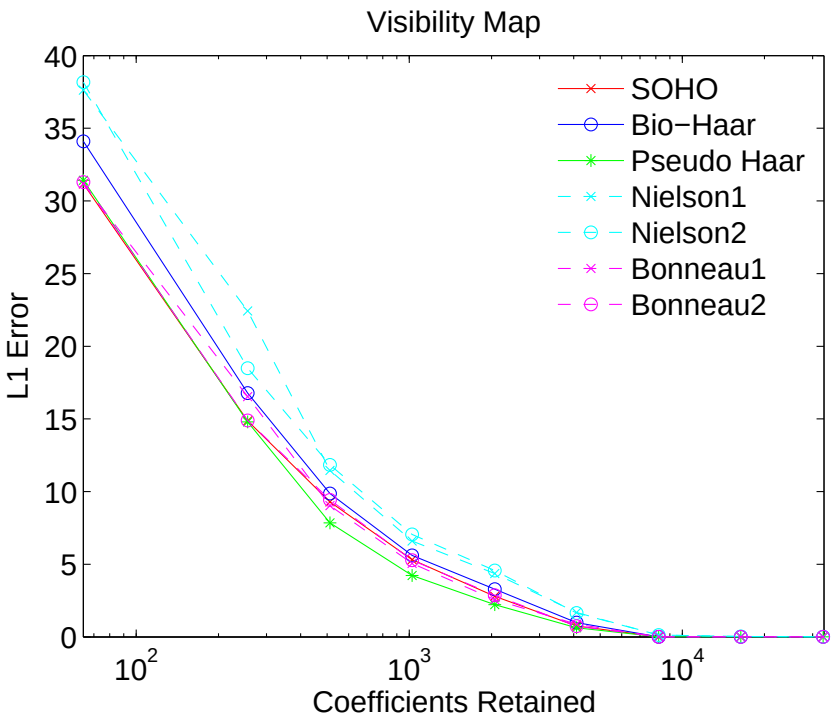

Figure 6.11: Approximation performance of spherical Haar wavelet bases in the ℓ_1 norm for the visibility map.

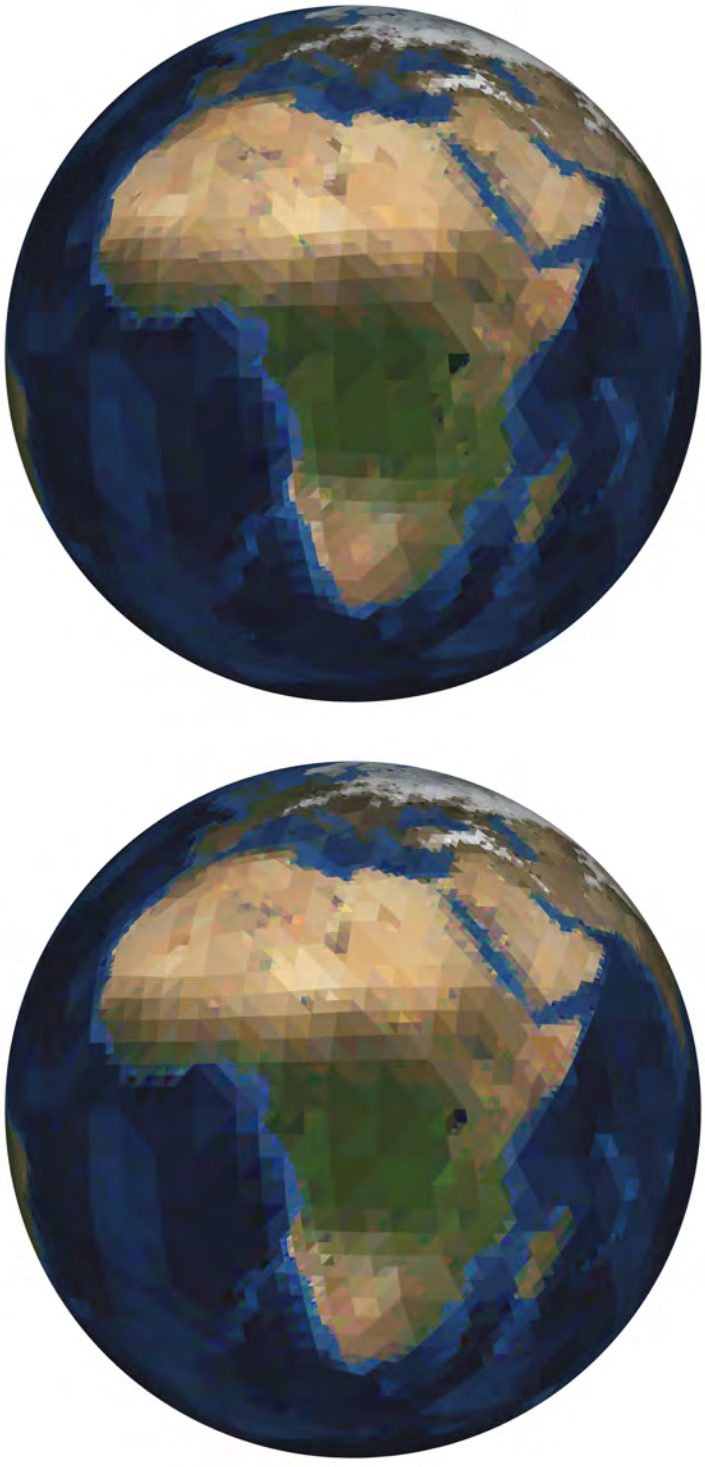

Figure 6.12: Reconstructed texture map for the SOHO wavelet basis (top) and the Bio-Haar basis (bottom) for an approximation which retained 6.25% of the basis function coefficients of the full signal.

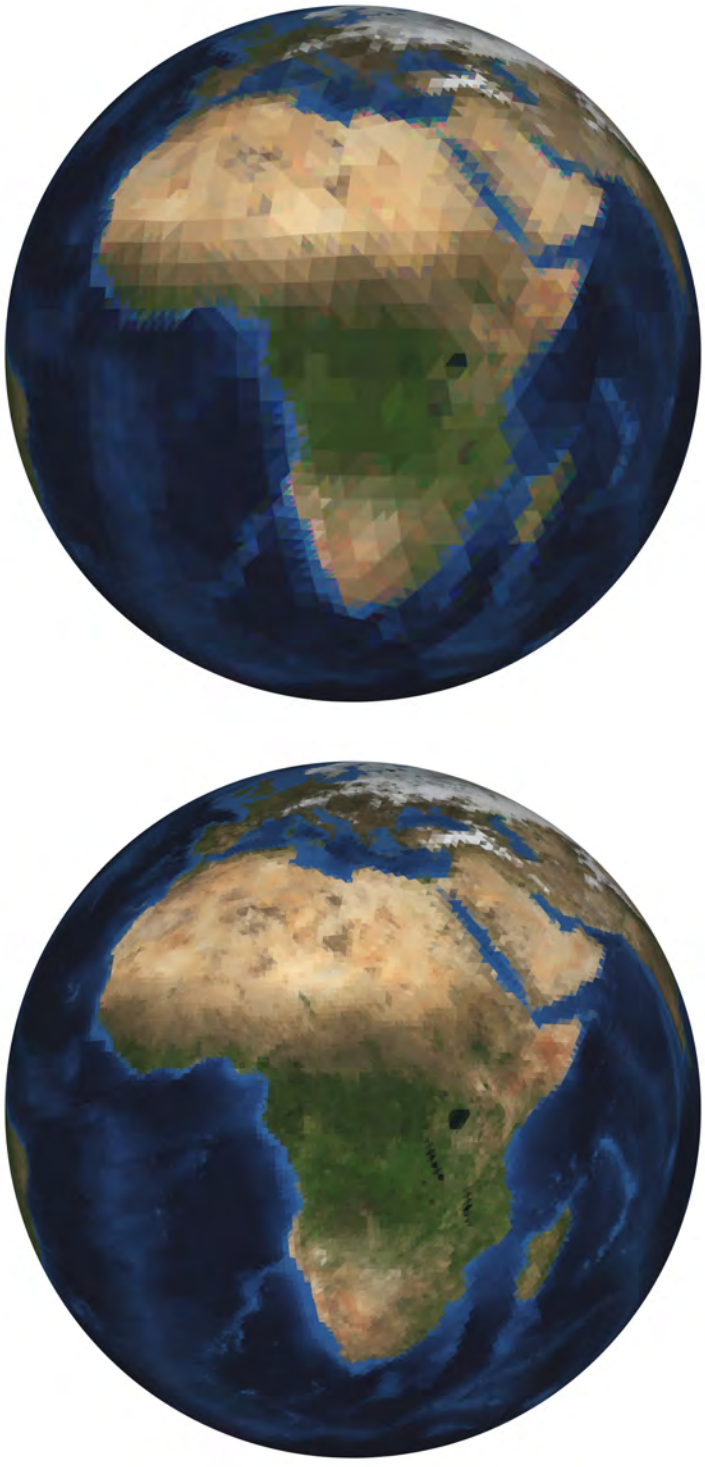

Figure 6.13: Reconstructed texture map for the pseudo Haar wavelets for an approximation which retained 6.25% of the basis function coefficients of the full signal (top), and a reconstruction with the full coefficient vector (bottom).

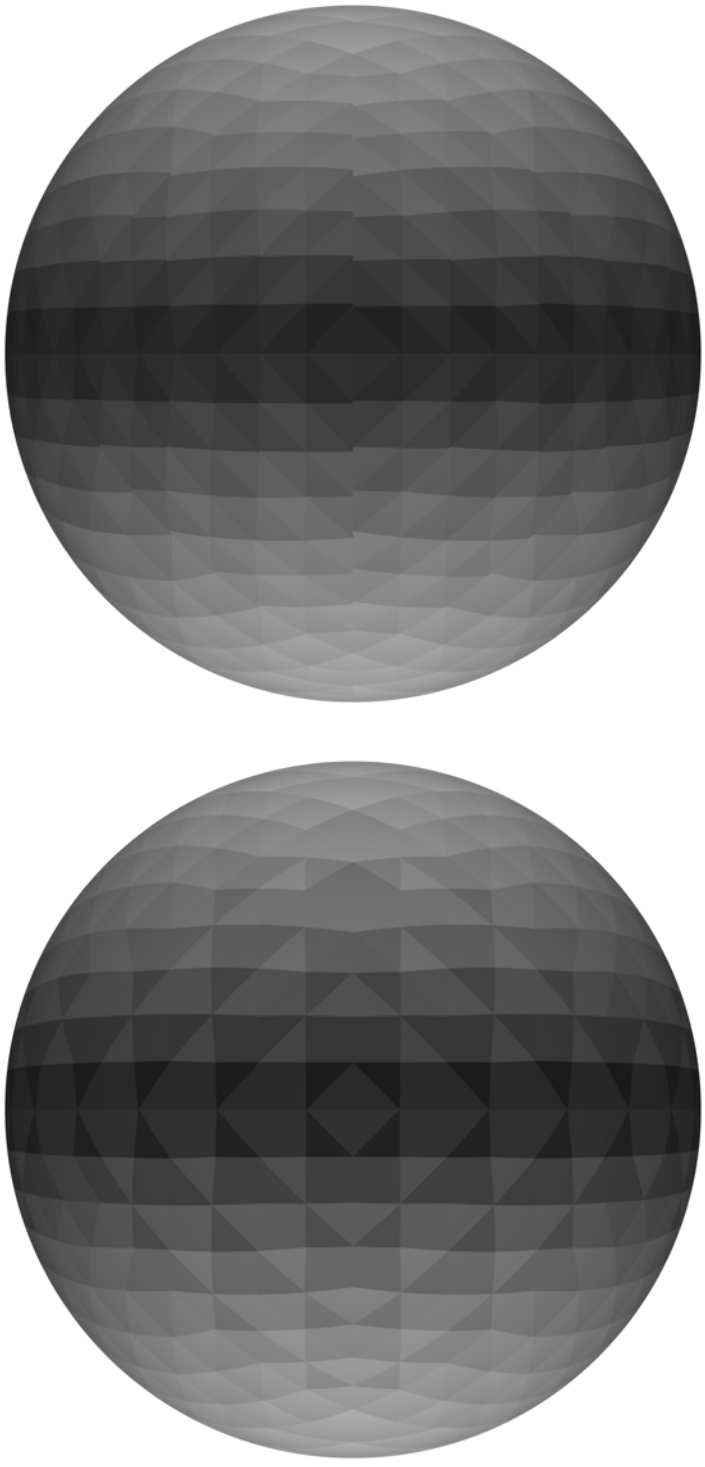

Figure 6.14: Reconstructed BRDF for the SOHO wavelet basis (top) and the Bio-Haar basis (bottom) for an approximation which retained 0.78% of the basis function coefficients of the full signal.

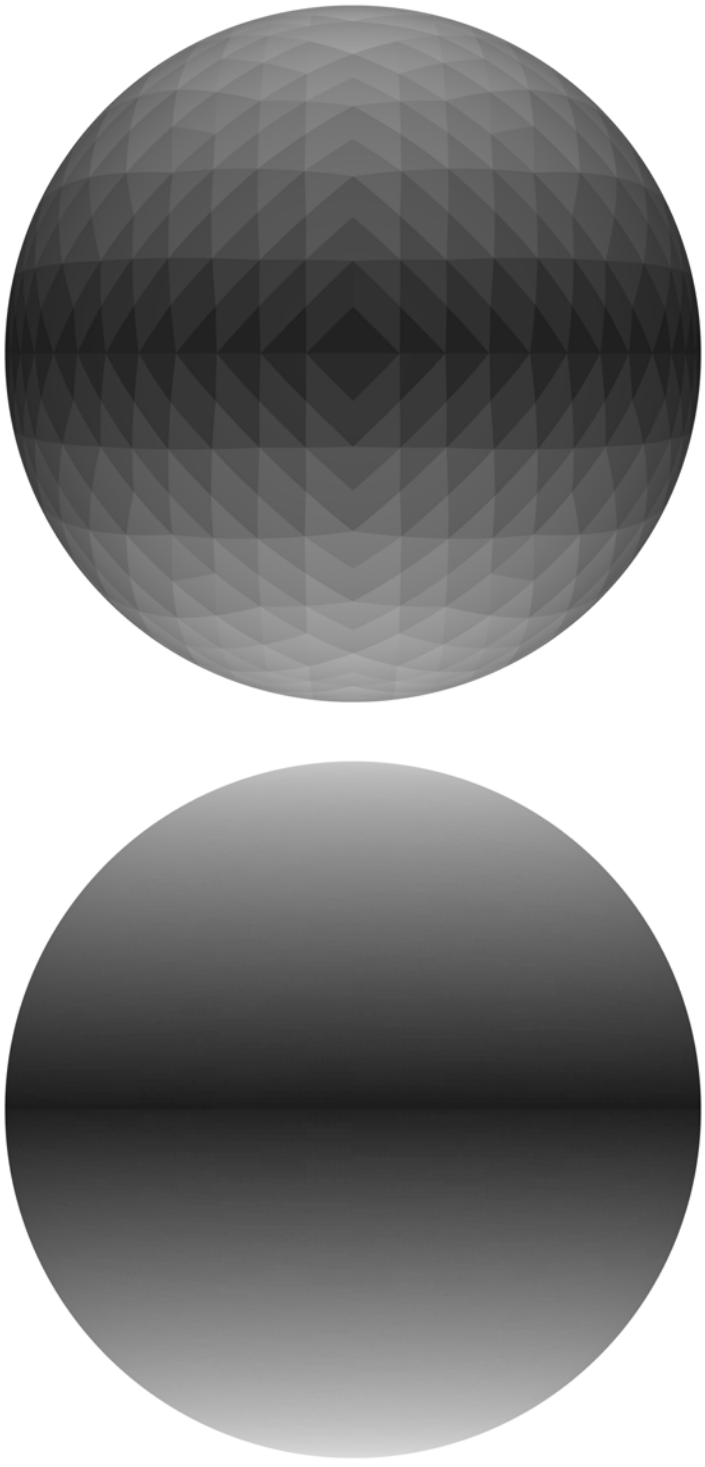

Figure 6.15: Reconstructed BRDF for the pseudo Haar wavelets for an approximation which retained 0.78% of the basis function coefficients of the full signal (top), and reconstruction with the full coefficient vector (bottom).

Figure 6.16: Reconstructed visibility map for the SOHO wavelet basis (top) and the Bio-Haar basis (bottom) for an approximation which retained 0.78% of the basis function coefficients of the full signal.

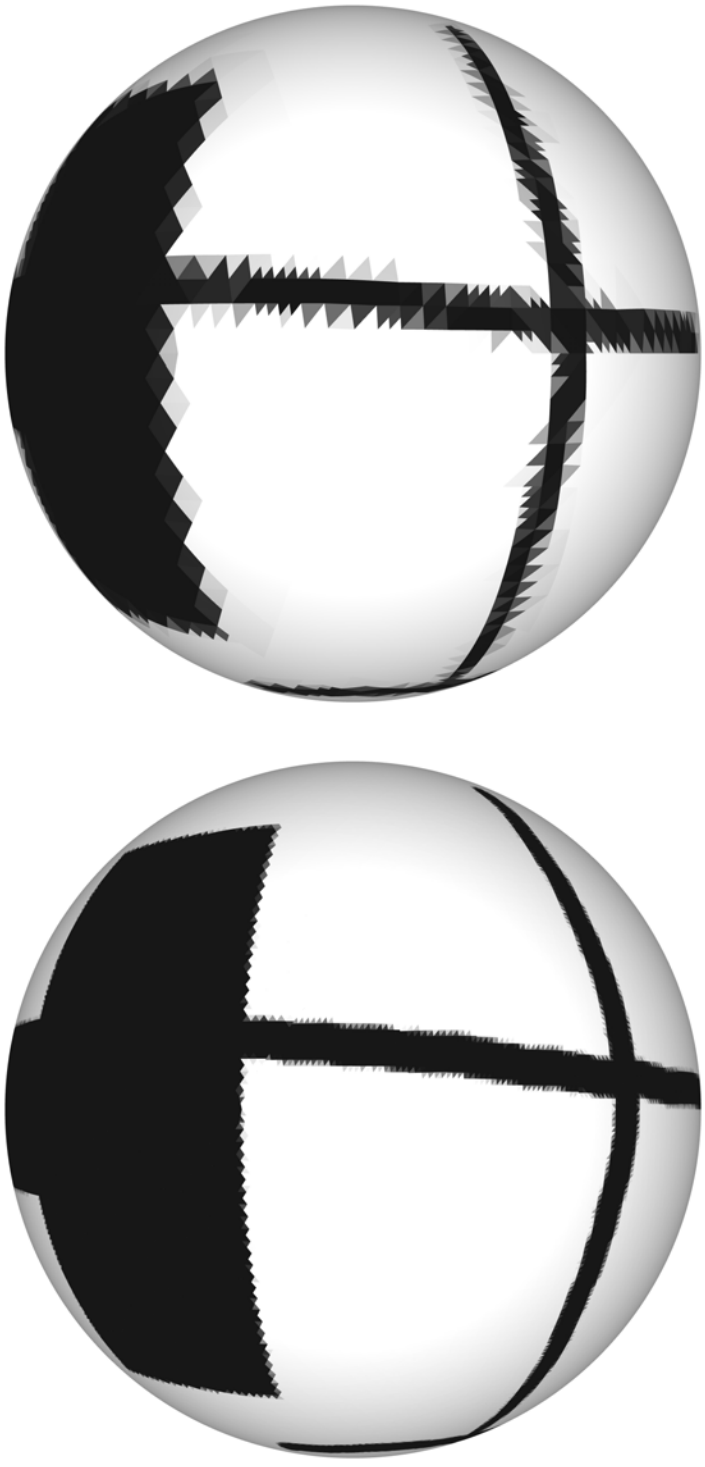

Figure 6.17: Reconstructed visibility map for the pseudo Haar wavelets for an approximation which retained 6.25% of the basis function coefficients of the full signal (top), and reconstruction with the full coefficient vector (bottom).

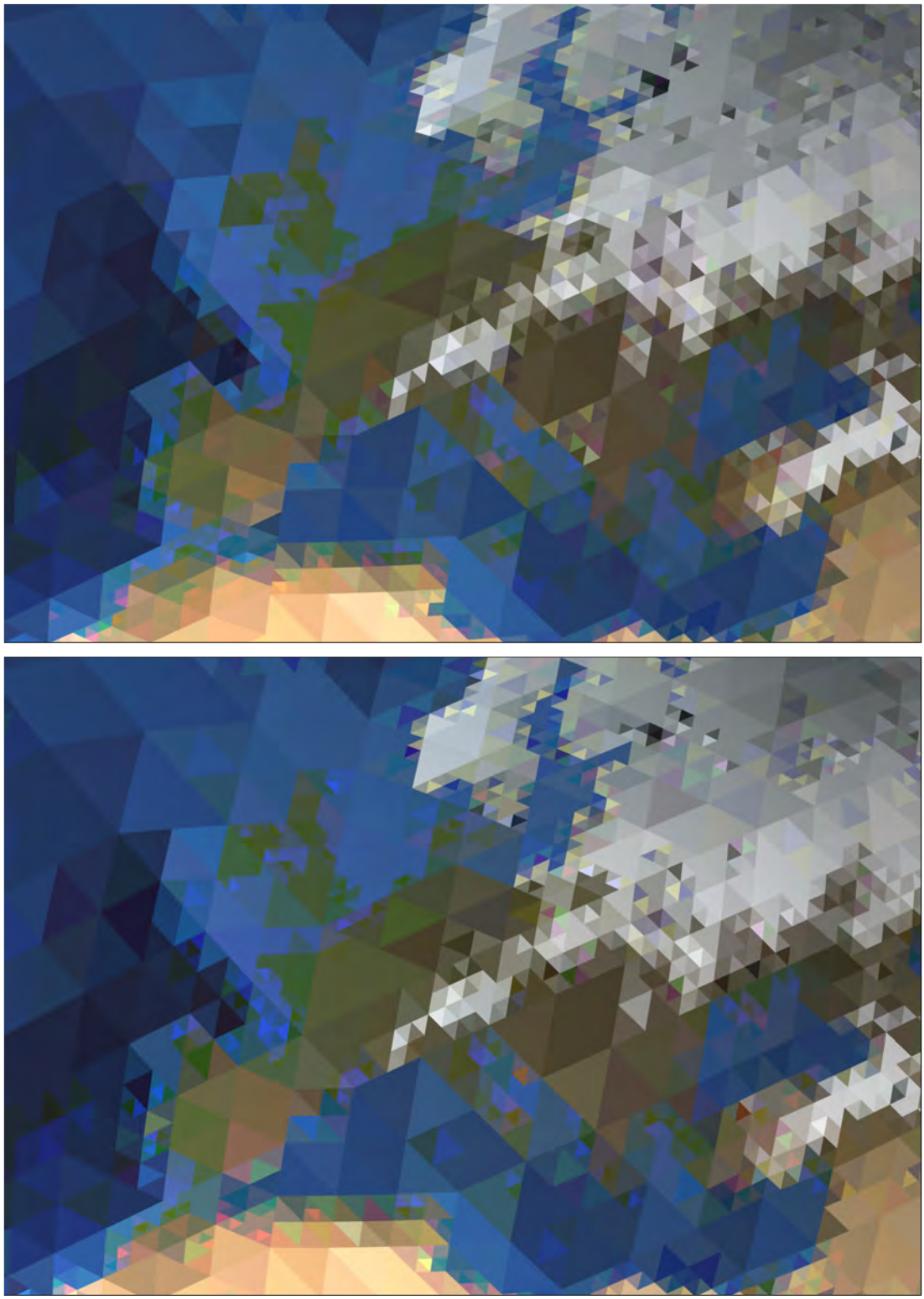

Figure 6.18: Detail of the reconstructed texture map for the SOHO wavelet basis (top) and the Bio-Haar basis (bottom) for an approximation which retained 6.25% of the basis function coefficients of the full signal.

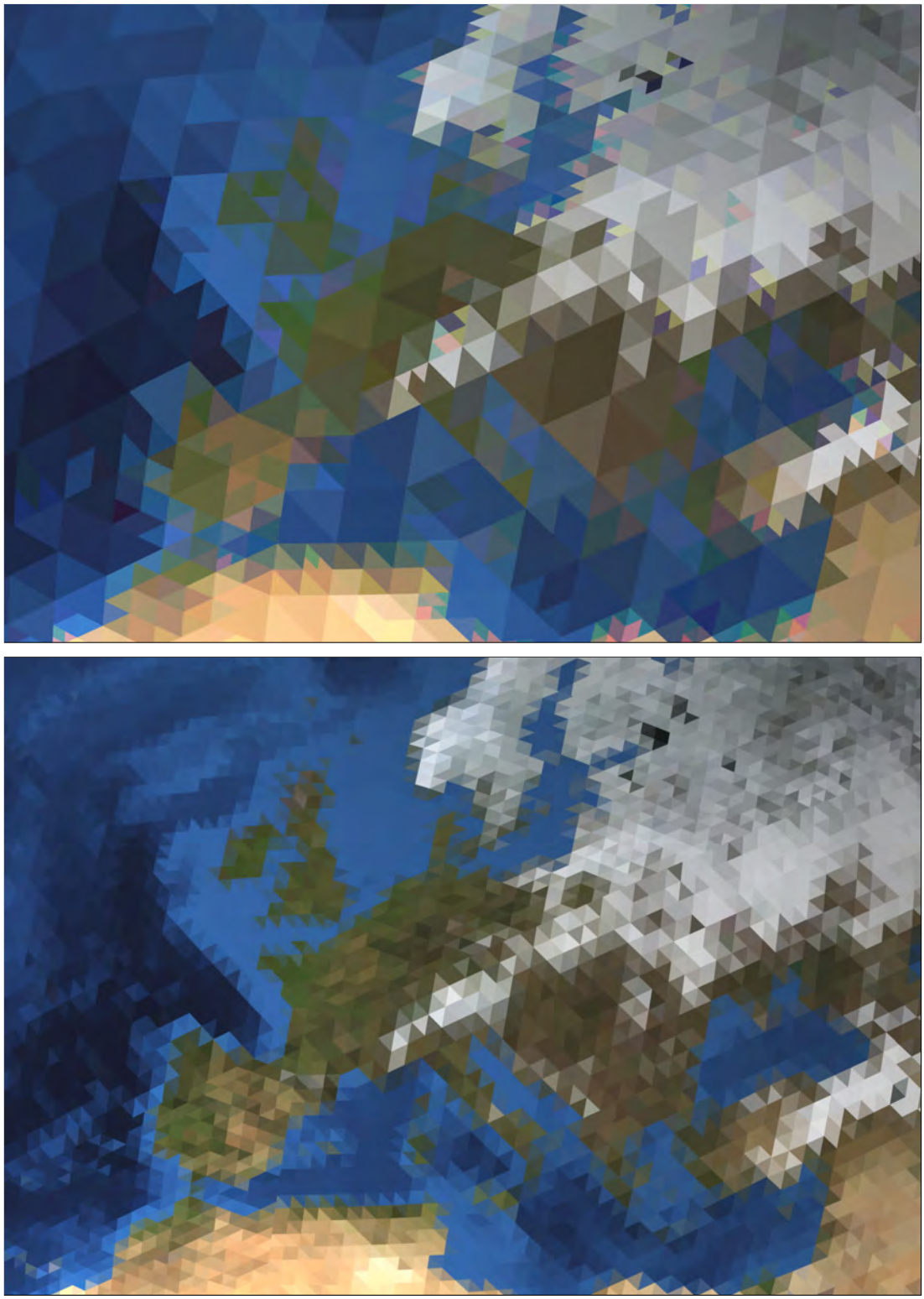

Figure 6.19: Detail of the reconstructed texture map for the pseudo Haar wavelets for an approximation which retained 6.25% of the basis function coefficients of the full signal.

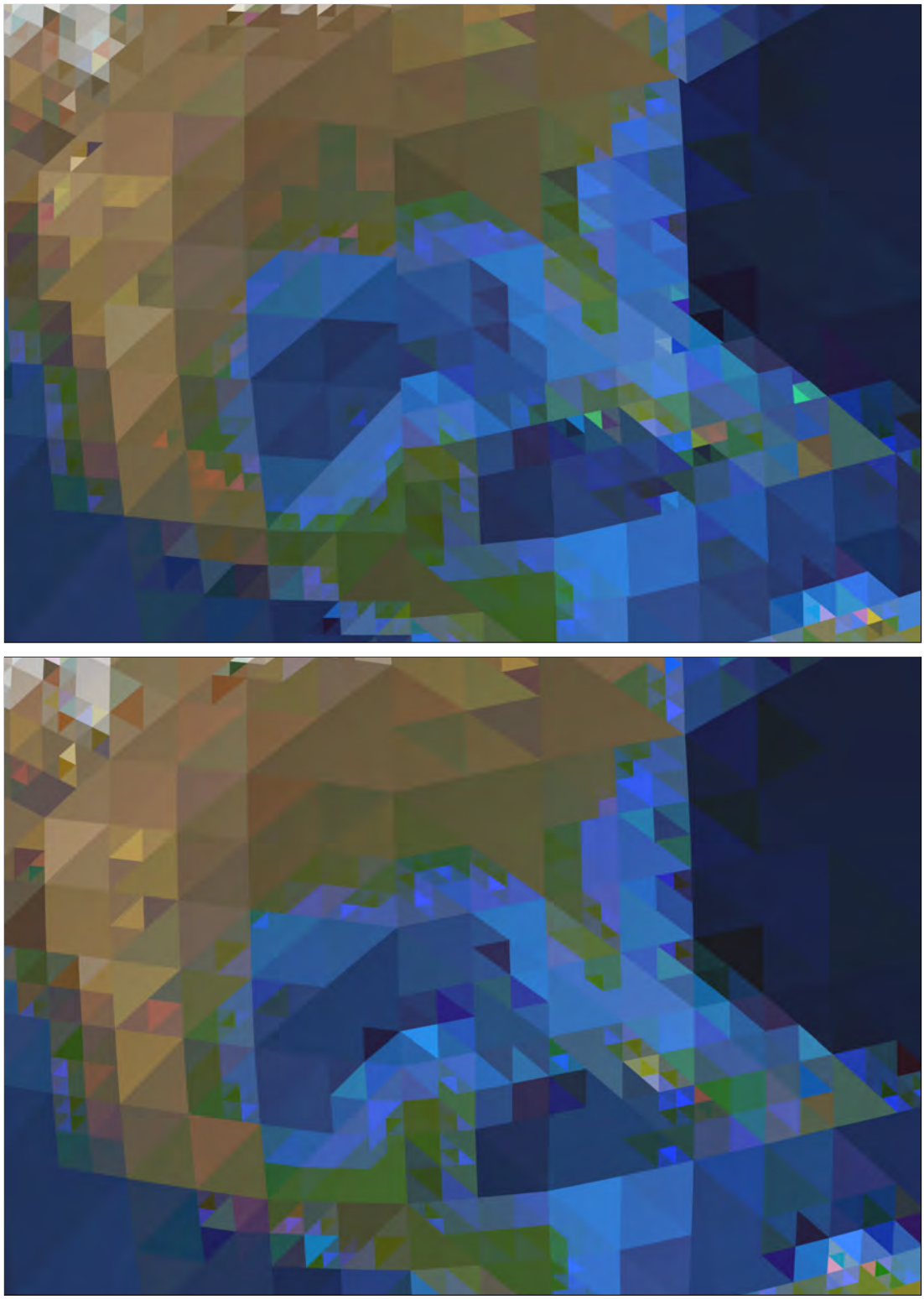

Figure 6.20: Detail of the reconstructed texture map for the SOHO wavelet basis (top) and the Bio-Haar basis (bottom) for an approximation which retained 6.25% of the basis function coefficients of the full signal.

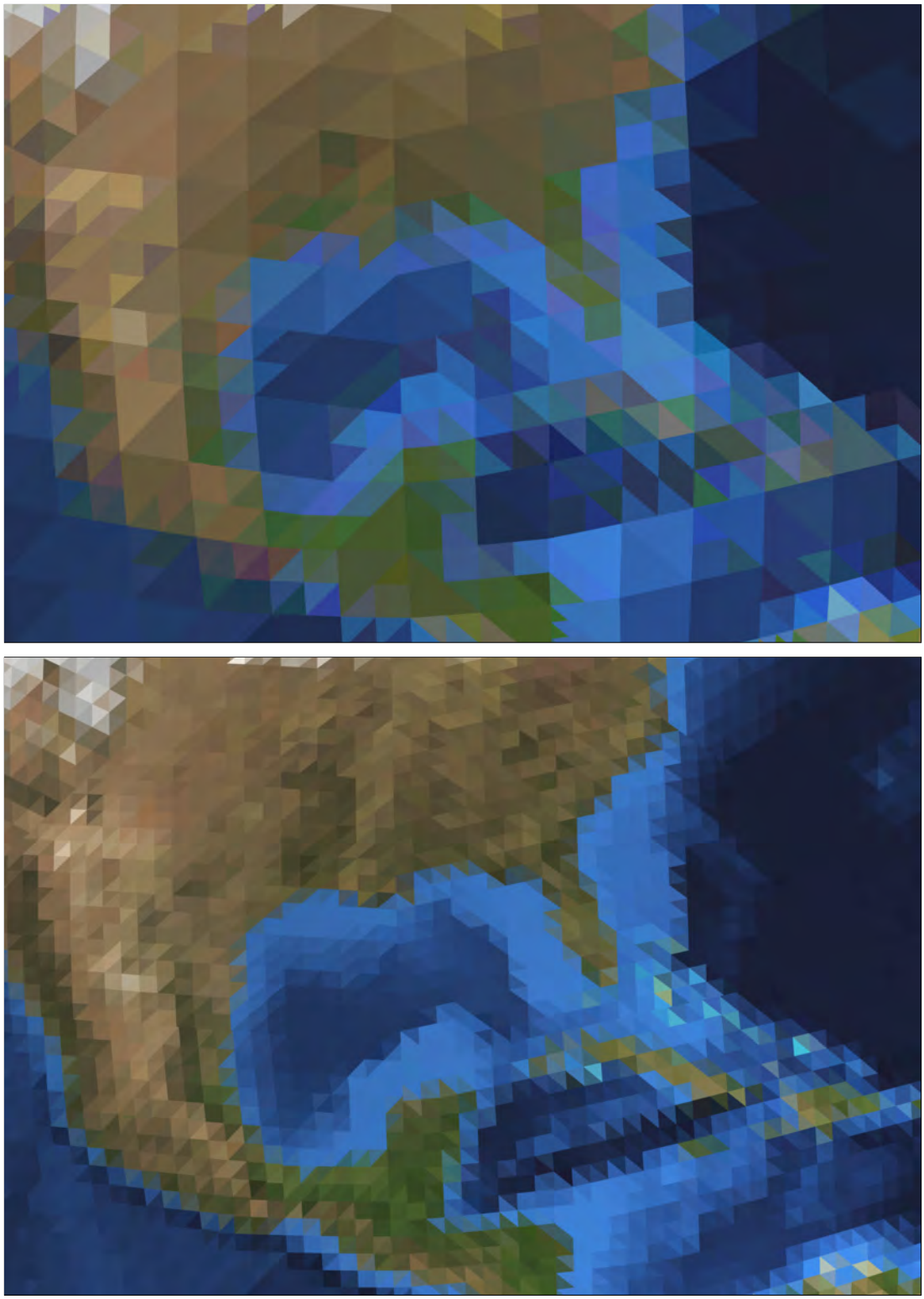

Figure 6.21: Detail of the reconstructed texture map for the pseudo Haar wavelets for an approximation which retained 6.25% of the basis function coefficients of the full signal.

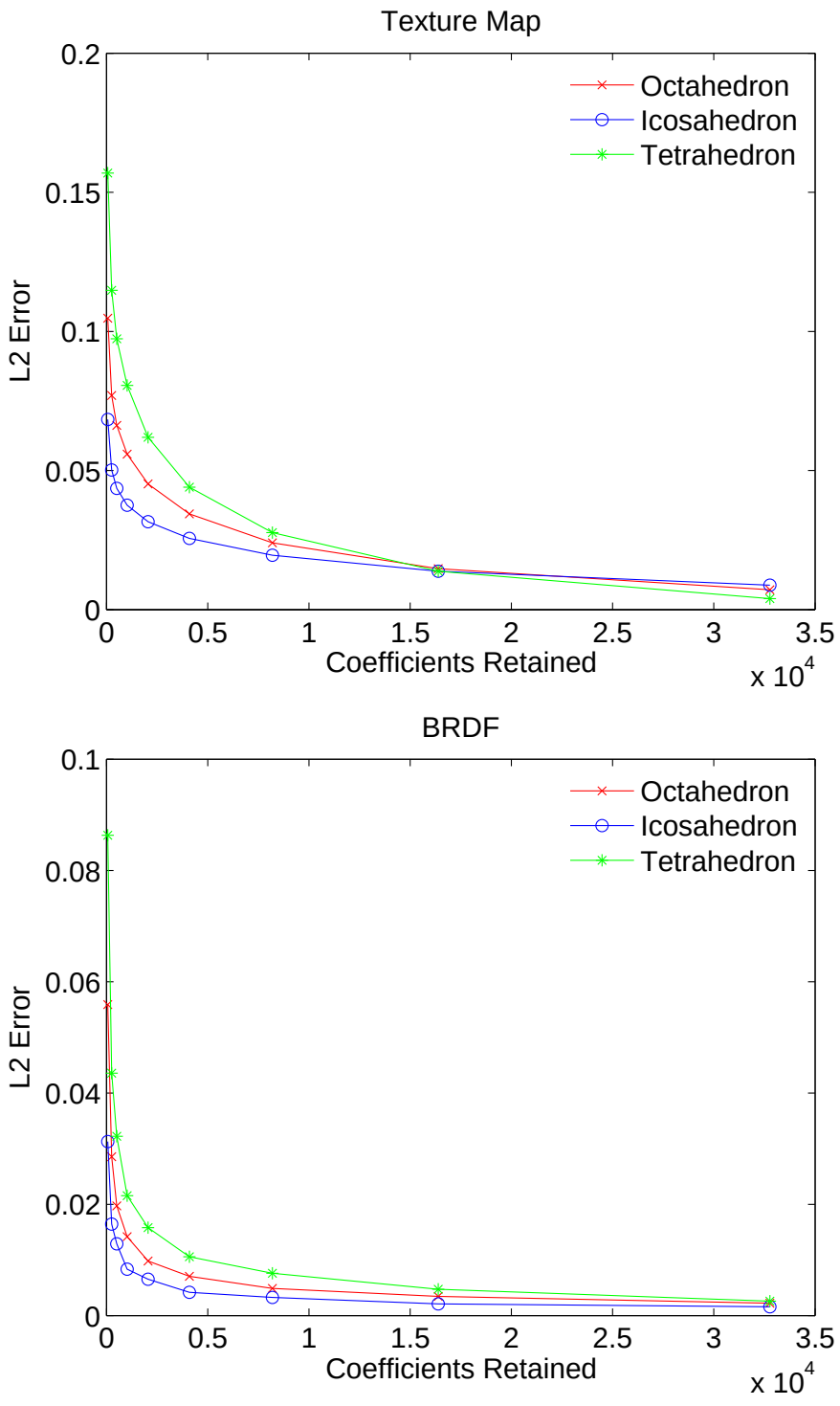

Figure 6.22: Approximation performance of SOHO wavelet bases defined over partitions derived from different base polyhedron. The graphs show the error in the ℓ_2 norm for the texture map (top) and the BRDF (bottom).

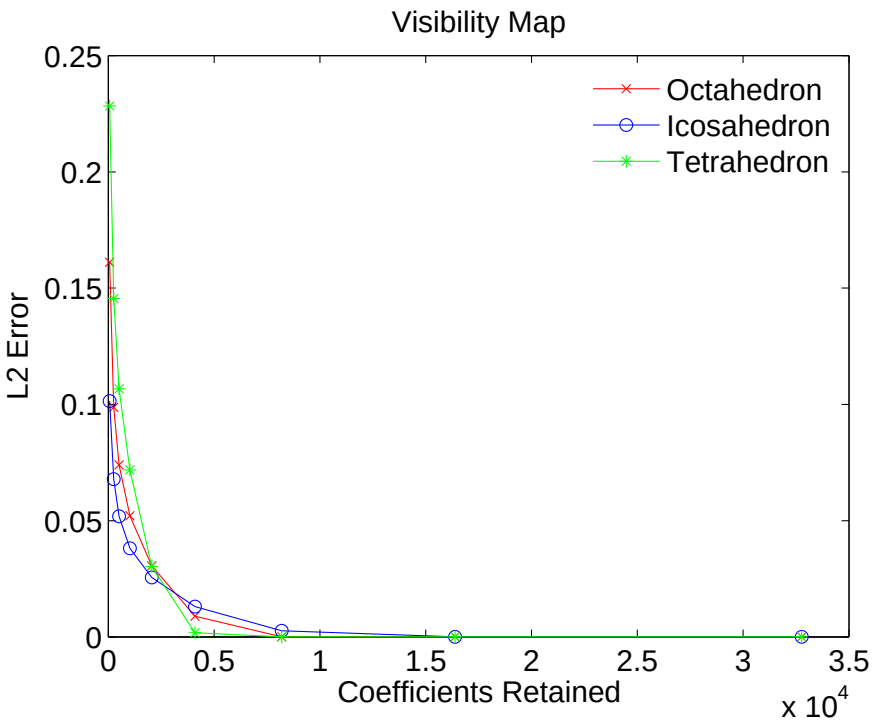

Figure 6.23: Approximation performance of SOHO wavelet bases defined over partitions derived from different platonic solids. The graphs show the ℓ_2 error for the visibility map.

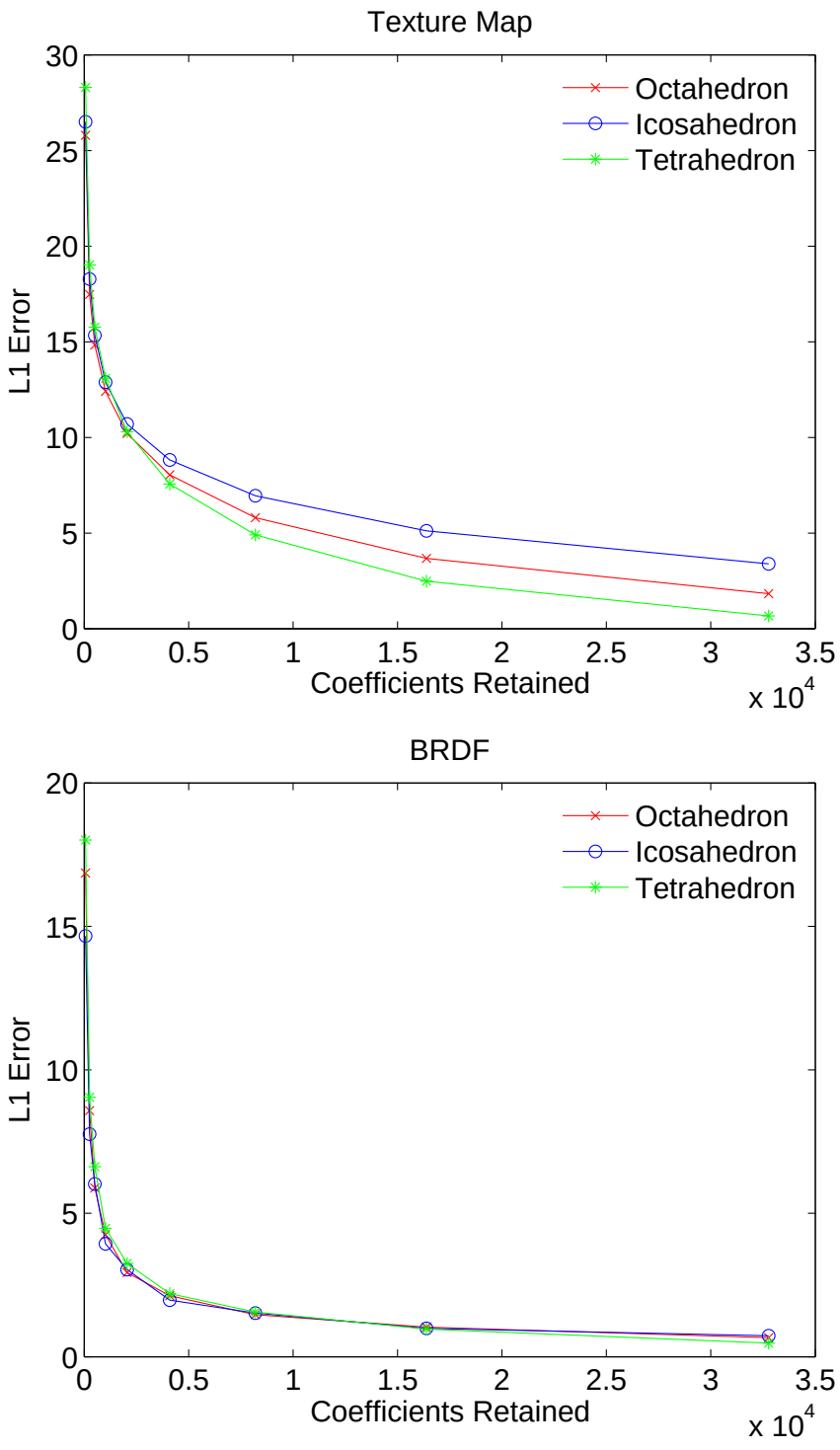

Figure 6.24: Approximation performance of SOHO wavelet bases defined over partitions derived from different platonic solids. The graphs show the ℓ_1 error for the texture map (top) and the BRDF (bottom).

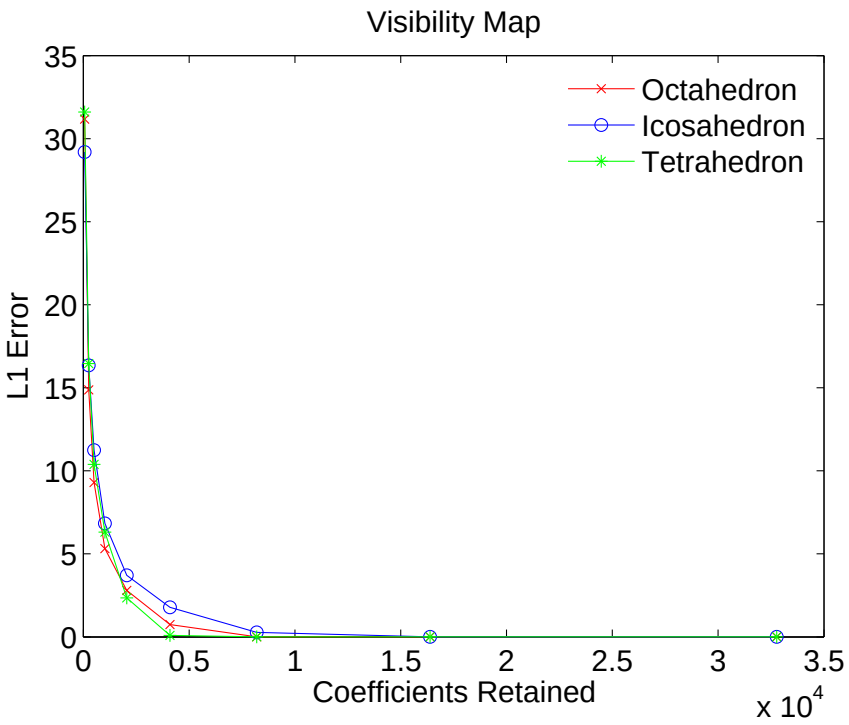

Figure 6.25: Approximation performance of SOHO wavelet bases defined over partitions derived from different platonic solids. The graphs show the ℓ_1 error for the visibility map.

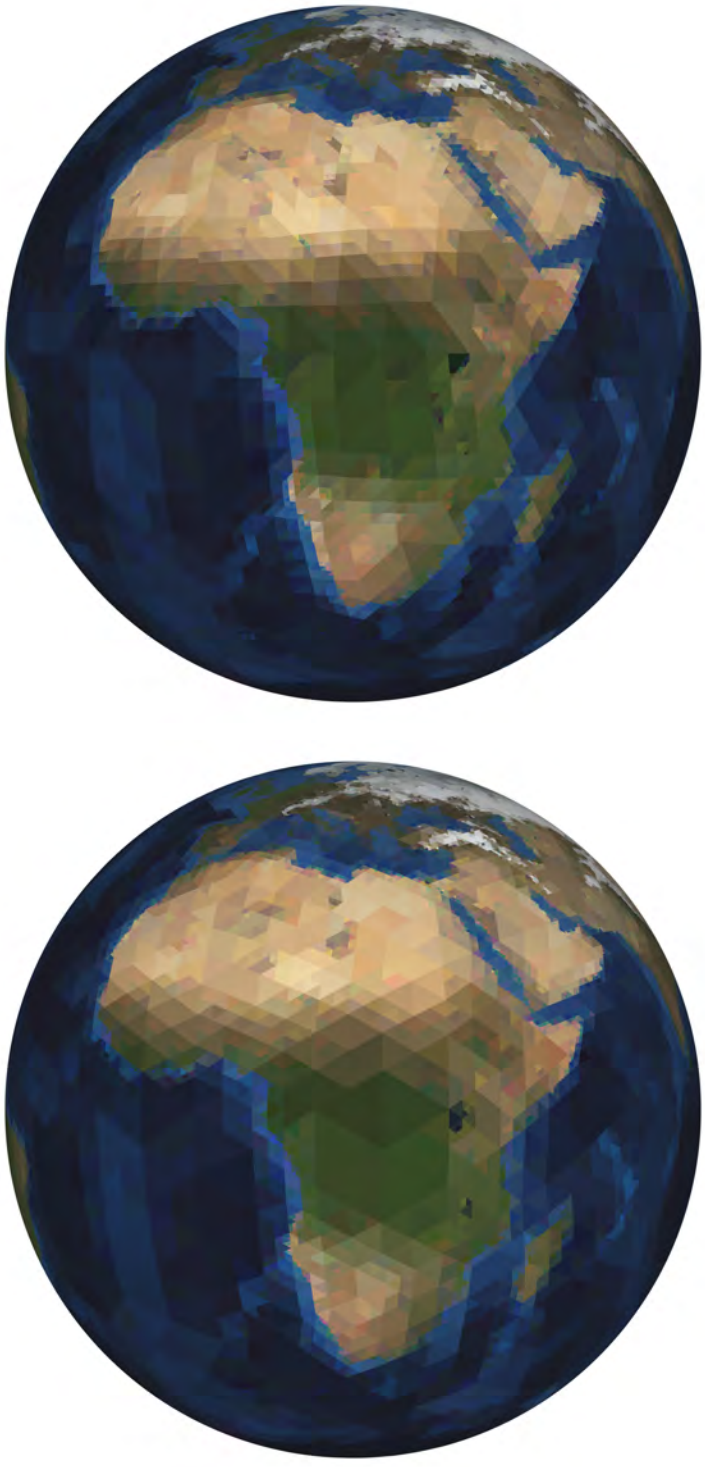

Figure 6.26: Reconstructed texture map for SOHO wavelet bases defined over partitions derived from an octahedron (top) and an icosahedron (bottom). For the reconstruction 6.25% of the coefficients of the full signal have been retained.

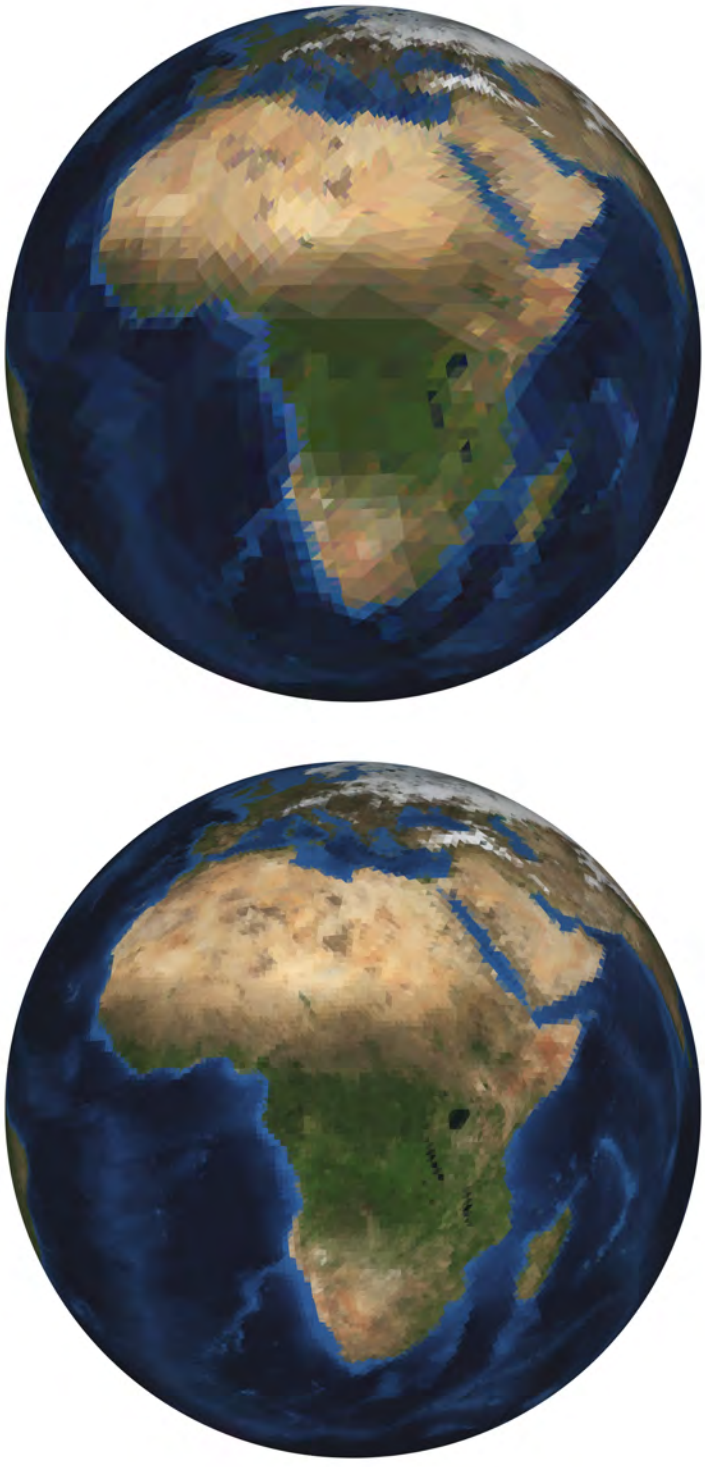

Figure 6.27: Reconstructed texture map for a SOHO wavelet basis defined over partitions derived from an tetrahedron (top). For the reconstruction 6.25% of the coefficients of the full signal have been retained. The signal at the bottom has been obtained with the full coefficient vector and a partition derived from an octahedron.

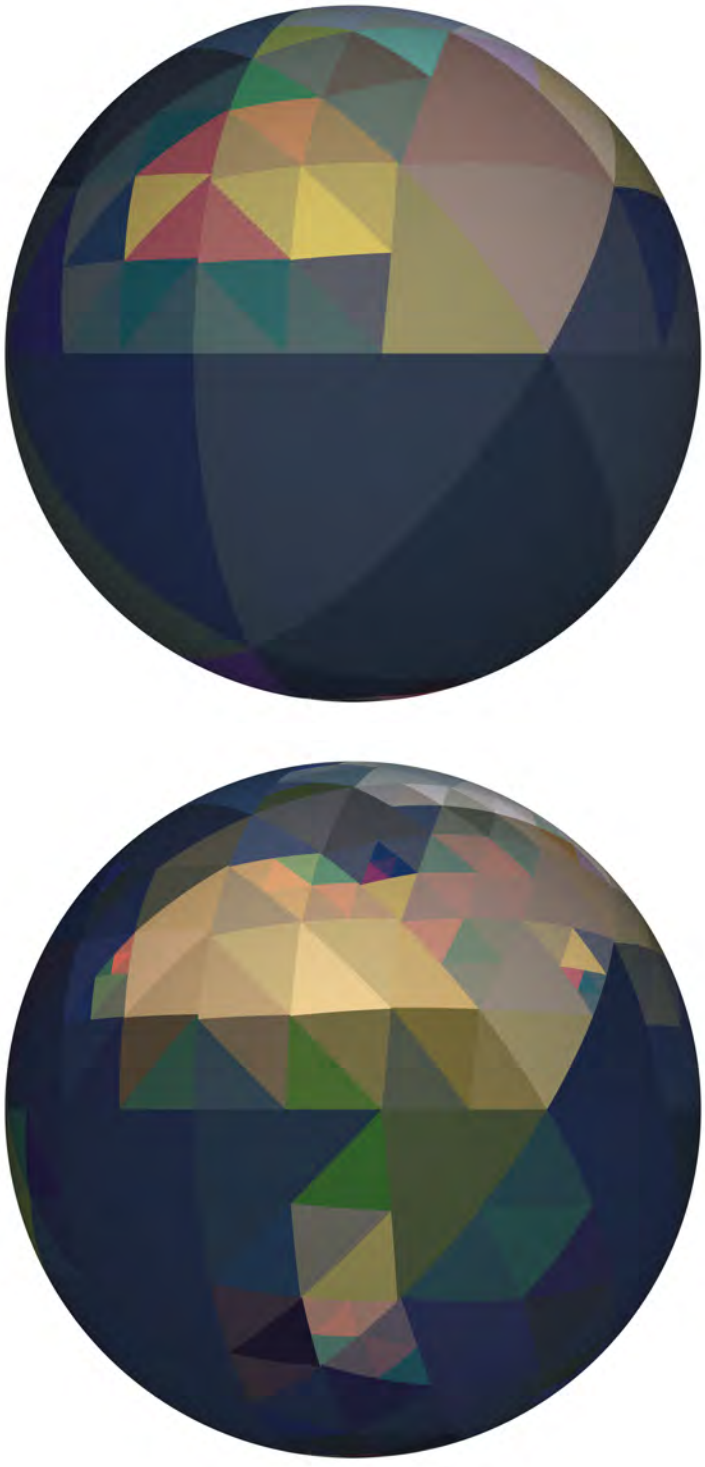

Figure 6.28: Reconstructed texture map for the SOHO wavelet basis with 64 (top) and 256 (bottom) nonzero coefficients.

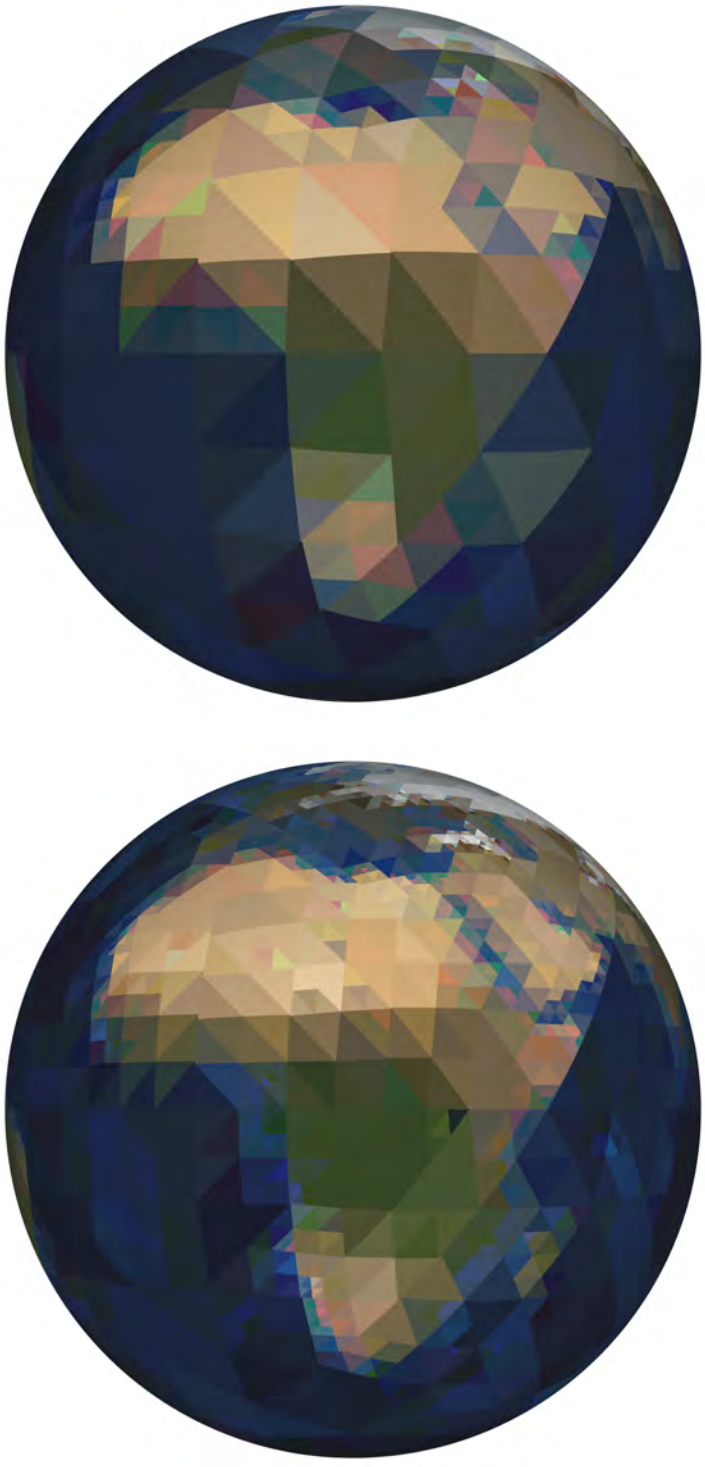

Figure 6.29: Reconstructed texture map for the SOHO wavelet basis with 512 (top) and $2,056$ (bottom) nonzero coefficients.

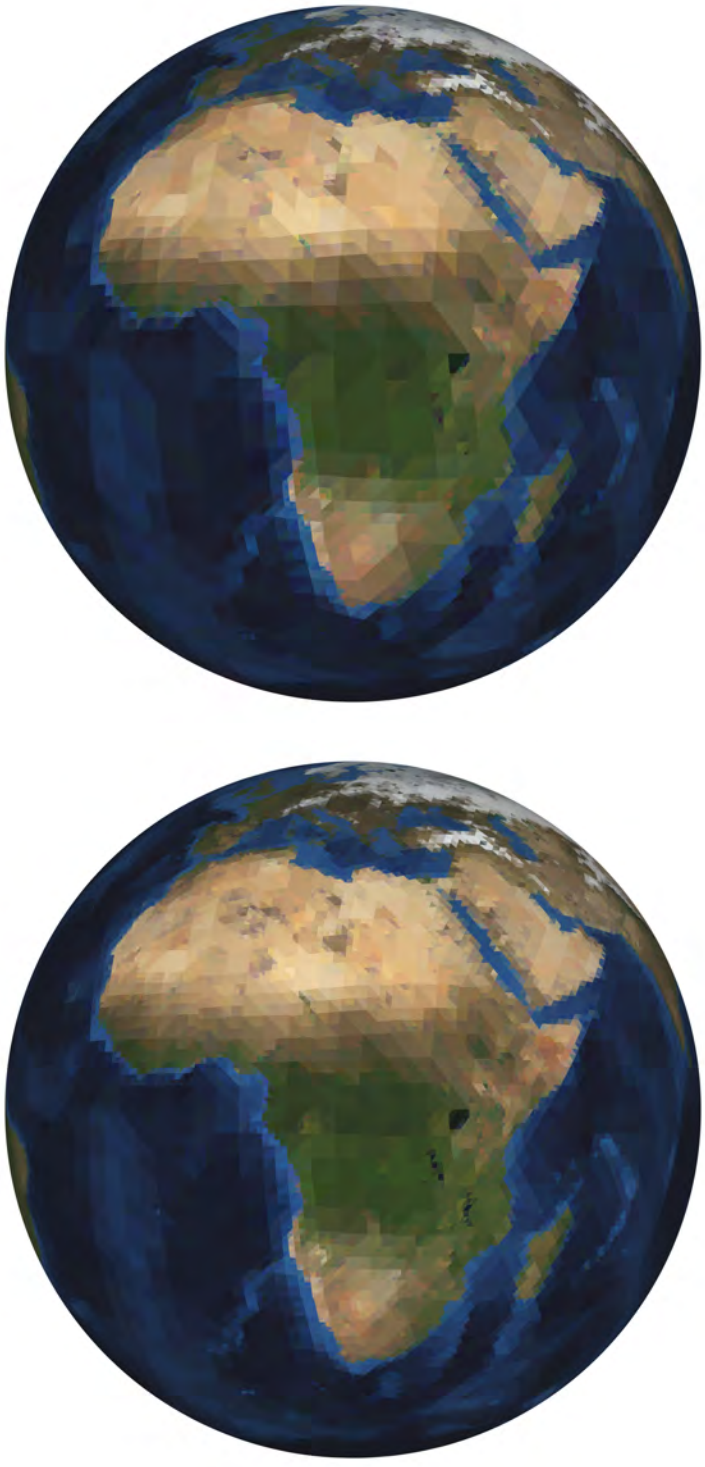

Figure 6.30: Reconstructed texture map for the SOHO wavelet basis with $8,192$ (top) and $16,384$ (bottom) nonzero coefficients.

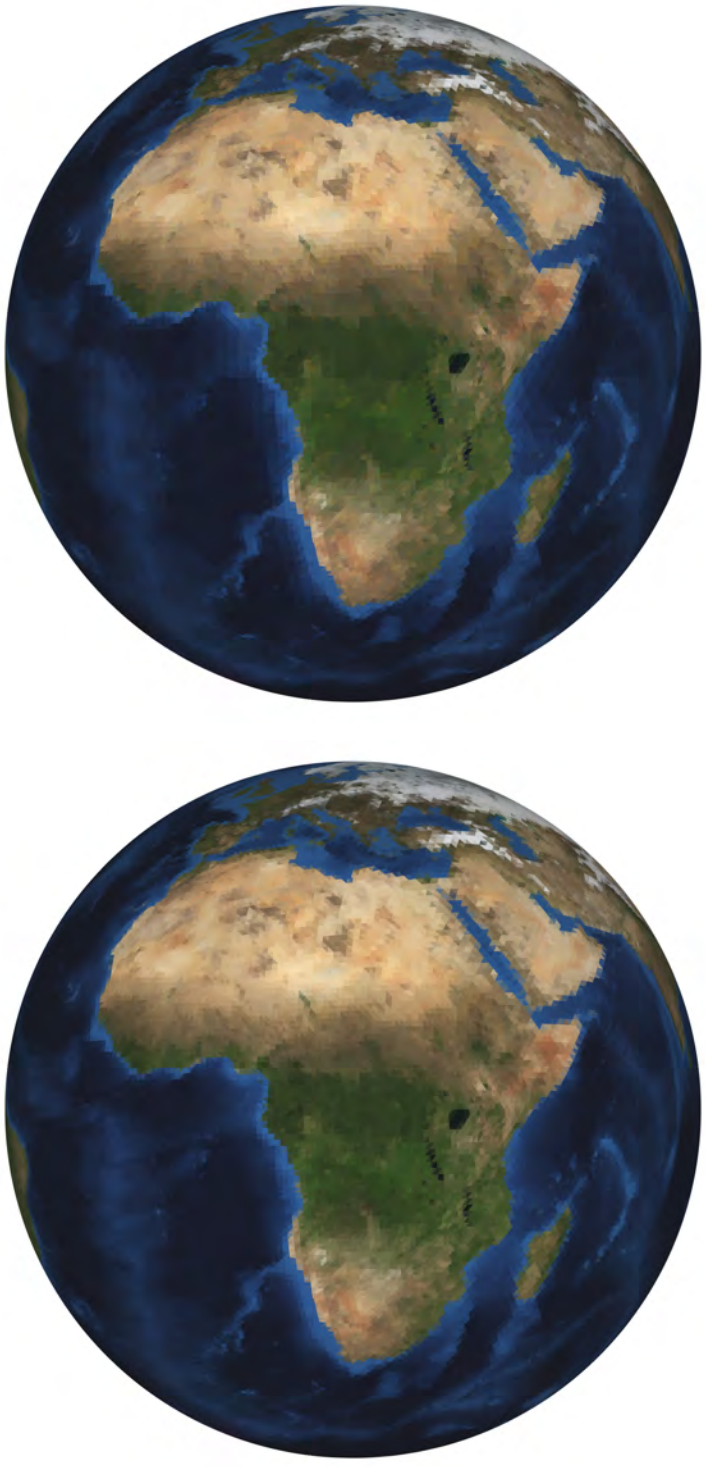

Figure 6.31: Reconstructed texture map for the SOHO wavelet basis with $32,768$ nonzero coefficients (top) and the full coefficient vector (bottom).

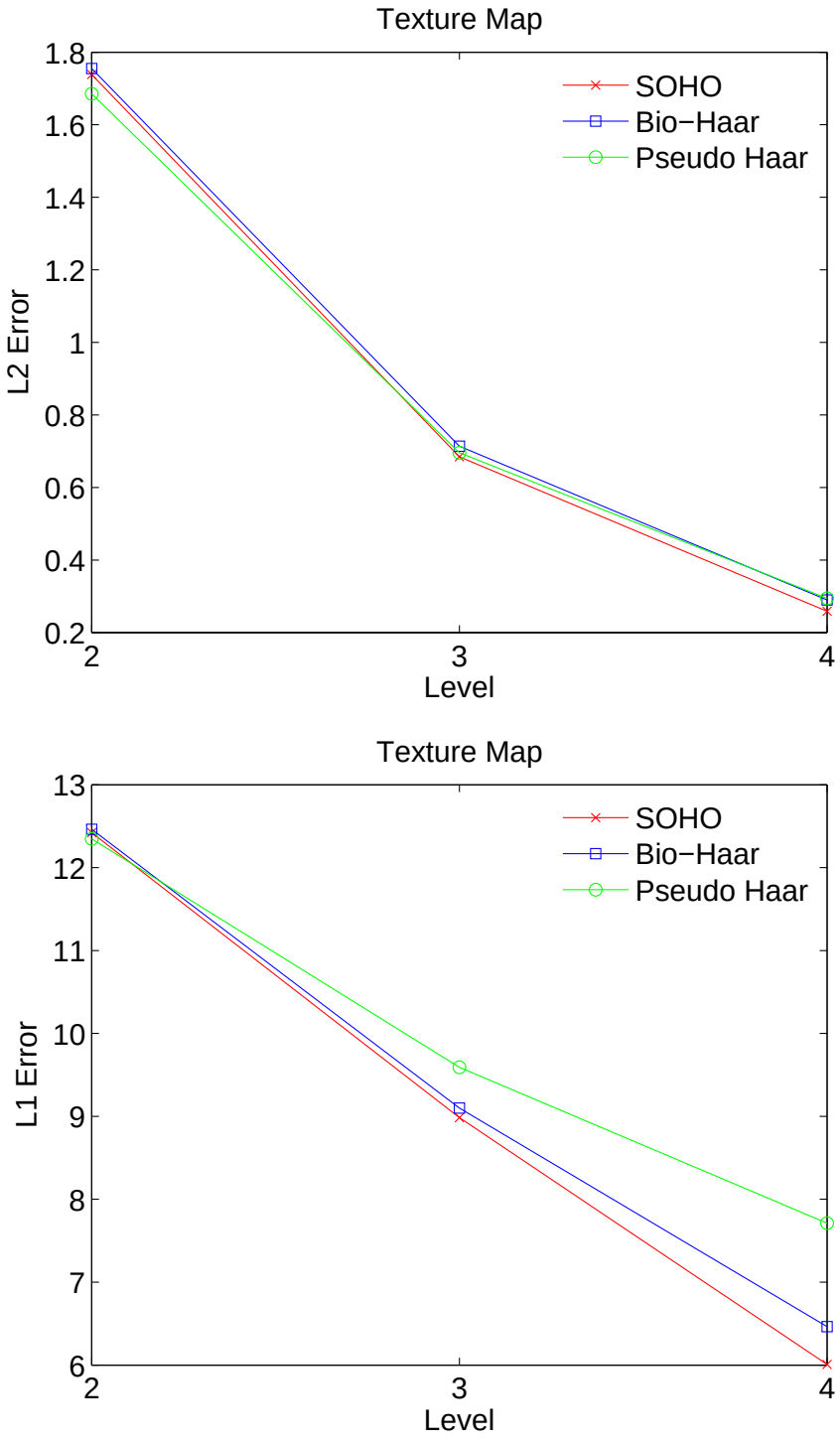

Figure 6.32: Performance of spherical Haar wavelet bases for the rotation of the texture map in its wavelet basis representation.

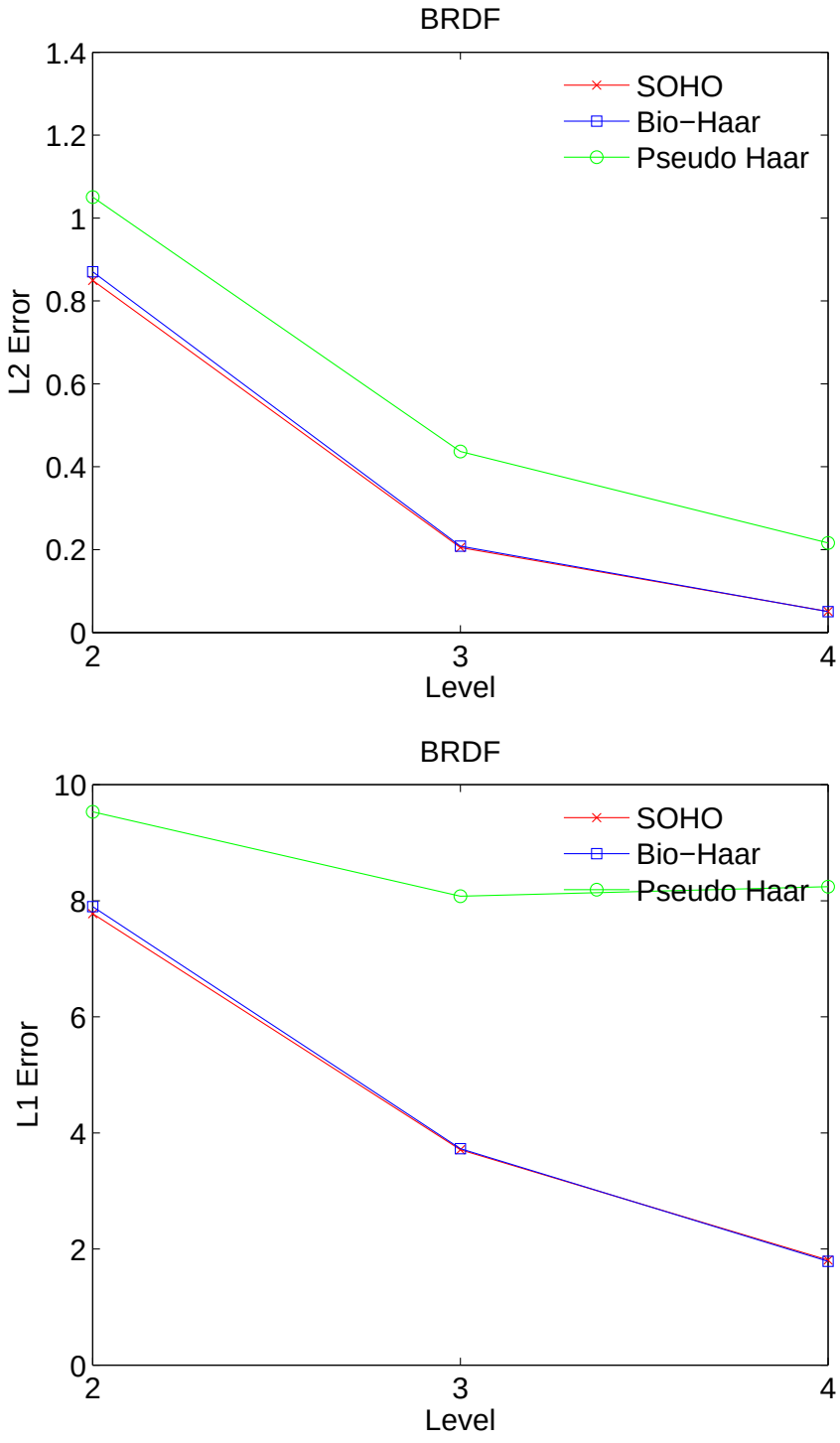

Figure 6.33: Performance of spherical Haar wavelet bases for the rotation of the BRDF in its wavelet basis representation.

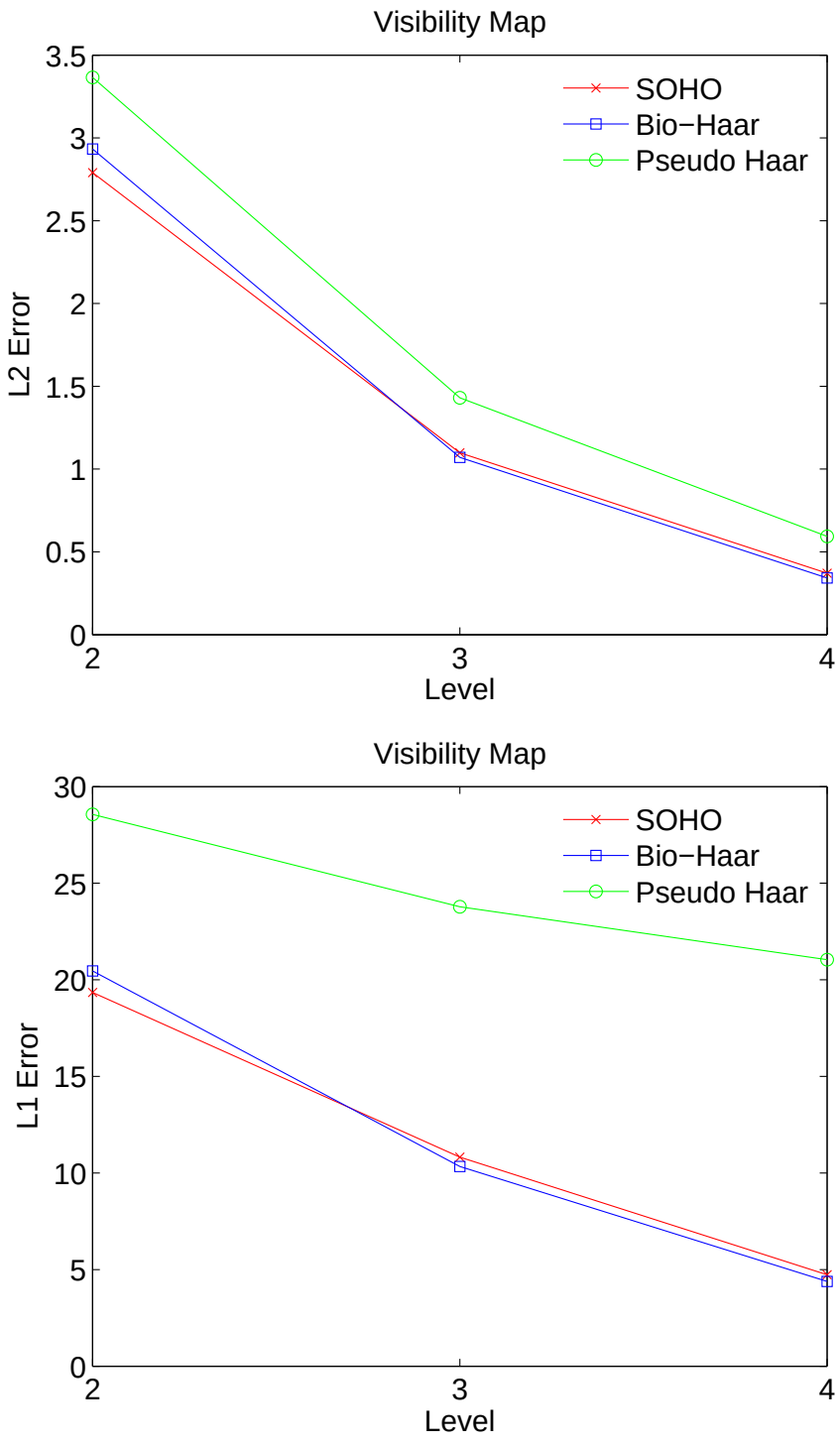

Figure 6.34: Performance of spherical Haar wavelet bases for the rotation of the visibility map in its wavelet basis representation.

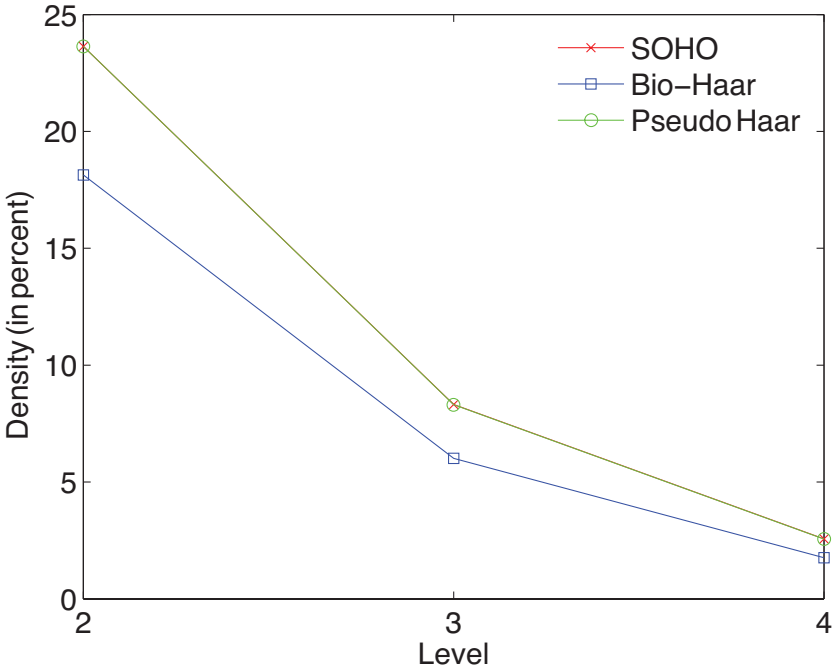

Figure 6.35: Sparsity of rotation matrices. Note that some graphs almost coincide and are therefore not clearly visible.

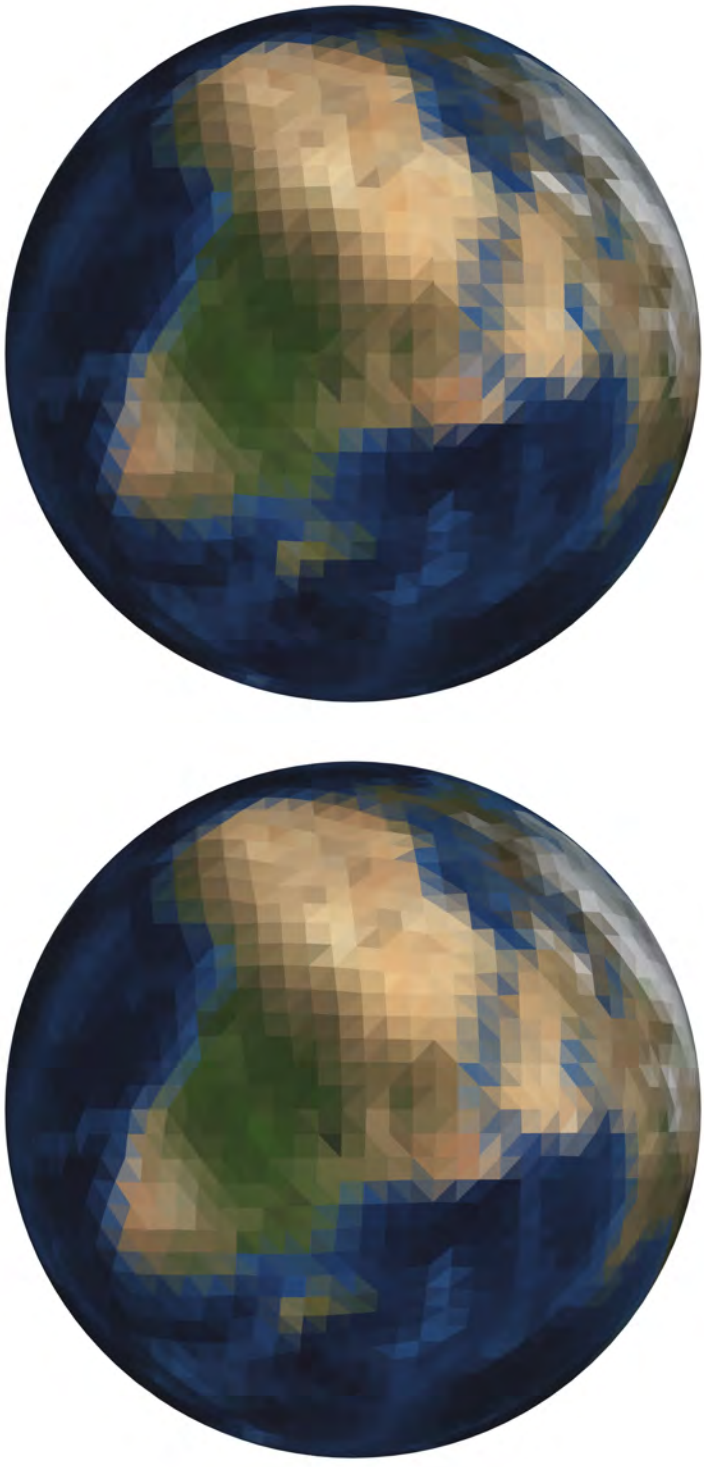

Figure 6.36: Reconstructed signals in the target basis after rotation for the SOHO wavelet basis (top) and the Bio-Haar basis (bottom).

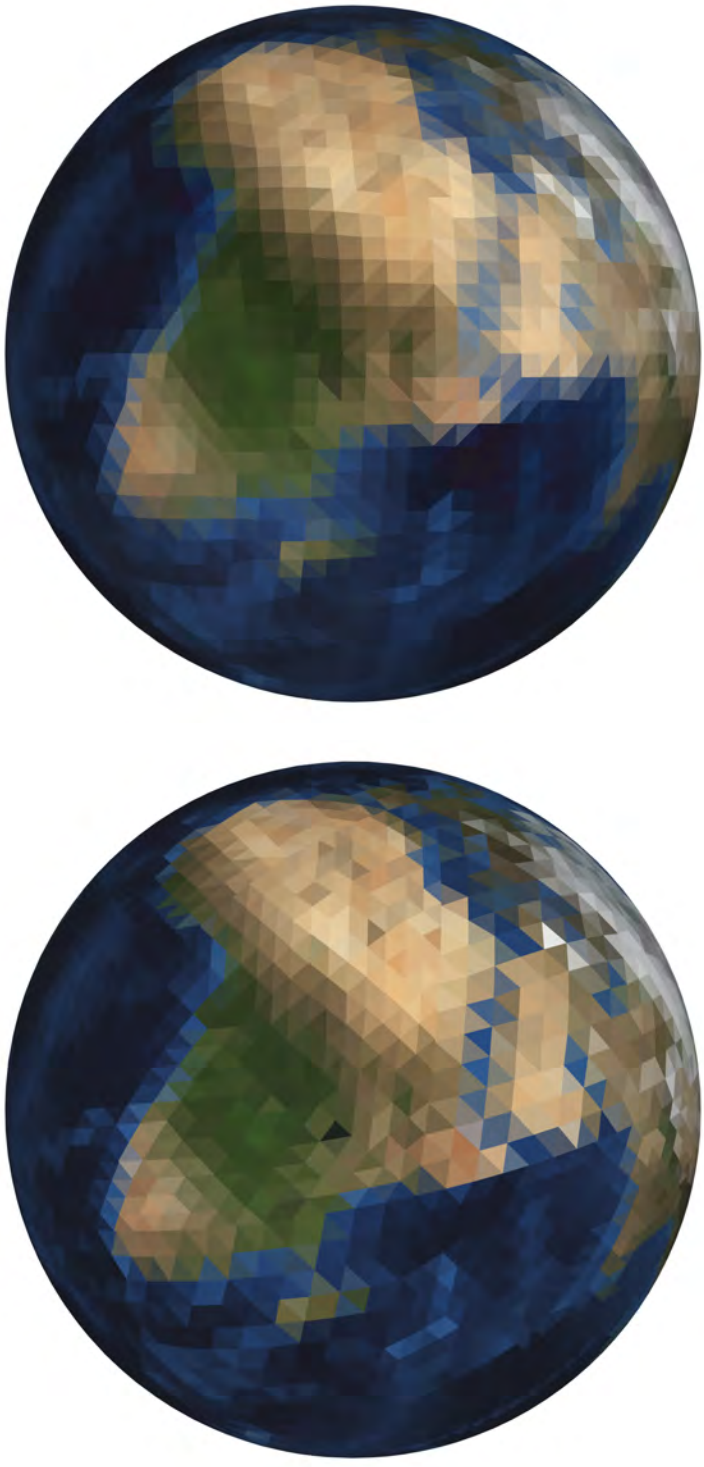

Figure 6.37: Reconstructed signals in the target basis after rotation for the pseudo Haar wavelets (top). In the bottom picture the rotated signal in the source basis is shown.

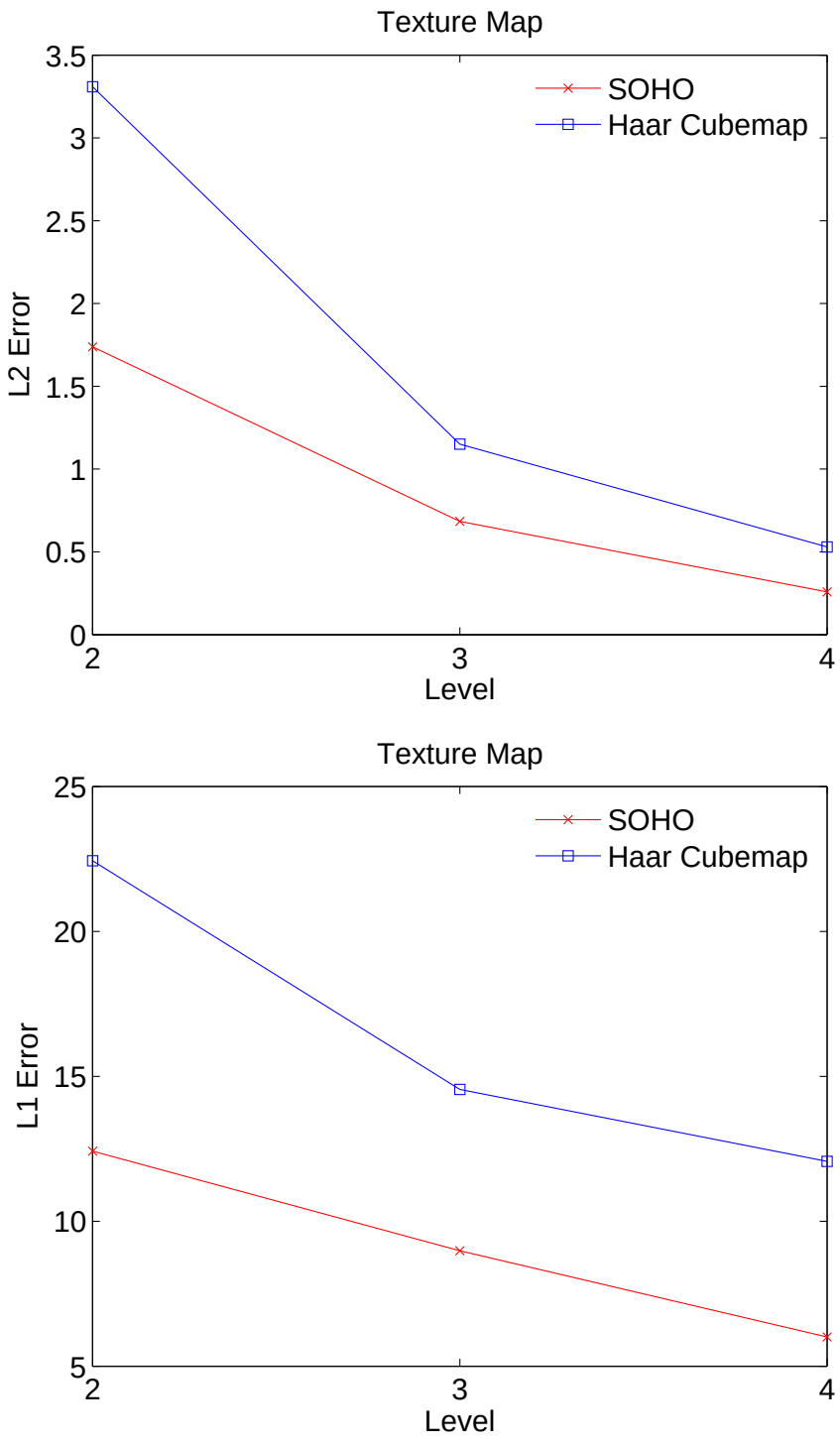

Figure 6.38: Performance of the SOHO wavelet basis and the Haar cubemap basis for the rotation of the texture map in its wavelet basis representation.

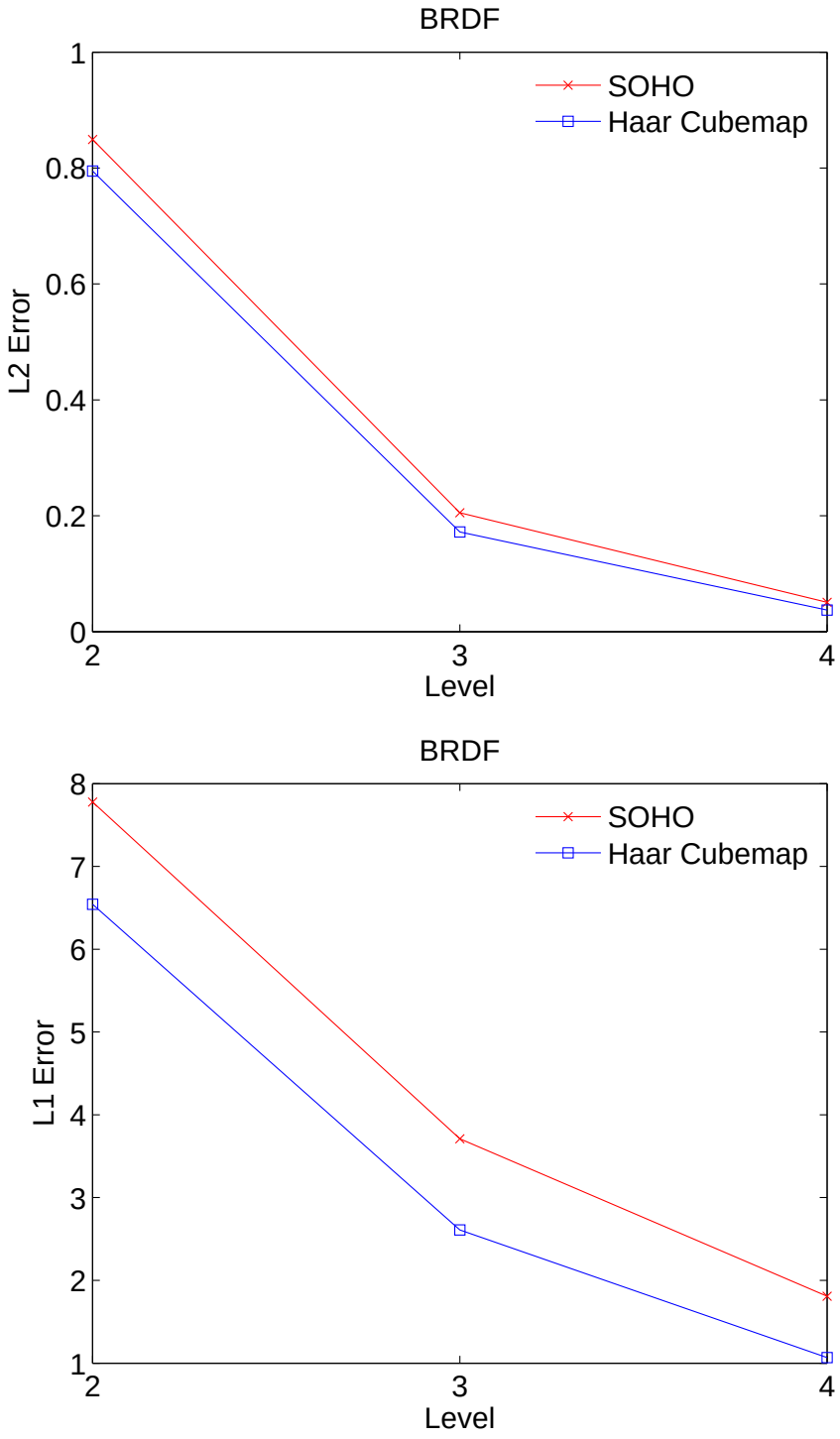

Figure 6.39: Performance of the SOHO wavelet basis and the Haar cubemap basis for the rotation of the BRDF in its wavelet basis representation.

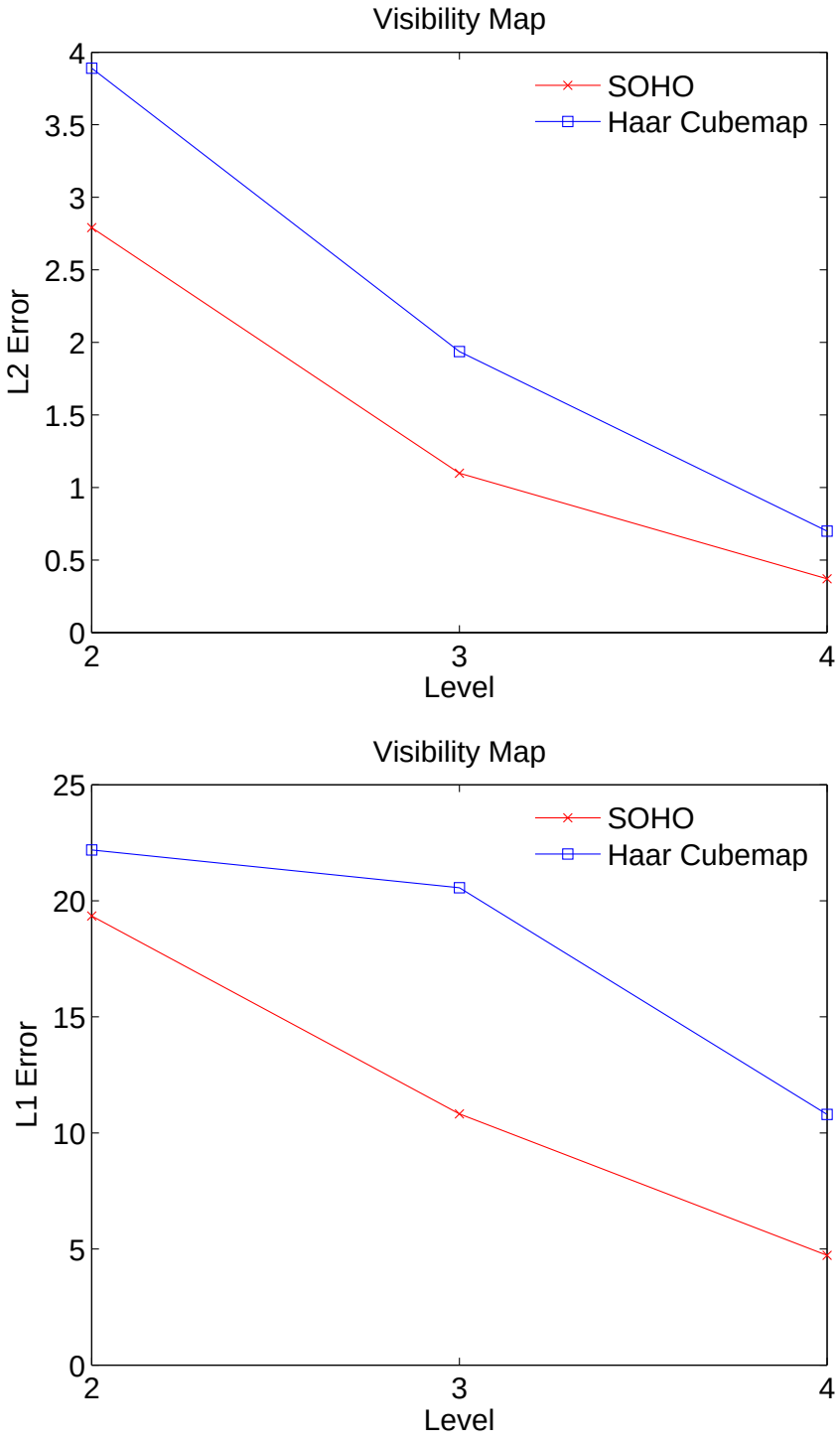

Figure 6.40: Performance of the SOHO wavelet basis and the Haar cubemap basis for the rotation of the visibility map in its wavelet basis representation.

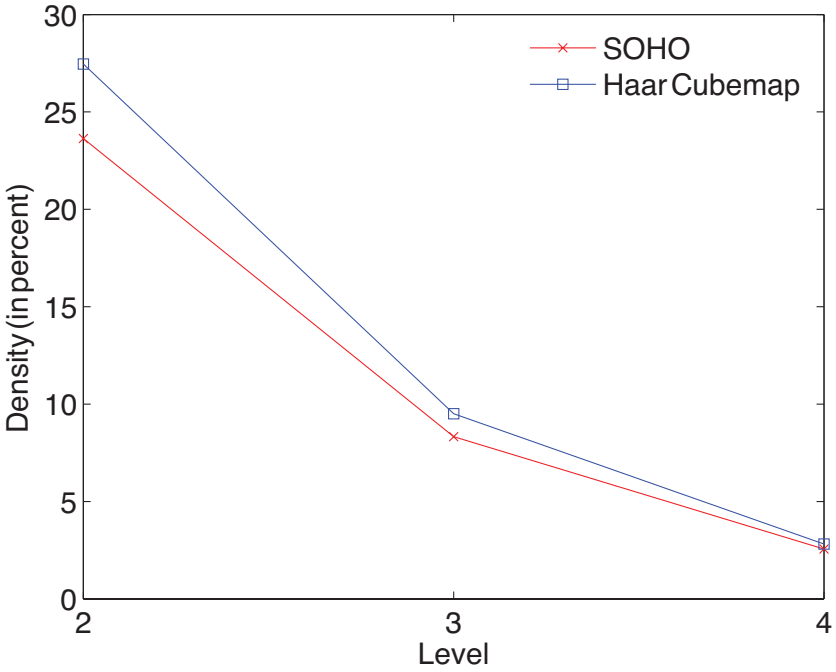

Figure 6.41: Sparsity of rotation matrices.

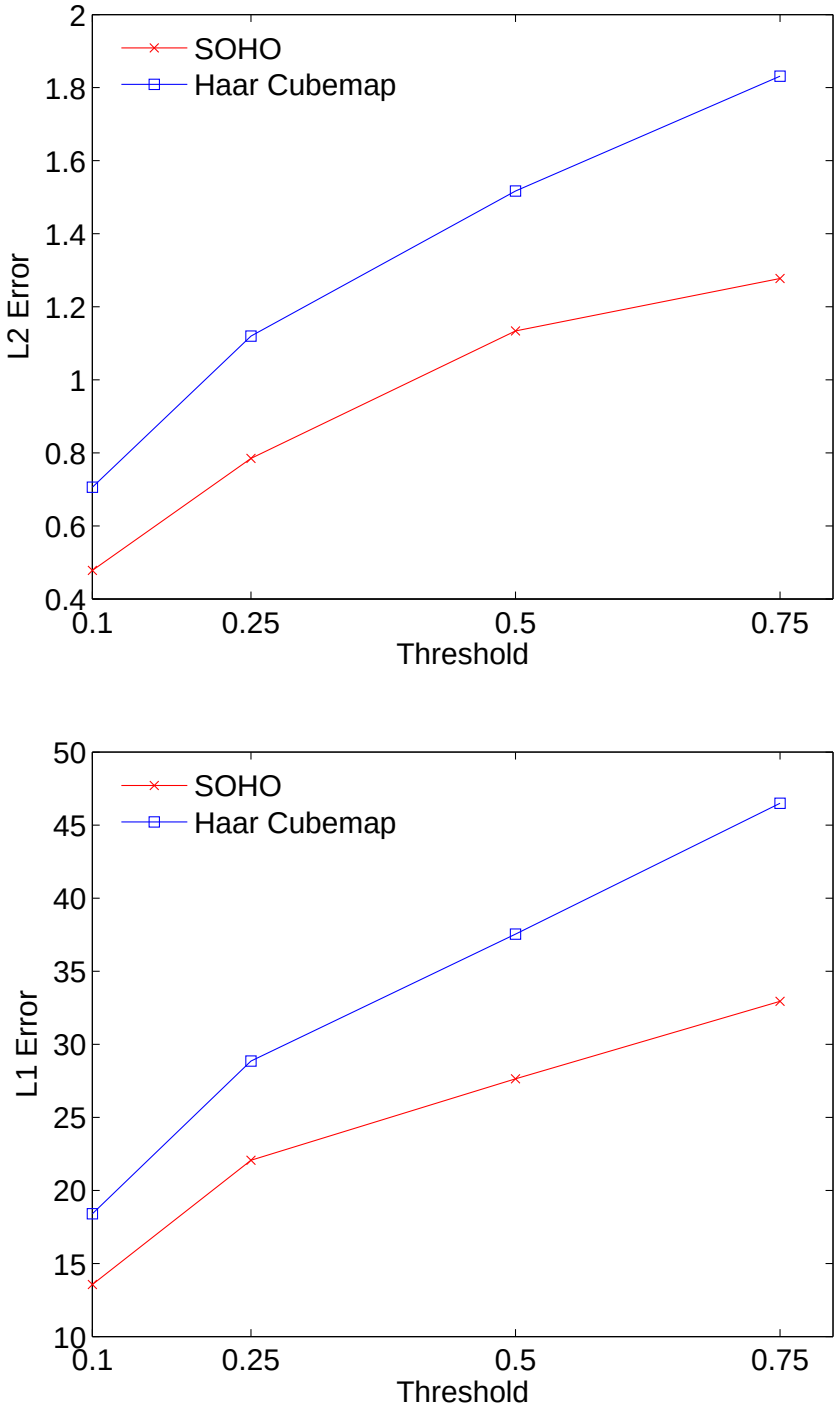

Figure 6.42: Performance of the SOHO wavelet basis and the Haar cubemap basis for the rotation of the texture map in its wavelet basis representation with approximated rotation matrices. The plots for other signals are similar and therefore omitted.

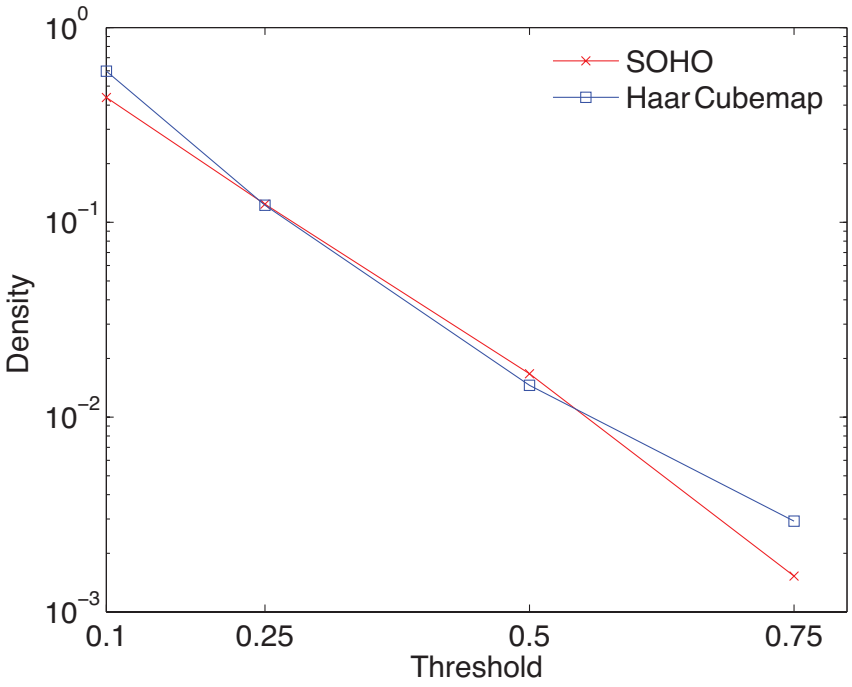

Figure 6.43: Sparsity of the rotation matrices for different approximation ratios.

Chapter 7

Future Work

The work presented in this thesis can be continued in a variety of directions.

Firstly, it would be interesting to answer the questions which had to remain unresolved in this thesis. What are sufficient conditions for the existence of an orthogonal and symmetric spherical Haar wavelet basis is one of the remaining problems. In our construction an area constraint has been employed, but it is at the moment unclear if any constraint at all is necessary to obtain a SOHO-like basis, or if alternative constraints exist. If the shape distortion of the novel subdivision scheme introduced in Chapter 4.4 is bounded is a second question which has yet to be answered.

We believe that many applications might benefit from the use of the SOHO wavelet basis. In computer graphics, for example the solution of the rendering equation [40] is likely to be more efficient with a representation of the light transport factors of the integral equation in the SOHO wavelet basis. The factors are usually not aligned and have to be rotated before a solution can be obtained efficiently. It would be interesting to explore the possibility of computing the basis transformation matrices for these rotations at runtime, thereby avoiding approximations and reducing the otherwise significant storage requirements [95].

Beyond computer graphics, applications for example in medical imaging, astrophysics, and geoscience might benefit from the use of the SOHO wavelet basis. In medical imaging in particular the orthonormality of the basis will be of interest; for example the ability to rigorously establish error bounds. For the very large data sets in astrophysics and geoscience the superior approximation performance of the SOHO wavelet basis will be beneficial.

We believe that the concept of performing basis transformations to implement operators will prove to be useful for many different problems in a variety of fields. An obvious application is a data manipulation system which entirely operates in the basis domain (cf. [77, 57, 95]). As already discussed in Chapter 5.4, with the steadily increasing size of data sets such systems will become indispensable. The applicability of basis transformations is at the moment limited by the high costs of performing transforms. We believe that revealing the connections between the fast wavelet transform and basis transformation matrices is the key to overcome these limitations. It will thereby be interesting to explore what are sufficient conditions for the existence of fast transform algorithms and how these depend on different operators and bases. This research might also lead to the development of new wavelet bases specifically designed for particular operations.

We showed in Chapter 6.2.4 that it is very difficult to find the optimal set of coupling coefficients which minimizes the error of a basis transformation in an ℓ_p norm. In practice, we obtained good results by using the k largest coupling coefficients. This is however the obvious strategy and it will be worth to explore alternative approaches.

The development of alternative wavelet representations for spherical signals is another interesting direction for future work. Smoother wavelets for example would be interesting for the representation of signals such as BRDFs. Orthogonality and symmetry are also desirable for these bases but it has to be explored whether or not both properties can

be preserved for smoother bases. The use of alternative constructions for the partition is another research direction which might lead to interesting, new spherical wavelet bases. The HEALPix scheme [33] and the Snyder projection [84] for example provide equal area domains on each level of a partition tree. The derivation of orthonormal wavelet bases is with these partitions thus straightforward. It is however at the moment unclear if it is possible to obtain symmetric bases with these schemes. It also has to be investigated to which extend the significant shape distortion of these subdivision schemes affects the performance of the bases for the approximation and rotation of signals in the basis representation.

The SOHO wavelet basis is defined on the sphere $\mathbb{S}^2$. It would be interesting to develop bases with similar properties on other domains such as general subdivision surfaces or spherical shells. Such bases would be useful for example for finite element methods, climate modeling and PRT for dynamic scenes.

Overcomplete sequences such as frames have shown to be useful in a variety of applications in Euclidean spaces. We believe that such representations will also be valuable for the processing of spherical signals. The possibility that rotationally invariant frames exist is an interesting example.

Chapter 8

Conclusion

In this thesis we developed the SOHO wavelet basis. To our knowledge this is the first spherical Haar wavelet basis that is both fully orthogonal and symmetric. Our result refutes earlier claims which doubted the existence of such a basis [7]. We also derived basis transformation matrices for the rotation of signals represented in spherical Haar wavelet bases such as the SOHO wavelets. The coupling coefficients forming the rotation matrices can be computed analytically, in contrast to the numerical calculation of the coefficients that was necessary in previous work.

Experimental results affirm that the superior theoretical properties of the SOHO wavelet basis also yield practical advantages. For the approximation of spherical signals, the SOHO wavelet basis provides competitive or lower error rates than other spherical Haar wavelet bases in both the ℓ_1 and the ℓ_2 norm. The visual quality of reconstructed signals confirms these results, emphasizing the importance of both orthogonality and symmetry.

Compared to the Haar cubemap basis, rotation in the SOHO wavelet basis yields in general lower error rates in both the ℓ_1 and the ℓ_2 norm. The Haar cubemap basis additionally suffers from a magnification of parametrization artifacts. Compared to other spherical Haar wavelet bases, the rotation of signals in the SOHO wavelet basis provides

visually superior results although numerical error measures do not verify the superiority in all cases. Approximating the rotation matrices by using only the k largest coupling coefficients is for all examined wavelet representations efficient.

Combining the findings in this thesis, we believe that the SOHO wavelet basis provides a more efficient representation for all-frequency signals defined on the sphere than previously proposed representations. We believe that this will enable more efficient solutions for many problems in computer graphics and beyond.

Bibliography

[1] HD View. http://research.microsoft.com/ivm/hdview.htm.

[2] Milton Abramowitz and Irene A. Stegun. *Handbook of Mathematical Functions with Formulas, Graphs, and Mathematical Tables*. Dover, New York, ninth dover printing, tenth gpo printing edition, 1964.

[3] Peter Alfeld, Marian Neamtu, and Larry L. Schumaker. Bernstein-Bézier Polynomials on Spheres and Sphere-like Surfaces. *Computer Aided Geometric Design*, 13(4):333–349, 1996.

[4] Peter Alfeld, Marian Neamtu, and Larry L. Schumaker. Fitting Scattered Data on Sphere-like Surfaces using Spherical Splines. *J. Comput. Appl. Math.*, 73(1-2):5–43, 1996.

[5] J. Antoine, R. Murenzi, P. Vandergheynst, and S. Ali. *Two-Dimensional Wavelets and their Relatives*. Cambridge University Press, September 2004.

[6] Victoria Baramidze. *Spherical Splines for Scattered Data Fitting*. PhD thesis, 2005.

[7] Georges-Pierre Bonneau. Optimal Triangular Haar Bases for Spherical Data. In *VIS '99: Proceedings of the Conference on Visualization '99*, pages 279–284, Los Alamitos, CA, USA, 1999. IEEE Computer Society Press.

[8] Donald L. Burkholder. Boundary Value Problems and Sharp Inequalities for Martingale Transforms. *Ann. Probab.*, 12:647–702, 1984.

[9] Donald L. Burkholder. An Elementary Proof of an Inequality of r. e. a. c. paley. *Bull. London Math. Soc.*, 17:474–478, 1985.

[10] Donald L. Burkholder. *Explorations in Martingale Theory and its Applications*, volume 1464 of *Lecture Notes in Mathematics*, pages 1–66. Springer-Verlag, Berlin, 1991.

[11] Samuel R. Buss and Jay P. Fillmore. Spherical Averages and Applications to Spherical Splines and Interpolation. *ACM Trans. Graph.*, 20(2):95–126, 2001.

[12] Brian Cabral, Nelson Max, and Rebecca Springmeyer. Bidirectional Reflection Functions from Surface Bump Maps. In *SIGGRAPH '87: Proceedings of the 14th Annual Conference on Computer Graphics and Interactive Techniques*, pages 273–281, New York, NY, USA, 1987. ACM Press.

[13] C. H. Choi, J. Ivanic, M. S. Gordon, and K. Ruedenberg. Rapid and Stable Determination of Rotation Matrices between Spherical Harmonics by Direct Recursion. *The Journal of Chemical Physics*, 111:8825–8831, 1999.

[14] Ole Christensen. *An Introduction to Frames and Riesz Bases*. Springer, 2006.

[15] Charles K. Chui. *An Introduction to Wavelets*. Academic Press Professional, Inc., San Diego, CA, USA, 1992.

[16] Peter J. Clarke, David A. Lavalee, G. Blewitt, and T. van Dam. Choice of Basis Functions for the Representation of Seasonal Surface Loading Signals in Geodetic Time Series. *AGU Fall Meeting Abstracts*, pages A121+, December 2004.

[17] A. Croisier, D. Esteban, and C. Galand. Perfect Channel Splitting by Use of Interpolation / Decimation Tree Decomposition Techniques. Presented at the Int. Conf. Inform. Sci. Syst., Patras, Greece, 1976.

[18] Stephan Dahlke, Wolfgang Dahmen, Ilona Weinreich, and Eberhard Schmitt. Multiresolution Analysis and Wavelets on S^2 and S^3. *Numer. Funct. Anal. Optim.*,

16(1-2):19–41, 1995.

[19] Ingrid Daubechies and Wim Sweldens. Factoring Wavelet Transforms into Lifting Steps. *J. Fourier Anal. Appl.*, 4(3):245–267, 1998.

[20] Geoff Davis and Aria Nosratinia. Wavelet-Based Image Coding: An Overview. 1(1), 1998.

[21] Ronald A. DeVore, Bjoern Jawerth, and Bradley J. Lucier. Image Compression through Wavelet Transform Coding. *IEEE Transactions on Information Theory*, 38(2):719–746, 1992.

[22] D. L. Donoho. Unconditional Bases are Optimal Bases for Data Compression and Statistical Estimation. *Appl. Comp. Harm. Anal.*, 1:100–115, 1993.

[23] A. R. Edmonds. *Angular Momentum in Quantum Mechanics*. Princeton University Press, Princeton, NJ, 1957.

[24] Adam Finkelstein and David H. Salesin. Multiresolution Curves. In *SIGGRAPH '94: Proceedings of the 21st annual Conference on Computer Graphics and Interactive Techniques*, pages 261–268, New York, NY, USA, 1994. ACM Press.

[25] N. I. Fisher, T. Lewis, and B. J. J. Embleton. *Statistical Analysis of Spherical Data*. Cambridge University Press, 1993.

[26] W. Freeden. *Multiscale Modelling of Spaceborne Geodata*. B.G. Teubner, Stuttgart, Leipzig, 1999.

[27] W. Freeden, T. Gervens, and M. Schreiner. *Constructive Approximation on the Sphere (With Applications to Geomathematics)*. Oxford Sciences Publication. Clarendon Press, Oxford University, 1998.

[28] Willy Freeden and U. Windheuser. Combined Spherical Harmonic and Wavelet Expansion — A Future Concept in Earth's Gravitational Determination. *Appl. Comput. Harmon. Anal.*, 4:1–37, 1997.

[29] Dennis Gabor. Theory of Communication. 93:429–457, November 1946.

[30] Pascal Gautron, Jaroslav Křivánek, Sumanta N. Pattanaik, and Kadi Bouatouch. A Novel Hemispherical Basis for Accurate and Efficient Rendering. In *Rendering Techniques 2004, Eurographics Symposium on Rendering*, pages 321–330, June 2004.

[31] Maria Girardi and Wim Sweldens. A New Class of Unbalanced Haar Wavelets that form an Unconditional Basis for L_p on General Measure Spaces. *J. Fourier Anal. Appl.*, 3(4), 1997.

[32] Anamaria Gomide and Jorge Stolfi. Bases for Non-Homogeneous Polynomial $\mathbf{C}_k$ Splines on the Sphere. In *Proc. LATIN'98 - Latin American Theoretical Informatics Conference*, volume 1380 of *Lecture Notes in Computer Science*, pages 133–140. Springer, April 1998.

[33] K. M. Gorski, E. Hivon, A. J. Banday, B. D. Wandelt, F. K. Hansen, M. Reinecke, and M. Bartelman. HEALPix – a Framework for High Resolution Discretization, and Fast Analysis of Data Distributed on the Sphere. *The Astrophysical Journal*, 622:759, 2005.

[34] Paul Green, Jan Kautz, Wojciech Matusik, and Frédo Durand. View-Dependent Precomputed Light Transport using Nonlinear Gaussian Function Approximations. In *SI3D '06: Proceedings of the 2006 Symposium on Interactive 3D Graphics and Games*, pages 7–14, New York, NY, USA, 2006. ACM Press.

[35] Robin Green. Spherical Harmonic Lighting: The Gritty Details. Presentation at Game Developer Conference (GDC) 2003.

[36] Markus H. Gross. L2 Optimal Oracles and Compression Strategies for Semiorthogonal Wavelets. December 1996.

[37] Albert Haar. Zur Theorie der Orthogonalen Funktionensysteme. *Mathematische Annalen*, 69:331–371, 1910.

[38] Ying He, Xin Li, Xianfeng Gu, and Hong Qin. Brain Image Analysis using Spherical Splines. In *EMMCVPR*, pages 633–644, 2005.

[39] I. T. Jolliffe. *Principal Component Analysis*. Springer, 1986.

[40] James T. Kajiya. The Rendering Equation. In *SIGGRAPH '86: Proceedings of the 13th Annual Conference on Computer Graphics and Interactive Techniques*, pages 143–150, New York, NY, USA, 1986. ACM Press.

[41] Taguchi Katsuyuki, L. Zeng Gengsheng, and Grant T. Gullberg. Cone-Beam Image Reconstruction using Spherical Harmonics. *Physics in Medicine and Biology*, 46:N127–N138(1), 2001.

[42] Jan Kautz, Peter-Pike Sloan, and John Snyder. Fast, Arbitrary BRDF Shading for Low-Frequency Lighting using Spherical Harmonics. In *EGRW '02: Proceedings of the 13th Eurographics Workshop on Rendering*, pages 291–296, Aire-la-Ville, Switzerland, Switzerland, 2002. Eurographics Association.

[43] Jan J. Koenderink, Andrea J. van Doorn, and Marigo Stavridi. Bidirectional Reflection Distribution Function Expressed in Terms of Surface Scattering Modes. In *ECCV '96: Proceedings of the 4th European Conference on Computer Vision-Volume II*, pages 28–39, London, UK, 1996. Springer-Verlag.

[44] Jaroslav Křivánek, Jaakko Konttinen, Kadi Bouatouch, Sumanta Pattanaik, and Jiří Žára. Fast Approximation to Spherical Harmonic Rotation. In *SCCG '06: Proceedings of the 22nd Spring Conference on Computer Graphics*, New York, NY, USA, 2005. ACM Press.

[45] Paul Lalonde and Alain Fournier. A Wavelet Representation of Reflectance Functions. *IEEE Transactions on Visualization and Computer Graphics*, 3(4):329–336,

1997.

[46] Michael Lounsbery, Tony D. DeRose, and Joe Warren. Multiresolution Analysis for Surfaces of Arbitrary Topological Type. *ACM Trans. Graph.*, 16(1):34–73, 1997.

[47] Wan-Chun Ma, Chun-Tse Hsiao, Ken-Yi Lee, Yung-Yu Chuang, and Bing-Yu Chen. Real-Time Triple Product Relighting Using Spherical Local-Frame Parameterization. *The Visual Computer*, (9-11):682–692, 2006. Pacific Graphics 2006 Conference Proceedings.

[48] Thomas M. MacRobert. *Spherical Harmonics; An Elementary Treatise on Harmonic Functions, with Applications*. Dover Publications, 1948.

[49] Oleg A. Makhotkin. Analysis of Radiative Transfer between Surfaces by Hemispherical Harmonics. *Journal of Quantitative Spectroscopy and Radiative Transfer*, 56:869–879, December 1996.

[50] Michael W. Marcellin, Michael J. Gormish, Ali Bilgin, and Martin P. Boliek. An overview of jpeg-2000. In *IEEE Data Compression Conference*, pages 523–541, 2000.

[51] The Mathworks. Matlab: The Language of Technical Computing.

[52] Adam H. Monahan. *Nonlinear Principal Component Analysis of Climate Data*. PhD thesis, THE UNIVERSITY OF BRITISH COLUMBIA (CANADA), 2000.

[53] Delphine Nain, Steven Haker, Aaron F. Bobick, and Allen Tannenbaum. Multiscale 3D Shape Analysis using Spherical Wavelets. In *MICCAI (2)*, pages 459–467, 2005.

[54] Delphine Nain, Steven Haker, Aaron F. Bobick, and Allen Tannenbaum. Shape-Driven 3D Segmentation Using Spherical Wavelets. In *MICCAI (1)*, pages 66–74, 2006.

[55] Francis J. Narcowich and Joseph D. Ward. Nonstationary Wavelets on the m-Sphere for Scattered Data. *App. Comput. Harm. Anal.*, 3:324–336, 1996.

[56] Ren Ng, Ravi Ramamoorthi, and Pat Hanrahan. All-Frequency Shadows using Non-Linear Wavelet Lighting Approximation. *ACM Trans. Graph.*, 22(3):376–381, 2003.

[57] Ren Ng, Ravi Ramamoorthi, and Pat Hanrahan. Triple Product Wavelet Integrals for All-Frequency Relighting. *ACM Trans. Graph.*, 23(3):477–487, 2004.

[58] Gregory M. Nielson, Il-Hong Jung, and Junwon Sung. Haar Wavelets over Triangular Domains with Applications to Multiresolution Models for Flow over a Sphere. In *VIS '97: Proceedings of the 8th Conference on Visualization '97*, pages 143–ff., Los Alamitos, CA, USA, 1997. IEEE Computer Society Press.

[59] NVIDIA. Cuda: Compute unified device architecture.

[60] Takahiro Okabe, Imari Sato, and Yoichi Sato. Spherical Harmonics vs. Haar Wavelets: Basis for Recovering Illumination from Cast Shadows. *cvpr*, 01:50–57, 2004.

[61] Alan V. Oppenheim, Ronald W. Schafer, and John R. Buck. *Discrete-Time Signal Processing (2nd ed.)*. Prentice-Hall, Inc., Upper Saddle River, NJ, USA, 1999.

[62] John D. Owens, David Luebke, Naga Govindaraju, Mark Harris, Jens Krüger, Aaron E. Lefohn, and Timothy J. Purcell. A Survey of General-Purpose Computation on Graphics Hardware. *Computer Graphics Forum*, 26(1):80–113, 2007.

[63] Matthew Papakipos. Converging Design Features in CPUs and GPUs. http://www.hpcwire.com/hpc/1209133.html, 2007.

[64] Luis Pastor and Angel Rodriguez. Surface Approximation of 3d Objects from Irregularly Sampled Clouds of 3D Points Using Spherical Wavelets. In *ICIAP '99: Proceedings of the 10th International Conference on Image Analysis and Processing*, page 70, Washington, DC, USA, 1999. IEEE Computer Society.

[65] Didier Pinchon and Philip E Hoggan. Rotation Matrices for Real Spherical Harmonics: General Rotations of Atomic Orbitals in Space-Fixed Axes. *Journal of Physics A: Mathematical and Theoretical*, 40(7):1597–1610, 2007.

[66] William K. Pratt. *Digital Image Processing (2nd ed.)*. John Wiley & Sons, Inc., New York, NY, USA, 1991.

[67] Emil Praun and Hugues Hoppe. Spherical Parametrization and Remeshing. *ACM Trans. Graph.*, 22(3):340–349, 2003.

[68] William H. Press, Saul A. Teukolsky, William T. Vetterling, and Brian P. Flannery. *Numerical Recipes in C: The Art of Scientific Computing*. Cambridge University Press, New York, NY, USA, 1992.

[69] Ravi Ramamoorthi and Pat Hanrahan. Frequency Space Environment Map Rendering. In *SIGGRAPH '02: ACM SIGGRAPH 2002 Papers*, pages 517–526, New York, NY, USA, 2002. ACM Press.

[70] Daniela Roşca. Weighted Haar Wavelets on the Sphere.

[71] Daniela Roşca. Optimal Haar Wavelets on Spherical Triangulations. *Pure Mathematics and Applications*, 15(2), 2004.

[72] Daniela Roşca. Haar Wavelets on Spherical Triangulations. In Neil A. Dodgson, Michael S. Floater, and Malcolm A. Sabin, editors, *Advances in Multiresolution for Geometric Modelling*, Mathematics and Visualization, pages 405–417. Springer Berlin Heidelberg, 2005.

[73] Sam T. Roweis and Lawrence K. Saul. Nonlinear Dimensionality Reduction by Locally Linear Embedding. *Science*, 290(5500):2323–2326, December.

[74] Kevin Sahr, Denis White, and A. Jon Kimerling. Geodesic Discrete Global Grid Systems. *Cartography and Geographic Information Science*, 30(2):121–134, 2003.

[75] Peter Schröder. Wavelets for Computer Graphics. *Proceedings of the IEEE*, 84(4):615–625, 1996.

[76] Peter Schröder and Wim Sweldens. Spherical Wavelets: Efficiently Representing Functions on the Sphere. In *SIGGRAPH '95: Proceedings of the 22nd annual Conference on Computer Graphics and Interactive Techniques*, pages 161–172, New York, NY, USA, 1995. ACM Press.

[77] Peter Schröder and Wim Sweldens. Spherical Wavelets: Texture Processing. In P. Hanrahan and W. Purgathofer, editors, *Rendering Techniques '95*, pages 252–263. Springer Verlag, Wien, New York, August 1995.

[78] Claude E. Shannon. A Mathematical Theory of Communication. *The Bell System Technical Journal*, 27:379–423, 623–, july, october 1948.

[79] Jerome. M. Shapiro. Embedded Image Coding sing Zerotrees of Wavelet Coefficients. *IEEE Trans. Signal Processing*, 41(12):3445–3462, 1993.

[80] François Sillion, James Arvo, Stephen Westin, and Donald P. Greenberg. A Global Illumination Solution for General Reflectance Distributions. In *SIGGRAPH '91: Proceedings of the 18th Annual Conference on Computer Graphics and Interactive Techniques*, pages 187–196, New York, NY, USA, 1991. ACM Press.

[81] Peter-Pike Sloan, Jesse Hall, John Hart, and John Snyder. Clustered Principal Components for Precomputed Radiance Transfer. In *SIGGRAPH '03: ACM SIGGRAPH 2003 Papers*, pages 382–391, New York, NY, USA, 2003. ACM Press.

[82] Peter-Pike Sloan, Jan Kautz, and John Snyder. Precomputed Radiance Transfer for Real-Time Rendering in Dynamic, Low-Frequency Lighting Environments. In *SIGGRAPH '02: ACM SIGGRAPH 2002 Papers*, pages 527–536, New York, NY, USA, 2002. ACM Press.

[83] Peter-Pike Sloan, Ben Luna, and John Snyder. Local, Deformable Precomputed Radiance Transfer. In *SIGGRAPH '05: ACM SIGGRAPH 2005 Papers*, pages 1216–1224, New York, NY, USA, 2005. ACM Press.

[84] John P. Snyder. An Equal-Area Map Projection for Polyhedral Globes. *Cartographica*, 29(1):10–21.

[85] John P. Snyder. *Map Projections; a Working Manual*. United States Government Printing, 1987.

[86] Eric J. Stollnitz, Tony D. DeRose, and David H. Salesin. Wavelets for Computer Graphics: A Primer, Part 1. *IEEE Comput. Graph. Appl.*, 15(3):76–84, 1995.

[87] Eric J. Stollnitz, Tony D. Derose, and David H. Salesin. *Wavelets for Computer Graphics: Theory and Applications*. Morgan Kaufmann Publishers Inc., San Francisco, CA, USA, 1996.

[88] Weifeng Sun and Amar Mukherjee. Generalized Wavelet Product Integral for Rendering Dynamic Glossy Objects. *ACM Trans. Graph.*, 25(3):955–966, 2006.

[89] Wim Sweldens. The Lifting Scheme: A New Philosophy in Biorthogonal Wavelet Constructions. In A. F. Laine and M. Unser, editors, *Wavelet Applications in Signal and Image Processing III*, pages 68–79. Proc. SPIE 2569, 1995.

[90] Wim Sweldens. The Lifting Scheme: A Custom-Design Construction of Biorthogonal Wavelets. *Appl. Comput. Harmon. Anal.*, 3(2):186–200, 1996.

[91] Wim Sweldens. Wavelets: What Next? *Proc. IEEE*, 84(4):680–685, 1996.

[92] Isaac Todhunter. *Spherical Trigonometry, for the Use of Colleges and Schools*. Macmillan, London, 1901.

[93] Yu-Ting Tsai and Zen-Chung Shih. All-Frequency Precomputed Radiance Transfer using Spherical Radial Basis Functions and Clustered Tensor Approximation. In

SIGGRAPH '06: ACM SIGGRAPH 2006 Papers, pages 967–976, New York, NY, USA, 2006. ACM Press.

[94] Liang Wan, Tien-Tsin Wong, and Chi-Sing Leung. Spherical q2-tree for sampling dynamic environment sequences. In *Rendering Techniques*, pages 21–30, 2005.

[95] Rui Wang, Ren Ng, David Luebke, and Greg Humphreys. Efficient Wavelet Rotation for Environment Map Rendering. In *Proceedings of the 2006 Eurographics Symposium on Rendering*. Springer-Verlag, Vienna, 2006. Published as Rendering Techniques 2006.

[96] Ze Wang, Chi-Sing Leung, Yi-Sheng Zhu, and Tien-Tsin Wong. Data Compression with Spherical Wavelets and Wavelets for the Image-Based Relighting. *Comput. Vis. Image Underst.*, 96(3):327–344, 2004.

[97] Stephen H. Westin, James R. Arvo, and Kenneth E. Torrance. Predicting Reflectance Functions from Complex Surfaces. In *SIGGRAPH '95: ACM SIGGRAPH 1992 Papers*, pages 255–264, New York, NY, USA, 1992. ACM Press.

[98] Denis White, A. Jon Kimerling, Kevin Sahr, and Lian Song. Comparing Area and Shape Distortion on Polyhedral-Based Recursive Partitions of the Sphere. *International Journal of Geographical Information Science*, 12(8):805–827, 1998.

[99] Yves Wiaux, L. Jacques, and Pierre Vandergheynst. Correspondence Principle between Spherical and Euclidean Wavelets. *The Astrophysical Journal*, 632:15, 2005.

[100] Boon Thye Thomas Yeo, Wanmei Ou, and Polina Golland. Invertible Filter Banks on the 2-Sphere.

[101] Kun Zhou, Yaohua Hu, Stephen Lin, Baining Guo, and Heung-Yeung Shum. Precomputed Shadow Fields for Dynamic Scenes. In *SIGGRAPH '05: ACM SIGGRAPH 2005 Papers*, pages 1196–1201, New York, NY, USA, 2005. ACM Press.

Appendix A

Properties of the Pseudo-Haar Basis

In the following it will be shown that the pseudo Haar basis proposed by Ma et al. [47] is not a basis of the space $L_2 \equiv L_2(\mathbb{S}^2, d\omega)$ of functions with finite energy on the sphere.

In Section 3.1.3 the definition of a basis has been given. To show that the pseudo Haar basis is not a basis of L_2 it is sufficient to provide a counter example where the sequence in Eq. 3.2 does not converge.

Proof. Let $\mathcal{B}$ be a partition obtained with the geodesic bisector subdivision from an octahedron. A constant signal f with magnitude c defined over the first octant of $\mathcal{B}$ is given by

$$f = c\ \tau_{0,0}, \tag{A.1}$$

with $\tau_{0,0} \in \mathcal{B}$. Let $\left\{\hat{\psi}_i\right\}_{i\in\mathcal{I}}$ be the pseudo Haar wavelets with the same assumptions as in the work by Ma et al. [47]. For this sequence Eq. 3.2 takes the form

$$f = \sum_{i\in\mathcal{I}} \gamma_i\ \hat{\psi}_i = \sum_{i\in\mathcal{I}} \left\langle f\ ,\ \hat{\psi}_i \right\rangle \hat{\psi}_i. \tag{A.2}$$

Obviously, the inner product in Eq. A.2 is zero if $\mathrm{supp}(f) \cap \mathrm{supp}(\hat{\psi}_i) = \emptyset$. In the following therefore only the basis functions defined over the first partition tree have to be considered

and we will denoted with $\hat{K}(j)$ an index set defined over the partitions of the first octant on level j.

Considering the projection of f into the pseudo Haar basis yields the scaling basis function coefficient

$$\lambda_{0,0} = \langle f \ , \ \varphi_{0,0} \rangle \, .$$

With the refinement relationship in Eq. 3.7 one obtains

$$= \int_{\mathbb{S}^2} c \ \tau_{0,0} \sum_l h_{0,0,l} \ \varphi_{1,l} \ d\omega.$$

For the pseudo Haar basis the scaling functions are one over their support so that

$$\begin{aligned} &= c \ \sum_l h_{0,0,l} \int_{\mathbb{S}^2} \tau_{0,0} \ \tau_{1,l} \ d\omega \\ &= c \ \sum_l h_{0,0,l} \ \alpha_{1,l}. \end{aligned}$$

An analogous calculation shows that the wavelet basis function coefficients are

$$\gamma_{j,k} = c \ \sum_l g_{j,k,l} \ \alpha_{j+1,l},$$

with $j \in \mathcal{J}$ and $k \in \hat{\mathcal{K}}(j)$.

Note that all basis function coefficients are nonzero. This follows from the non-vanishing integral of the wavelet basis functions. Combining the basis function coefficients with Equation A.2, and employing the refinement relationship for the wavelet basis functions yields

$$\hat{f} = \sum_{l_1} \left(c \ \sum_{l_2} h_{0,0,l_2} \ \alpha_{1,l_2} \right) h_{0,0,l_1} \ \varphi_{1,l_1} + \sum_{j \in \mathcal{J}} \sum_{k \in \hat{\mathcal{K}}(j)} \sum_{l_1} \left(c \ \sum_{l_2} g_{j,k,l_2} \ \alpha_{j+1,l_2} \right) g_{j,k,l_1} \ \varphi_{j+1,l_1}.$$

It is easy to see that the filter coefficients $h_{j,k,l}$ and $g_{j,k,l}$ for the pseudo Haar basis satisfy Eq. 3.12. It follows that

$$\begin{aligned}\hat{f} &= c \sum_l \alpha_{1,l}\ \varphi_{1,l} + \sum_{j\in\mathcal{J}} \sum_{k\in\hat{\mathcal{K}}(j)} c \sum_l \alpha_{j+1,l}\ \varphi_{j+1,l} \\ &= c \left(\sum_l \alpha_{1,l}\ \tau_{1,l} + \sum_{j\in\mathcal{J}} \sum_{k\in\hat{\mathcal{K}}(j)} \sum_l \alpha_{j+1,l}\ \tau_{j+1,l} \right) \end{aligned} \tag{A.3}$$

The union of the $\tau_{j,k}$ for fixed j and $k \in \hat{\mathcal{K}}(j)$ form $\tau_{0,0}$. The geodesic bisector subdivision does however not yield child domains with equal areas and the scaling factors $\alpha_{j,k}$ on the right hand side of Eq. A.3 are therefore not constant. Thus $\hat{f}$ is not constant over its support which implies that $f \neq \hat{f}$, that is Eq. 3.2 is not satisfied.

With the same derivation it is easy to show that the SOHO wavelet basis satisfies Eq. 3.2 for the constant signal f. □